NOTE TO USERS

The original manuscript received by UMI contains indistinct, slanted and or light print. All efforts were made to acquire the highest quality manuscript from the author or school. Microfilmed as received.

This reproduction is the best copy available

UMI

University of Alberta

Simulation of the Scintillating Tile Endcap Detector of OPAL

By

Bryan Lawrence Caron ©

A dissertation

presented to the Faculty of Graduate Studies and Research

in partial fulfilment of the requirements for the degree

of

Master of Science

Department of Physics

Edmonton, Alberta

Spring 1998

National Library of Canada

Acquisitions and Bibliographic Services

395 Wellington Street
Ottawa ON K1A 0N4
Canada

Bibliothèque nationale du Canada

Acquisitions et services bibliographiques

395, rue Wellington
Ottawa ON K1A 0N4
Canada

Your file Votre référence

Our file Notre référence

The author has granted a non-exclusive licence allowing the National Library of Canada to reproduce, loan, distribute or sell copies of this thesis in microform, paper or electronic formats.

L'auteur a accordé une licence non exclusive permettant à la Bibliothèque nationale du Canada de reproduire, prêter, distribuer ou vendre des copies de cette thèse sous la forme de microfiche/film, de reproduction sur papier ou sur format électronique.

The author retains ownership of the copyright in this thesis. Neither the thesis nor substantial extracts from it may be printed or otherwise reproduced without the author's permission.

L'auteur conserve la propriété du droit d'auteur qui protège cette thèse. Ni la thèse ni des extraits substantiels de celle-ci ne doivent être imprimés ou autrement reproduits sans son autorisation.

0-612-28921-4

Canada

UNIVERSITY OF ALBERTA

FACULTY OF GRADUATE STUDIES AND RESEARCH

The undersigned certify that they have read, and recommend to the Faculty of Graduate Studies and Research for acceptance, a thesis entitled "Simulation of the Scintillating Tile Endcap Detector of OPAL " submitted by Bryan Lawrence Caron in partial fulfilment of the requirements for the degree of Master of Science.

Professor J.L. Pinfold , Supervisor

Professor F.C. Khanna

Professor P. Kitching

Associate Professor L.W. Sigurdson

Date: April 15, 1998.

Abstract

A simulation of scintillating tiles with complex arrangements of wavelength shifting (WLS) fibre readout is presented. Simulations were performed of both the prototype and final design elements of the scintillating tile endcap (TE) detector of the OPAL detector at the Large Electron Positron (LEP) collider. The TE detector was installed with the purpose of improving trigger redundancy and performance by providing good time resolution and efficient detection of minimum ionizing particles (MIPs). The construction of detectors for this purpose is a new application of scintillator-WLS fibre technology.

Good agreement is observed between data and Monte Carlo for the passage of MIPs in terms of the average photoelectron output and the uniformity of response across the prototype tile. A similar comparison is made for the TE Tile 2 sector using $\mu^+ \mu^-$ events. The small event sample size limits the comparison of Monte Carlo and data for the TE Tile 2.

Acknowledgements

I would like to thank my supervisor, Dr. James Pinfold for his interest in and enthusiasm for the research presented in this thesis. A great deal of thanks is also extended to the staff of the Centre for Subatomic Research who facilitated this work.

I would especially like to thank Dr. Nathan Rodning for his many helpful discussions which greatly assisted in carrying out the work necessary for this thesis.

Thanks also go to Stan Bentvelsen of CERN for his assitance in the analysis of the TE data.

I would like to acknowledge the office gang with whom I have shared the confines of P-146 for the past several years: Norm Buchanan, Robert Davis, Anthony Faust, Philip Kayal, Dan MacQueen, Trevor Nickle, and Dugan O'Neil.

I would like to thank my parents for their continuing support over the many years I have spent avoiding the real world.

Finally and foremost, I would like to thank my wife Anastasia for her unfaltering support and belief in my ability to once and for all write up this thesis.

Contents

Abstract iii

Acknowledgements iv

Contents v

List of Figures x

List of Tables xvii

1 Introduction 1

2 Experimental Apparatus 4

2.1 The Large Electron-Positron (LEP) Collider 4

2.2 The OPAL Detector 8

2.2.1 The Central Detector 9

2.2.2 Time-Of-Flight Counters 20

2.2.3 Electromagnetic Calorimeter 22

2.2.4 The Hadron Calorimeter 25

2.2.5 Muon Detector 26

2.2.6 The Forward Detectors and Si-W Calorimeter 28

2.3 The Trigger and Online Data Flow 31

2.3.1 The OPAL Trigger 31

2.3.2 Online Data Flow 33

2.3.3 The OPAL Detector Simulation Software 35

3 The Tile Endcap (TE) Detector **37**

3.1 Motivation 37

3.1.1 Pre-TE Trigger Conditions 38

3.1.2 Bunch Trains 39

3.2 The TE Mechanical and Optical Design 42

3.2.1 Design Constraints and Considerations 43

3.2.2 Tile and Electronics Readout 43

3.3 Scintillator and Fibre Properties 50

3.3.1 Plastic Scintillator BC408 50

3.3.2 Kuraray Y11 Wavelength Shifting Fibre 51

3.3.3 Bicron BCF-91A Wavelength Shifting Fibre 53

4 Scintillator and Optical Fibre Physics **56**

4.1 The Scintillation Process 57

4.1.1 Organic Scintillators 58

4.2 Optical Fibres 64

4.2.1 Leaky Ray Theory of Optical Waveguides 64

4.2.2 Geometrical Optics 73

5 Simulation Tools **82**

5.1 Simulation Packages 82

5.1.1 GEANT Version 3.21 82

5.1.2 GUIDEIT 84

5.2 The GEANT Description of Scintillation Detectors 85

5.3 GEANT-GUIDEIT Combination 89

5.3.1 GEANT Failure During Ray Tracing 89

5.3.2 GEANT-GUIDEIT Geometry Description Limitations 93

5.4 Parallel GEANT 95

6 Single Optical Fibre Measurements With a CCD **98**

6.1 The Single Fibre Light Yield Experiment 98

6.2 GUIDEIT Single Fibre Simulation 100

6.3 Experimental Data and Simulation Results 103

6.3.1 Image Processing 103

6.3.2 Experiment and Monte Carlo Results 103

6.3.3 Photon Distribution in the Fibre Cross-Section 108

6.3.4 Square Optical Fibre Simulation Results 111

7 Three Sigma Fibre Layout Scintillating Tiles **116**

7.1 Minimum Ionizing Particles 116

7.2 Cosmic Rays 117

7.3 Experimental Setup: The Cosmic Ray Telescope 117

7.3.1 The Three Sigma Prototype Tile 120

7.4 Three Sigma Prototype Tile Simulation 122

7.5 Cosmic Ray Scan and Monte Carlo Results 128

7.5.1 Light Yield Uniformity Studies 129

7.5.2 Photoelectron Output 156

8 TE Scintillating Tile Performance **168**

8.1 TE Scintillating Tiles 169

8.1.1 The TE Tile 2 Segment 169

8.1.2 TE Tile 2 Description with GEANT-GUIDEIT 170

8.2 TE Tile 2 Monte Carlo and Measured Results 174

8.2.1 MIP Sensitivity of TE 175

8.2.2 TE Tile 2 Average Light Yield 178

8.2.3 Tile 2 Monte Carlo Light Yield 184

8.2.4 TE Tile 2 Predicted Light Yield Uniformity 186

8.2.5 Tile 2 Timing Characteristics 187

9 Conclusions 190

Bibliography 193

A Simulation of Photon Propagation Through Bent Optical Fibres 197

A.1 Photon Tracking Through Toroidal Geometries 197

A.2 Losses of Photons in Bent Fibres 200

B Optical Fibre Connector Simulation Results 202

B.1 Optical Fibre Connector Simulations 202

B.1.1 Radial Distribution of Photons 204

List of Figures

2.1 The injector complex and LEP ring 6

2.2 LEP Integrated Luminosity 7

2.3 The OPAL Detector 10

2.4 Cutaway view of the OPAL Silicon Microvertex Detector 12

2.5 Cross-sectional view of the OPAL Silicon Microvertex Detector 13

2.6 Schematic view of the OPAL vertex detector 14

2.7 Wire layout of the OPAL vertex detector. 15

2.8 Cross Sectional view of a single OPAL Z Chamber. 19

2.9 Cross sectional view of the OPAL forward detector region. 29

2.10 Trigger Generation by θ-ϕ 32

3.1 TE Segment 45

3.2 Coupler to connect the WLS and clear optical fibres. 47

3.3 Coupling device to connect the clear optical fib-ER to the photomultiplier tubes. 48

3.4 Interface of TE to the OPAL Pretrigger and Trigger 49

3.5 Emission Spectra of BC-408 Scintillator 52

3.6 Absorption and Emission Spectra of BCF-91A WLS Fibre 52

3.7 Mean Free Path of Incident Light in BCF-91A WLS Fibre 54

4.1 Scintillator Single and Two-Component Exponential Decays 58

4.2 Energy Level Diagram for Organic Scintillator Materials 60

4.3 Scintillation mechanism for a typical Plastic Scintillator 62

4.4 Optical Fibre of Circular Cross Section 65

4.5 Leaky q'th mode fields and radiation caustic r_{tp}^{q} 68

4.6 Fraction of Incident Power from an Incoherent Source as a function of z/ρ 74

4.7 Meridional and Skew Rays 75

4.8 Spherical Polar Angles for Ray Reflection 77

4.9 Distribution of Rays in $\overline{\beta} - \overline{l}$ 79

4.10 Geometrical Acceptance of Emitted Photons 80

5.1 Variation of Angle of Incidence and Inner Caustic Radius during GEANT tracking. 91

5.2 GEANT Approximation of a Toroidal Segment by a Series of Connected Cylinders with Noncoplanar Faces. 95

6.1 Schematic layout of apparatus used to measure the light yield distribution in the WLS fibre cross-section. 99

6.2 Three dimensional view of the light yield signal of a single WLS fibre readout via a CCD array. 104

6.3 Profile view of the measured and normalized Monte Carlo light yield distributions for N=1.45. 106

6.4 Centre slice of the measured and normalized Monte Carlo light yield distributions for N=1.45. 107

6.5 Distribution of photons in the fibre cross-section arising from uniformly distributed emission positions. 109

6.6 Distribution of WLS photons in the fibre cross-section. 110

6.7 Distribution of photons in the plane perpendicular to the fibre axis for varying distances from the fibre end toward the CCD array. . . . 112

6.8 Distribution of photons in the square fibre cross-section immediately prior to exiting the fibre and after traveling through 1 mm of plastic towards the CCD array. 114

6.9 Profile and Centre Slice distributions of the measured round fibre light yield and Monte Carlo square fibre. 115

7.1 Layout of the cosmic ray telescope used to examine the prototype scintillating tiles. 119

7.2 GEANT drawing of the 3 Sigma prototype scintillating tile geometry and the cosmic ray scan region across the face of the tile surface. . 121

7.3 Measured ADC distribution for cosmic ray muons passing through the central scan region of the three sigma prototype scintillating tile. . 122

7.4 Quantum efficiency of the Philips XP2262 photomultiplier tube Lime-glass photocathode as a function of wavelength. 126

7.5 GEANT drawing of the passage of a muon through a 3 Sigma prototype scintillating tile. 128

7.6 Number of reflections experienced by primary scintillation photons for perfectly reflecting surfaces and infinite attenuation lengths. . . . 137

7.7 Number of reflections experienced by WLS photons for perfectly reflecting surfaces and infinite attenuation lengths. 138

7.8 Distribution of Chi-Square values for all possible reflectivity values. . 144

7.9 Chi-Square variation as a function of reflectivity values for Tile-Air Top-Bottom, Tile-Air Side-Side, Air-Wrapping, and Core-Surface reflectivities. 145

7.10 Chi-Square variation satisfying $\chi^2 < 0.036$ as a function of reflectivity values for Tile-Air Top-Bottom, Tile-Air Side-Side, Air-Wrapping, and Core-Surface reflectivities. 146

7.11 Simulated photoelectron yield at the WLS fibre end for each of the 25 spatial bins. 147

7.12 Comparison of the Monte Carlo and measured light yield of the 3 Sigma Prototype scintillating tile-WLS fibre combination as a function of position across the face of the scintillator for parameter combination 424. 149

7.13 Comparison of the Monte Carlo and measured light yield for three of the reflectivity combinations with $\chi^2 < 0.0343$. 150

7.14 Pathlength of the scintillation and WLS photons assuming perfect and imperfect surface reflectivities and attenuation lengths. 152

7.15 Distance from the readout end of the WLS fibre to the point of scintillation photon absorption for reflectivity parameter combination 424. 154

7.16 Number of reflections experienced by primary scintillation photons for both perfectly reflective and realistic non-perfectly reflecting surfaces. 157

7.17 Number of reflections experienced by WLS photons at the Fibre Core-Cladding, and Fibre Cladding-Scintillator interfaces for both perfectly reflective and realistic non-perfectly reflecting surfaces. . . . 158

7.18 Simulated photoelectron yield at the WLS fibre end. The Monte Carlo result was fitted with a Poisson distribution convoluted with a Gaussian to determine the mean number of photoelectrons. 161

8.1 Sketch of the WLS fibre layout of the Tile 2 element of the TE detector. 171

8.2 GEANT drawing of the TE Tile 2 geometry and the MIP scan region across the face of the tile surface. 172

8.3 Quantum efficiency of the Electron Tubes photomultiplier tube Lime-glass photocathode as a function of wavelength. 173

8.4 Observed TE ADC distribution from the passage of associated charged tracks from $\mu^+ \mu^-$ events in OPAL. 176

8.5 MIP detection efficiency of the TE Tile 2, Tile 3, and combined Tile 2+3 sectors for charged tracks 1.0 cm interior to the tile perimeter. 179

8.6 MIP detection efficiency of the TE Tile 2, Tile 3, and combined Tile 2+3 sectors for charged tracks 3.0 cm interior to the tile perimeter. 180

8.7 Average measured photoelectron output for the passage of MIPs through the TE Tile 2 sector. 182

8.8 Average measured photoelectron output for the passage of MIPs through the central scan region of the TE Tile 2 sector. 183

8.9 Number of predicted photoelectrons seen at the end of the optical fibre for the TE Tile 2 with reflectivity combination 424. 186

8.10 Monte Carlo prediction for the light yield uniformity across the scan region of the TE Tile 2 for reflectivity combination 424. 187

8.11 Raw pulse signal observed from the passage of cosmic rays for a production TE Tile 2 sector. 189

8.12 Monte Carlo light output as a function of time for the passage of a single cosmic ray through TE Tile 2 assuming a single photoelectron resolution of approximately 2 ns. 189

A.1 Exit position of photons which escapes from an optical fibre. 201

B.1 Layout of the wavelength shifting (WLS) fibre to optical fibre connector simulated using GUIDEIT. 203

B.2 Comparison of the GEANT-GUIDEIT 3σ and GUIDEIT stand-alone predictions for the radial distribution of photons in the fibre cross-section which reach the end of the WLS fibre and survive the adjoining connector. 208

B.3 Comparison of the radial distribution of photons in the fibre cross-section which reach the end of the WLS fibre and survive the adjoining connector for both GEANT-GUIDEIT 3σ and GUIDEIT stand-alone simulations. 209

B.4 Radial distribution of photon exit position at the wavelength shifting fibre for photons which propagate through the connector and survive to the end of the optical fibre. 210

List of Tables

3.1 Physical constants of *BC*-408 plastic scintillator. 50

3.2 Physical constants of *BCF*-91*A* wavelength shifting fibre. 53

4.1 Gaussian and exponential parameters for several plastic scintillators describing the light pulse distribution. 63

7.1 Quantum efficiency of the Philips XP2262 photomultiplier tube Lime-glass photocathode as a function of wavelength. 125

7.2 Surface reflectivity values used in the Monte Carlo simulations of the three sigma fibre prototype tile. 130

7.3 Fraction of primary scintillation and secondary WLS photons which encounter a reflection at the various geometric interfaces. The values reported were determined for the case of perfectly reflecting surfaces and infinite attenuation lengths. 133

7.4 Reflectivity value combinations yielding the minimum χ^2 values satisfying $\chi^2 < 0.036$. Reflectivity values are given for the Tile-Air Top-Bottom (TATBCUT), Tile-Air Side-Side (TASSCUT), Air-Wrapping (AMCUT), and Fibre Core-Reflective Surface (CORSCUT). All combinations have Fibre Core-Cladding (COCCUT) and Fibre Cladding-Optical Glue (CLTCUT) reflectivities of 0.999 and 0.990, respectively. 148

7.5 Mean number of photoelectrons expected at the end of the optical fibre from Monte Carlo and the corresponding value of the fibre surface polish quality T_{Smooth} which is necessary for the Monte Carlo and measured light yield to be in agreement. The simple connector model predicts $T_{Smooth} = 0.79 \pm 0.03$. 167

8.1 Values of the angular and spatial coverage provided by each of the three TE Tile elements in the OPAL environment. 170

8.2 Surface reflectivity values used in the Monte Carlo simulations of the Tile 2 element of TE. 174

B.1 Transmission coefficient results for varying connector size and fibre misalignment from Monte Carlo simulation of an optical grease connector with refractive index $n_{Connector} = 1.60$. 205

B.2 Transmission coefficient results for varying connector size and fibre misalignment from Monte Carlo simulation for an air gap connector of refractive index $n_{Connector} = 1.00$. 206

CHAPTER 1

Introduction

The use of scintillation detectors with wavelength shifting (WLS) fibre readout was first developed for both electromagnetic and hadronic calorimetry [1]. The development of large area scintillator tiles with WLS fibre readout which are sensitive to the passage of single minimum ionizing particles (MIPs) is a new application of this technique, and has been successfully implemented with the OPAL detector's Tile Endcap (TE) subdetector.

The installation of TE enhances the trigger capabilities in the endcap region by providing valuable redundancy necessary to maintain efficient triggering in the presence of higher beam backgrounds expected at LEP2. The principle design constraints of TE included the limited space available in the endcap region for detector placement as well as signal cable readout, along with the need for adequate light output.

The simulation of scintillating tiles with complex arrangements of WLS fibre readout is presented in this thesis with emphasis on the performance of the prototype and final TE tile designs.

Firstly, an overview of the LEP accelerator and OPAL detector is presented in Chapter 2. A description of the accelerator conditions at LEP2 which impact upon the performance of OPAL is given. The need for a subdetector in the endcap region capable of providing high efficiency for the detection of MIPs as

well as a fast trigger signal which can be used by the rest of the OPAL detector is demonstrated.

Chapter 3 provides a detailed description of Tile Endcap (TE) detector indicating the various design constraints. A discussion of the general characteristics of scintillator materials follows in Chapter 4. Here it is demonstrated that a geometric optics approach is sufficient to accurately describe the propagation of light in WLS fibres, and therefore scintillator-WLS fibre detector systems.

The current state of the simulation software available required that I develop a suite of programs which simulate both the scintillation and wavelength shifting mechanisms, as well as transport of photons through the WLS fibre geometry. Furthermore, routines were written which permitted the description of complex layouts of WLS fibres such as those found in the TE detector. These and other software simulation issues are presented in Chapter 5.

The first test of the new simulation software successfully predicted the distribution of photons in the cross-section of a WLS fibre which I measured using a high resolution CCD array. The measurement and simulation considerations are given in Chapter 6.

The simulation was then applied to describe the response of the three sigma fibre prototype tile to the passage of MIPs. This is presented in Chapter 7. Both the average photoelectron output and uniformity of response were determined by comparing the Monte Carlo with measured results obtained from a cosmic ray telescope.

Finally, in Chapter 8 the simulation is extended to describe the final design TE Tile 2 sector. The Monte Carlo is compared with data obtained for MIPs from $\mu^+ \mu^-$ events in terms of the average photoelectron yield as well as the uniformity

of response across the face of the TE Tile 2.

CHAPTER 2

Experimental Apparatus

2.1 The Large Electron-Positron (LEP) Collider

At CERN, the European Laboratory for Particle Physics, the current main operating facility is LEP, the Large Electron Positron collider. In LEP electrons and positrons circulate in opposite directions and can collide at up to eight interaction points situated around the 27 km circumference underground storage ring. The LEP accelerator depends upon the other CERN accelerators to provide it with the necessary electron and positron beams. A schematic of the accelerator complex which supplies electron and positron beams to LEP is shown in Figure 2.1.

The source of electrons and positrons for LEP is LIL (Linear Injector for LEP), where electrons are accelerated to an energy of 200 MeV. Positrons are created by directing the electron beam onto a target. The second stage of LIL accelerates the leptons to 600 MeV, and are then injected into the EPA (Electron-Positron Accumulation) ring. Located directly in front of LIL, the EPA stores and compresses the electron and positron beams via synchrotron damping until the positrons are accumulated into 8 bunches.

When the bunches are of sufficient intensity they are injected into the PS (Proton Synchrotron) ring and accelerated to 3.5 GeV. From the PS the bunches are transferred to the SPS (Super Proton Synchrotron) and accelerated to 20 GeV.

Finally, the electron and positron bunches are alternately injected counterclockwise and clockwise, respectively, into the main LEP ring until a sufficient current per beam is achieved.

Between 1989 and 1995, the lepton beams were accelerated in LEP1 to energies of about 45 GeV using conventional radio frequency (RF) cavities, producing collisions of center of mass energies near the Z^0 resonance. The addition of 60 superconducting RF cavities late in 1995, and a further 84 superconducting RF cavities early in 1996, boosted the beam energies to approximately 70 GeV and 80.5 GeV respectively, and marked the beginning of LEP2 operations. The latter increase pushed LEP above the energy threshold necessary for production of W^+W^- pairs. Running concluded in 1996 with a total of 178 superconducting RF cavities in place yielding energies of 86 GeV per beam. The addition of 32 superconducting RF cavities in 1997 provided energies of 92 GeV per beam. A more detailed discussion of the operational differences between LEP1 and LEP2 will be provided in section 3.1.

Situated at four of the eight potential interaction points around the LEP ring are the experiments ALEPH, DELPHI, L3, and OPAL. Figure 2.1 shows the locations of the experiments, as well as the directions in which the electron and positron beams travel. Electrostatic separators keep the beams from colliding at the interaction points where no detectors are situated. While the experimental halls and RF cavities are located in eight straight sections around the LEP ring, dipole magnets are contained in the adjoining curved sections in order to guide the beams. Quadrupole magnets distributed throughout the ring are used to maintain beam focus.

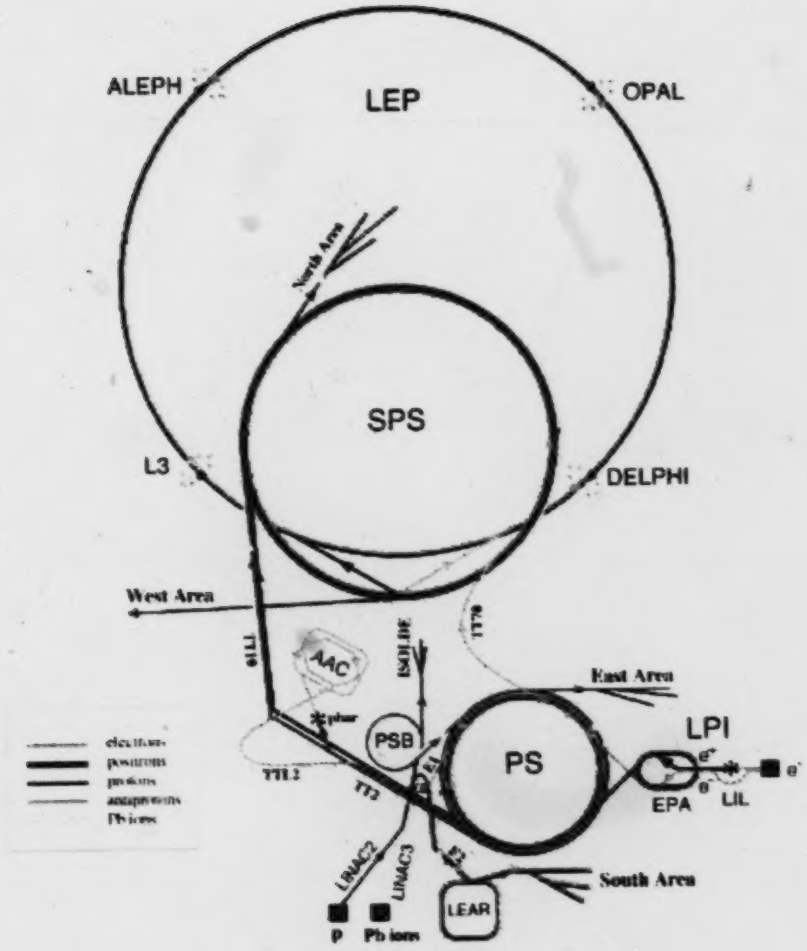

Figure 2.1: Shown above is accelerator complex which provides the electron and positron beams to the four LEP experiments.

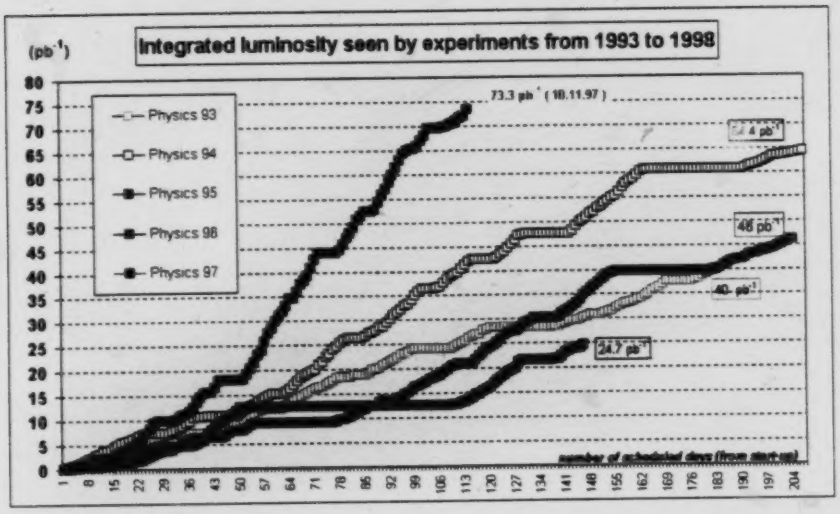

Figure 2.2: Shown above is integrated luminosity delivered to the four LEP experiments for each year of operation, as a function of scheduled days from start up.

Each experiment at LEP observed a reaction rate R given by

$$R = \mathcal{L}\sigma \tag{2.1}$$

where $\mathcal{L}$ is the luminosity (in units of $\mathrm{cm}^{-2}\mathrm{s}^{-1}$) and σ is the cross section (in units of cm^2) for any given process. The luminosity of an e^+e^- storage ring depends upon the beam characteristics and is given by

$$\mathcal{L} = \frac{fnN_1\ N_2}{4\pi\sigma_x\sigma_y} \tag{2.2}$$

where f is the bunch circulation frequency, n is the number of bunches per beam, N_1 and N_2 are the number of particles per bunch for each beam, and σ_x and σ_y are the horizontal and vertical bunch dimensions.

Often quoted as a measure of the accelerator performance is the integrated

luminosity L delivered to the experiments, and is the time integral of the luminosity given by

$$L = \int_t \mathcal{L}\, dt \tag{2.3}$$

Between 1990 and 1993 an integrated luminosity of 93.5 pb^{-1} (1 pb = 10^{-36} cm^2) was delivered to the LEP experiments. Figure 2.2 shows the integrated luminosity delivered by LEP during operations from 1993 to 1998. The luminosity received by each experiment is determined by measuring the rate of small-angle elastic electron-positron scattering, also known as Bhabha scattering. Since this is a pure electroweak process, the cross section for Bhabha scattering can be precisely calculated. It is ideally suited for determination of the luminosity via equation 2.1, the measured rate and the calculated cross-section corrected for the geometric acceptance of the detector.

2.2 The OPAL Detector

Shown in Figure 2.3, the OPAL (**O**mni-**P**urpose **A**pparatus for **L**EP) detector [2] is a large cylindrical device approximately 5 m in radius and 12 m in length, designed to give nearly complete acceptance for e^+e^- interactions over the entire 4π solid angle.

The detector is composed of a number of subsystems designed to provide precise measurements of charged particle trajectories and electromagnetic and hadronic energies for a wide variety of events. The main components are a central tracking system enclosed in a solenoidal magnet, a lead glass electromagnetic calorimeter, a time of flight system, a hadron calorimeter and muon detectors. A forward detector system is used to measure the luminosity and identify particles

emitted at small angles with respect to the beam line. The time of flight system, particularly the time of flight endcap (TE) detector, will be described in some detail as it is directly related to the work presented here. The other detector components are covered below.

2.2.1 The Central Detector

The Central Detector (CD) consists of a Silicon Microvertex detector and three drift chamber devices: the vertex detector, jet chamber and surrounding Z-chambers. Each of the detectors are situated inside a pressure vessel holding a pressure of 4 bar. The gas mixture used in all 3 detectors consists of a mixture of argon (88.2%), methane (9.8%) and isobutane (2%). The central detector is contained in a solenoid supplying a uniform axial magnetic field of 0.435 T. The magnet of the OPAL detector consists of a self-supporting, water-cooled aluminum coil and and iron yoke which is segmented for use as a hadron calorimeter. This magnet provides a field uniform to about $\pm$ 0.5 % within the central tracking volume.

The inner wall of the pressure vessel at 7.8 cm radius consists of 0.13 cm thick carbon fibre with a 100μm aluminum inner lining. Interior to the pressure vessel at a radius of 5.35 cm is a 0.11 cm thick layer of Beryllium with the Silicon Microvertex detector inserted between the two layers.

Information from each detector is analyzed separately offline to perform track reconstruction. The resulting track segments from each detector are then merged, with a combined track fit performed using the hit coordinates of each detector.

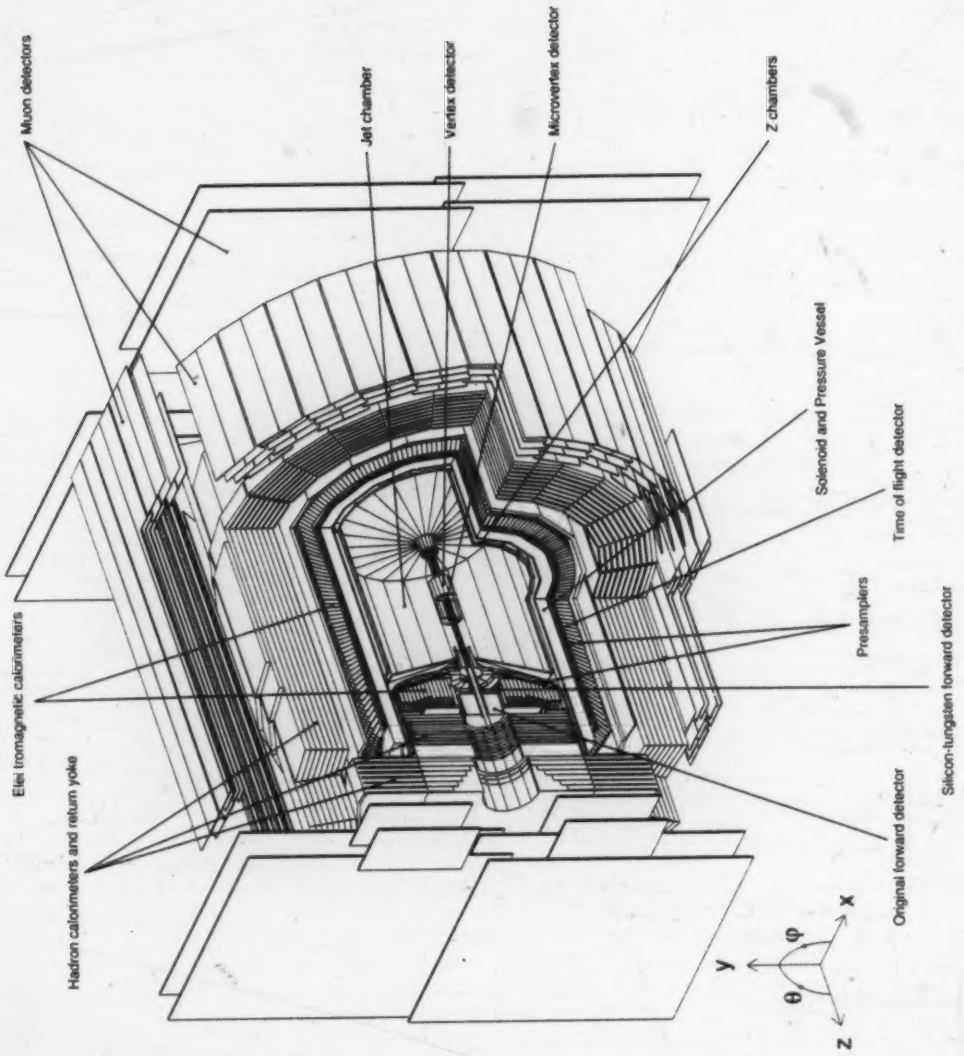

Figure 2.3: Shown above is a three dimensional cut-away view of the OPAL Detector.

Silicon Microvertex Detector

The purpose of the Silicon Microvertex Detector (SI) [3] is to provide a precise measure of the position of secondary vertices located close to the interaction point. The secondary vertex marks the point of decay for a long lived particle that has been produced at the e^+e^- interaction point (primary vertex). A precise determination of the secondary vertex can provide an accurate measure of particle lifetimes, and assist in the identification and classification of heavy quark decays.

The SI detector consists of two barrels of double sided silicon wafers at radii of 6.1 and 7.5 cm from the beam, as shown in Figure 2.4. Each silicon wafer is 33 mm × 60 mm in dimension and are connected end to end to form either 2 or 3 wafer arrangements called ladders. The inner layer consists of 12 two wafer ladders at the -z end and 12 three wafer ladders at the +z end of the detector. The outer layer consists of 15 two wafer ladders and 15 three wafer ladders at the -z and +z detector ends respectively. Both inner and outer layers provide coverage of the interaction region with five silicon wafers longitudinally, with the interaction point located at the center of the five wafers. Overlap in the ϕ direction of the inner and outer layers, as shown in Figure 2.5, is performed in order to eliminate any possible gaps in coverage.

Each silicon wafer strip detector is of 250 μm thickness, and contains 629 implant strips at a pitch of 25 μm for both ϕ and z detectors. The ϕ detectors have the implant strips pointing in the z direction on the inner side of the wafer, while the z detectors have the implant strips pointing in the ϕ direction on the outer side. Since more than one channel is read out on the same line, the effective pitch values for the ϕ and z detectors are 50 μm and 100 μm respectively. The front end electronics that read out the detectors are located on 300 μm thick ceramic circuit

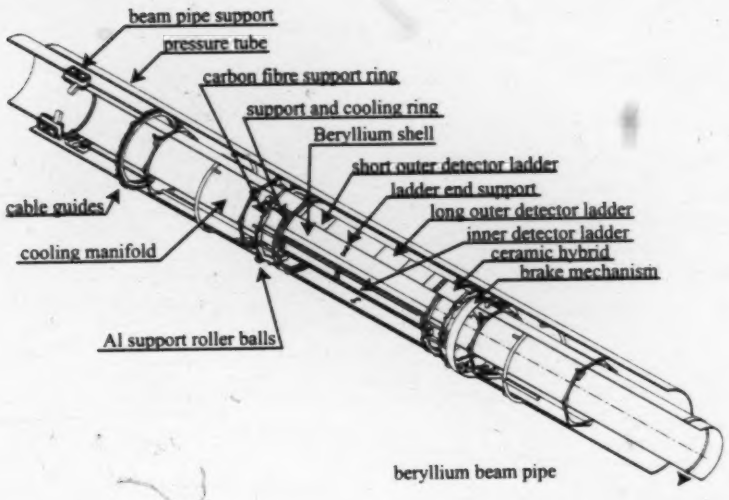

Figure 2.4: Shown above is a cutaway view of the OPAL Silicon Microvertex detector.

boards at the end of each ladder. The z detector strip signals are also brought to the front end electronics via a gold printed circuit on a borosilicate glass support.

The analog signals from the detector strips are removed from the detector to be processed by 28 Digital Signal Processor (DSP) units in Fastbus SIROCCO IV modules. The DSP's apply a clustering algorithm to determine charge clusters in the detector channels. The deadtime of the SI detector, primarily from the analog readout and digitization sequence in the SIROCCO modules, is on the order of 1.6 ms for a trigger rate of 4-10 Hz.

The resolution of the SI detector has been measured by considering the impact parameter (d_0) resolution for dilepton events. For the process $Z^0 \rightarrow \mu^+\mu^-$, the SI detector has been shown to measure d_0 with a resolution of 18 μm in the $r-\phi$ plane, and 100 μm in z.

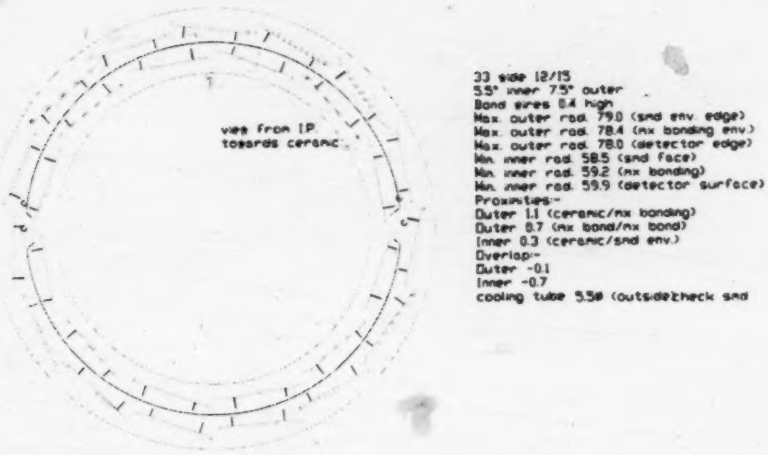
view from IP
towards ceramic
33 wide 12/13
5.5° inner 7.5° outer
Bond areas 0.4 high
Max. outer rad. 79.0 (snd env. edge)
Max. outer rad. 78.4 (mx bonding env.)
Max. outer rad. 78.0 (detector edge)
Min. inner rad. 58.5 (snd face)
Min. inner rad. 59.2 (mx bonding)
Min. inner rad. 59.9 (detector surface)
Proximities:-
Outer 1.1 (ceramic/mx bonding)
Outer 0.7 (mx bond/mx bond)
Inner 0.3 (ceramic/snd env.)
Overlap:-
Outer -0.1
Inner -0.7
cooling tube 5.50 (outside?check snd

Figure 2.5: Shown above is a cross-sectional view of the OPAL Silicon Microvertex detector.

Vertex Detector

The vertex detector (CV) [2, 4] is a high precision cylindrical drift chamber that is used to locate the primary vertex of the event, assist in the location of decay vertices of short-lived particles, and to improve the momentum resolution of charged tracks. Figure 2.6 shows a schematic view of the vertex detector. It is 100 cm long with inner and outer radii of 8.8 and 23.5 cm respectively. The detector consists of two layers of 36 sectors each. The inner layer contains the axial sectors, each containing a plane of 12 anode or sense wires strung parallel to the beam direction. The wires range radially from 10.3 to 16.2 cm with a spacing of 0.583 cm. The outer layer contains the stereo sectors each containing a plane of 6 sense wires inclined at a stereo angle of $\sim 4°$. The stereo wires lie between the

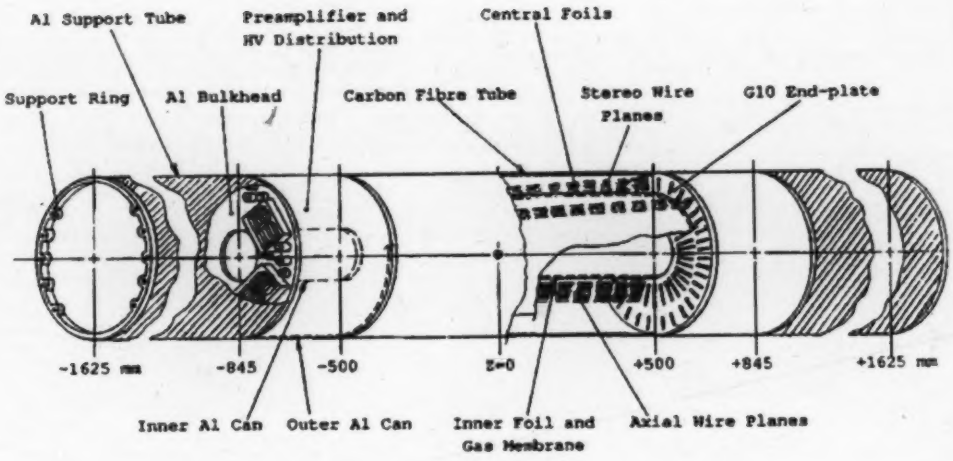

Figure 2.6: Schematic view of the OPAL vertex detector.

radii 18.8 and 21.3 cm with a spacing of 0.5 cm.

Figure 2.7 shows the wire layout for a section of the vertex detector. The axial and stereo wires together provide angular coverage in the region of $23° \leq \theta \leq 157°$ amounting to 92 % of the 4π solid angle. The chamber wires are strung between two 32 mm thick G10 fibreglass end plates that are held 1 m apart by a single 1.5 mm thick carbon fiber tube located at the detector outer radius. The preamplifiers and high voltage distribution components are mounted onto the G10 endplates, and are enclosed within a gas-tight container defined by two aluminum cylinders and an aluminum bulkhead.

Each anode wire defines a drift cell, of which there are 648 in total. Ionization from a charged particle passing through the cell is collected at the anode wire. The anode and potential wires are 20 μm diameter gold plated W-Rh and

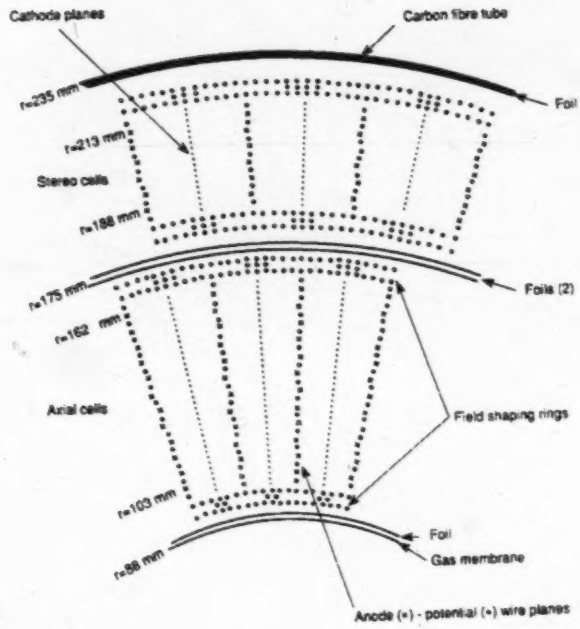

Figure 2.7: Wire layout for a section of the OPAL vertex detector in the $r-\phi$ plane.

200 μm diameter gold plated Cu-Be respectively, while the cathode planes use 125 μm Cu-Be wires spaced 1 mm apart. The cathode planes form the boundaries between adjacent sectors and help shape the electric fields on the anode wire surfaces. Each drift cell is bidirectional, meaning that electrons drift to the anode wires from both sides of the anode wire planes. Therefore, all of the anode wires are offset from the plane defined by the potential wires by an alternating stagger of $\pm$ 41 μm in order to resolve the ambiguity as to whether a particle passed to the right or left side of the wire plane. There is also an additional bowing of the anode wires by 50-100 μm due to electostatic forces when voltage is applied to the chamber.

The electrostatic field conditions in a cell delimit the performance of the vertex detector. Both the anode surface fields and drift fields are determined by the voltages applied to the cathode planes and potential wires. The anode wires are fixed at ground potential. The voltages are chosen to provide a uniform electric field over most of the drift cell with the field lines perpendicular to the anode wire planes. Within any given anode wire plane, the potential wires are all kept at the same voltage to ensure a uniform gas gain for all anode wires. The vertex chamber is operated at a drift field of 2.5 kV/cm and an anode surface field of 360 kV/cm, resulting in a drift velocity of 39.5 μm/ns in the central detector gas. A single hit efficiency of about 97% along with an average spatial resolution of about 55 μm in the r-ϕ plane is achieved with the vertex detector under these operating conditions. The anode surface field value has been chosen to maximize the detector efficiency and resolution, and to maintain the electrostatic properties and lifetime of detector.

Both ends of each anode wire are connected to preamplifiers on the chamber end plates, and the signals are then fed to CFD's (constant fraction discriminators). The outputs from each wire are combined in a mean timer to obtain a measurement of the electron drift time. The mean value for each cell is passed to a TDC (time to digital converter) with a bin width of 0.67 ns, corresponding to a drift distance of 26 μm. This TDC value is then used offline to calculate where the particle passed through the drift cell in the $r-\phi$ plane. The maximum drift distance is approximately 1.5 cm, and limits the effects due to diffusion. Furthermore, the difference in arrival times of the signals from each wire end is determined to an accuracy of 0.1 ns, yielding a rough z coordinate measurement with a resolution on the order of 4 cm. While this information is used in the trigger, a more precise z measurement resolution of 700 μm is obtained during the

offline tracking analysis which utilizes both the axial and stereo cell information. The vertex detector is capable of achieving a two particle separation of about 2 mm due to the pulse shortening of the anode signals in the readout electronics, thereby reducing the detector deadtime to about 40-50 ns.

Jet Chamber

The jet chamber (CJ) [2, 5] is a 400 cm long cylindrical drift chamber with inner and outer radii of 25 cm and 185 cm respectively. The chamber records the tracks of charged particles and measures their momentum. Particle identification is achieved through multiple sampling of the energy loss $\mathrm{d}E/\mathrm{d}x$ in the central detector gas. The chamber consists of 24 identical azimuthal sectors each containing a anode wire plane of 159 wires equally spaced 1.0 cm apart strung parallel to the beam direction. As in the vertex chamber, cathode wire planes form the boundaries between adjacent sectors with the anode wires staggered by $\pm$ 100 μm, alternately to the left and right side of the plane defined by the potential wires, to resolve the left-right ambiguity. The anode wires are at ground potential, and lie between radii of 25.5 and 183.5 cm, alternating with potential wires. The maximum drift distance varies from 3 cm for the innermost radial wires to 25 cm for the outermost wires. The wires are strung between 2 conical endplates which are supported by 24 hollow aluminum panels located at the outer radius of the chamber. Within the range $43° \leq \theta \leq 137°$ up to 159 points can be measured along each track, and at least 8 points on a track are obtained over 98 % of the 4π solid angle.

The output signal from both ends of each anode wire are passed through preamplifiers mounted on each of the chamber endplates, and then digitized with

100 MHz flash analog to digital converters (FADCs). The 80 FADC crates provide high speed sampling of the anode signals, greatly improving the drift time measurements and two particle separation resolution. The digitized data is read out into 20 microprocessors for further online data reduction and track finding, and for use in the trigger. Online pulse shape analysis of each wire hit by the microprocessors provides a measurement of the drift time and charge collected at each anode wire end, which are used to determine the coordinates of wire hits in the $r-\phi$ plane and z directions respectively.

The jet chamber is operated with a gas gain of $\approx 10^4$ and a drift field of 890 V/cm, chosen to balance the requirements for good $\mathrm{d}E/\mathrm{d}x$ information and good z resolution. Obtaining good z resolution measurements through charge division requires a high gas gain in order to maximize the charge collected at the anodes, and therefore the ratio of signal to noise. This is opposite to the requirement for quality particle identification via $\mathrm{d}E/\mathrm{d}x$ which requires a low gas gain in order to minimize saturation effects. Saturation effects increase with gain and are due to ion screening of the anode electric field early in the ionization avalanche, thereby reducing the gas gain and total charge produced by the avalanche, and degrading the resolution of the $\mathrm{d}E/\mathrm{d}x$ measurement.

From a study of $\mathrm{e^+e^-} \rightarrow \mu^+\mu^-$ events the $r-\phi$ resolution was determined to be 135 μm with a mean drift distance of 7 cm. The average z resolution measurement via charge division is 10 cm. The momentum resolution for charged particles in the region $|\cos\theta| < 0.7$ is given by

$$(\frac{\sigma_p}{p})^2_{xy} = (0.02)^2 + (0.0015 p_{xy})^2 \qquad (2.4)$$

where p_{xy} is the measured particle momentum (units of GeV/c) in the x-y plane. The $\mathrm{d}E/\mathrm{d}x$ resolution for the $\mu^+\mu^-$ events is approximately 3.8%.

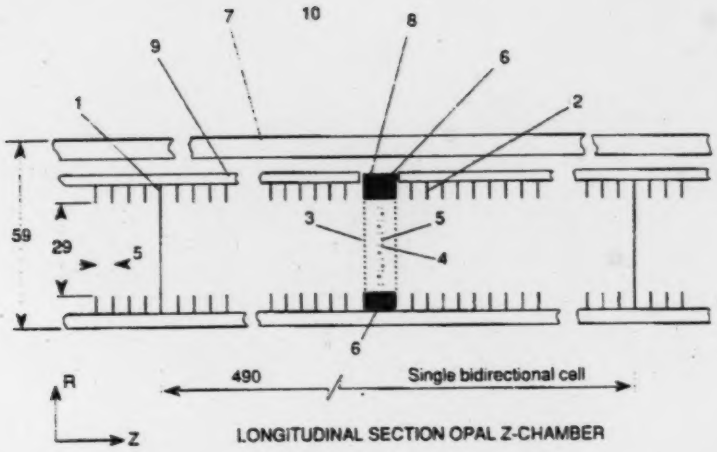

Figure 2.8: Cross-sectional view of a single Z chamber. The anode wires (6) are 50 cm long in the ϕ direction. All measurements shown are in mm.

Z-Chambers

The Z-chambers (CZ) [2, 6] consist of 24 drift chambers each 400 cm long, 50 cm wide and 5.9 cm thick. The chambers are mounted onto the hollow aluminum panels of the jet chamber support structure, at a radius of 1.93 m from the beamline. Coverage of 94% of the azimuthal angle and the polar angle range $|\cos(\theta)| < 0.72$ is provided by the 4 m long barrel structure. Each chamber is divided along the z direction into 8 bidirectional cells of 50 cm$\times$50 cm, with every cell containing 6 anode sense wires spaced at 0.4 cm at increasing radius and a stagger of ± 250 μm from the potential wire plane. A cross-sectional view of a single Z chamber is shown in Figure 2.8.

The anode and potential wires are mounted onto a separate G10 window-frame structure which also contains two planes of edge mounted grid wires ± 5 mm

from the potential wire plane. The grid wires isolate the anode region from the drift region, and help maintain a parallel and uniform drift field up to the grid wire plane. The grid wires also assist in establishing the electric field at the anode wires. Each chamber has a maximum drift distance of 25 cm in the z direction. A drift field of 800 V/cm is achieved from a maximum drift voltage of about 20 kV. The anode wires are read out at each end using FADCs identical to those used in the jet chamber readout. The ϕ coordinate of each anode wire hit is obtained by charge division. The measured Z chamber $r-\phi$ and z position resolutions are about 1.5 cm and 300 μm respectively.

2.2.2 Time-Of-Flight Counters

The time-of-flight (TOF) system provides a measurement of the time taken for a charged particle to traverse the detector from the interaction point, and as such provides particle identification in the momentum range of 0.6 - 2.5 GeV/c. The TOF system also provides fast triggering information and an effective rejection of cosmic rays by acting as a veto to events which are not synchronized with the beam crossing. TOF detectors are situated in both the barrel and endcap regions of OPAL.

The barrel TOF detector [2] consists of 160 scintillation counters forming a barrel layer 684 cm long at a mean radius of 236 cm surrounding the OPAL magnet coil. The barrel detector provides coverage in the polar angle range $|\cos\theta| < 0.82$. Each counter is 6.840 m long and 45 mm thick with a trapezoidal cross section, ranging from 89 to 91 mm in width. The counters are individually wrapped in aluminised mylar foil and a black PVC sheet. Light collection occurs at both

ends of each scintillation counter via 300 mm long conical and cylindrical plexiglas lightguides glued directly to photomultiplier tubes. The analog signal from each phototube is divided and sent to both a charge integrating analog to digital converter (ADC) as well as constant fraction discriminator (CFD). The CFD output is directed to both an 11-bit TDC (50 ps/count) and a mean timer which produces signals for input into the trigger system.

Typical timing resolutions of between 300 and 400 picoseconds, depending on the z position along the counter, are determined by measuring the time of flight for muons from the decay $Z^0 \rightarrow \mu^+\mu^-$.

In 1996 the Tile Endcap (TE) [7] system was added to enhance the triggering information available from the endcap region, and to aid in the identification of which bunches in a bunch train are responsible for a particular observed collision. The TE detector consists of a 10 mm thick BC-408 plastic scintillator layer divided into tiles and placed between the endcap presampler and the endcap electromagnetic calorimeter. The TE detector extends from the edge of the barrel TOF scintillators at $|\cos\theta| = 0.82$ down to the limit of particle tracking provided by the central drift chambers at $|\cos\theta| = 0.95$. The scintillation light produced from the passage of a charged particle is absorbed and reemitted inside the embedded wavelength shifting (WLS) fibre, which then transports the light via coupled optical fibres to photomultiplier tubes situated approximately 15 m outside the endcap region.

The design characteristics and performance of the TE detector will be covered in detail in Chapter 3.

2.2.3 Electromagnetic Calorimeter

The function of the electromagnetic (em) calorimeter [2] is to detect and identify electrons, positrons and photons with energies ranging from tens of MeV to 100 GeV, and to accurately measure their energies and positions. Discrimination between neutral pions and photons is provided, along with electron-hadron discrimination when used in cooperation with the central tracking system. The calorimeter consists of three large overlapping assemblies of SF57 lead glass blocks, split into a barrel and two endcap arrays, covering 89 % of the solid angle.

The barrel calorimeter (EB) consists of a cylindrical array of 9440 lead glass blocks at a radius of 2.46 m outside the magnet coil, providing coverage over the complete azimuthal angle and the polar angle range $|\cos\theta| < 0.82$. Each block is approximately 10 cm x 10 cm in cross section and 37 cm in depth corresponding to 24.6 radiation lengths of material, and is angled to point at the interaction region, thereby maximizing detection efficiency and minimizing electromagnetic shower leakage from the back of the calorimeter. The blocks are tilted slightly from a perfectly pointing geometry to prevent particle losses in the gaps between blocks. Čerenkov light from the passage of relativistic charged particles through the lead glass is detected by a 3 inch diameter magnetic field tolerant phototube at the base of each block. Without any material in front of the calorimeter, the intrinsic energy resolution of the barrel detector for a traversing particle of energy E has been measured to be

$$\frac{\sigma_E}{E} \simeq 0.2\% + \frac{6.3\%}{\sqrt{E}} \tag{2.5}$$

The resolution degrades by almost a factor of 2 when considering the presence of absorbing material in the detector directly preceding the calorimeter. The intrinsic spatial resolution for a 6 GeV electron beam has been measured to be on

the order of 11 mm.

The endcap electromagnetic calorimeter (EE) consists of two dome-shaped arrays, each of 1132 CEREN-25 lead glass blocks, located between the pressure bell of the central tracking system and the pole tip hadron calorimeter and provides full azimuthal coverage over the polar angle range $0.81 < |\cos\theta| < 0.98$. Arranged to follow the contours of the pressure bell, the lead glass blocks were manufactured in lengths of 38, 42, and 52 cm and positioned coaxial with the beam axis. The blocks in the endcap calorimeter represent approximately 22 radiation lengths of material on average for all particles emerging from the interaction region. Since the blocks are operating in the full OPAL magnetic field, they are read out using a special single stage photomultiplier known as a Vacuum Photo Triode (VPT). The intrinsic energy resolution of the electromagnetic endcap calorimeter has been measured to be $\simeq 5\%/\sqrt{E}$ for low energy particles. The intrinsic spatial resolution is similar to that achieved by the barrel electromagnetic calorimeter.

The presence of approximately 2 radiation lengths of material in front of the electromagnetic calorimeter, mostly due to the solenoid and pressure vessel, results in most electromagnetic showers initiating prior to reaching the lead glass. Presampling devices are therefore installed in the barrel and endcap regions directly in front of the lead glass. The presamplers measure the position and energy of showers and act to improve the overall spatial and energy resolution. This improvement is due to the fact that the hit multiplicity measured in the presampler is approximately proportional to the number of charged shower particles entering the device, and therefore proportional to the energy deposited in front of the presampler. The presamplers also provide additional photon-neutral pion and electron-hadron discrimination.

The Barrel Electromagnetic Presampler (PB) [2, 8] consists of 16 chambers arranged on a cylinder of radius 2.388 m and length 6.623 m covering the polar angle range $\cos\theta < 0.81$. Each chamber consists of two layers of drift tubes each having a cross section of 9.6 mm^2 square, with the anode wires running parallel to the beam direction. Both sides of each layer of tubes contains 1 cm wide cathode strips at $\pm 45°$ to the wire direction. The drift tubes are operated in the limited streamer mode using a gas mixture of 68% carbon dioxide and 32% n-pentane. Spatial positions perpendicular to the electromagnetic shower direction are determined by reading out the cathode strips, with an intrinsic resolution of 2 mm for a minimum ionizing particle (MIP). The charge collected at both ends of each wire is used to provide a z coordinate measurement with a resolution of about 10 cm by charge division.

The Endcap Electromagnetic Presampler (PE) [2, 9] is an umbrella shaped arrangement of 32 chambers in 16 sectors located in the region between the pressure bell and the endcap electromagnetic calorimeter, covering the full ϕ angle and the polar angle range $0.83 < |\cos\theta| < 0.95$. Each sector contains one large and one small thin trapezoidal multiwire proportional chamber operating in high gain mode. The large chambers are inclined at an angle of 18° with respect to the plane perpendicular to the beam direction in order to follow the shape of the pressure bell and lead glass blocks, while the small chamber is at 90° to the beam axis. Complete coverage of the endcap region is obtained by the overlap of neighboring sectors. Coverage at the inner radius is prevented by geometrical constraints.

Simultaneous readout of groups of 4 wires and strips provide hit positions for showers and MIPs, with a spatial resolution of about 2 mm. When used in concert with the electromagnetic calorimeter the shower spatial resolution improves to about 2 mm and 2-5 mm for the barrel and endcap detectors, respectively.

2.2.4 The Hadron Calorimeter

The hadron calorimeter [2] is used to measure the energy of hadrons emerging from the electromagnetic calorimeter and assists in the identification of muons. The hadron calorimeter also serves as the return yoke for the magnetic field of the coil, and is divided into the barrel, endcap and pole-tip sections.

The barrel region (HB) is 10 m long with an inner radius of 3.4 m and outer radius of 4.4 m, and surrounds the electromagnetic calorimeter, covering the polar angle range of $|\cos\theta| < 0.81$. The barrel calorimeter contains 8 layers of 10 cm thick iron separated by 2.5 cm gaps. An additional 2 iron layers cover the central 4 m section of the barrel to increase the amount of material encountered by an emerging particle in this region. Placed within the gaps are a total of 9 planes of limited streamer tube chambers which operate using a gas mixture of 75 % isobutane and 25 % argon. The chamber anode wires, which run parallel to the beam axis, are spaced 1 cm apart and are used for monitoring purposes only. Located on the outer and inner surfaces of the chambers are pads and 0.4 cm wide aluminum strips which run the full length of the chamber, directly above the anode wire positions. Induced charge collected on the pads and strips produce the analog chamber signals. Hadron calorimeter towers which point towards the interaction region are formed from the grouping of layers of pads, thereby dividing the detector volume into 48 bins in ϕ and 21 bins in θ. The summed pulse height for each tower is recorded by ADCs, while the cathode strip signals are digitally recorded.

Toroidal shaped hadronic endcaps (HE) close off the barrel ends, and consist of 7 layers of 10 cm thick iron, covering the angular region $0.81 < |\cos\theta| < 0.91$. The layers of iron are separated by 3.5 cm gaps, and are also instrumented

with limited streamer tube chambers.

The hadron calorimetry coverage is extended to the region $0.91 < |\cos\theta| < 0.99$ with the hadronic pole-tip calorimeter [2, 10], placed between the endcaps of the hadron and electromagnetic calorimeters. A total of nine layers of 8 cm thick iron are separated by 1.0 cm gaps, instrumented with thin multiwire proportional chambers operating in a high gain mode using a mixture of 55 % carbon dioxide and 45 % n-pentane gas. The purpose of the increased number of sampling layers in this region is to provide an improved energy resolution in the forward direction of the detector. Each of the ten chambers has cathode pads on one side, with areas of typically 500 cm^2, and 2.5 cm wide strips on the other side which fan out radially nearly perpendicular to the 50 μm anode wires. The pad size matches the width expected for a hadronic shower. The pads from the ten layers of chambers are also grouped to form hadron calorimeter towers which point towards the interaction region.

For all three detector regions the chamber strip hits provide muon identification and tracking information, with position measurements possible to an accuracy determined by the anode wire spacings. Summation of the pad signals within a tower provide an estimate of the energy of a hadronic shower. The energy resolution of the electromagnetic and hadron calorimeters combined varies from $100\ \%/\sqrt{E}$ for particle energies below 15 GeV to $140\%\ /\sqrt{E}$ at 50 GeV.

2.2.5 Muon Detector

The goal of the muon detector [2] is to identify muons from a hadronic background. The muon detector consists of a barrel and two endcap detectors covering 93 % of the solid angle.

The muon barrel (MB) consists of 110 drift chambers that cover the acceptance $\cos\theta < 0.68$ with four chamber layers and $\cos\theta < 0.72$ with one or more chamber layers. The chambers, which operate using a gas mixture of 90 % argon and 10 % methane, range in length between 10.4 m and 6 m in order to fit between the magnet support legs, and all have the same cross sectional area of 120 cm×9 cm. Each chamber is split into two bidirectional drift cells each containing a 50 μm diameter anode signal wire running the full length of the cell parallel to the beamline. Defining the drift field in the cell are 0.75 cm wide cathode strips etched onto the inner surface of the chamber. Directly opposite the anode wires are diamond shaped cathode pads [11] which run the entire length of the chamber. The electron drift velocity in the cell is 33 mm/μs with a maximum drift distance of 29.7 cm from either side of the anode wire.

The spatial position in the $r-\phi$ plane is determined using the drift time onto the anode wire, and can be reconstructed to an accuracy of better than 0.15 cm. By using the difference in time and pulse height of the signals arriving at both ends of the anode wire, a rough estimate of the z position can be found. The most accurate measure of the z position is achieved by examining the induced charge on the two sets of diamond shaped cathode pads, and determines the z hit coordinate to an accuracy of 0.2 cm.

Each endcap of the muon detector (ME) consists of two layers of four 6 m ×6 m square quadrant chambers, and two layers of two 3 m×2.5 m patch chambers, providing coverage in the angular range $0.67 < |\cos\theta| < 0.985$. All chambers are situated in a plane perpendicular to the beam direction. Each chamber contains two layers of limited streamer tubes separated by 19 mm where one chamber layer has its wires horizontal and the other vertical. Inside each 0.9 cm×0.9 cm streamer tube unit 100 μm diameter anode wires are spaced every

1.0 cm, and run the full length of the chamber. These tubes operate with a gas mixture of 75 % isobutane and 25 % argon.

Each plane of tubes is open on one side and closed on the other to rows of 0.8 cm wide aluminum cathode strips which on the open side run perpendicular to the tube anode wires, and on the closed side run parallel to the anode tube wires. From an examination of the pulse heights of signals arriving from the strips on the open side, the position of the avalanche on each wire can be determined to an accuracy of about 1 mm. The strips on the closed side provide only a rough estimate of the hit position with an accuracy of 3 mm.

Muon identification requires the extrapolation of the track seen in the central tracking system through the absorber material of the hadron calorimeter, taking into account energy loss and multiple coulomb scattering, and matched with tracks found in the muon detector. Multiple scattering of the highest muons of interest determines a spatial accuracy of about 2 mm as necessary to associate tracks from the central detector with those in the muon chambers, and is well matched by the precision measurements capable of the barrel and endcap chambers.

2.2.6 The Forward Detectors and Si-W Calorimeter

A measure the luminosity delivered by LEP to the OPAL experiment is provided through the observation of the low angle Bhabha scattering event rate. This measurement is achieved using both forward detectors (FD) [2, 12] and the Silicon-Tungsten Calorimeter (SW) [13].

Shown in Figure 2.9, the two forward detectors are located immediately

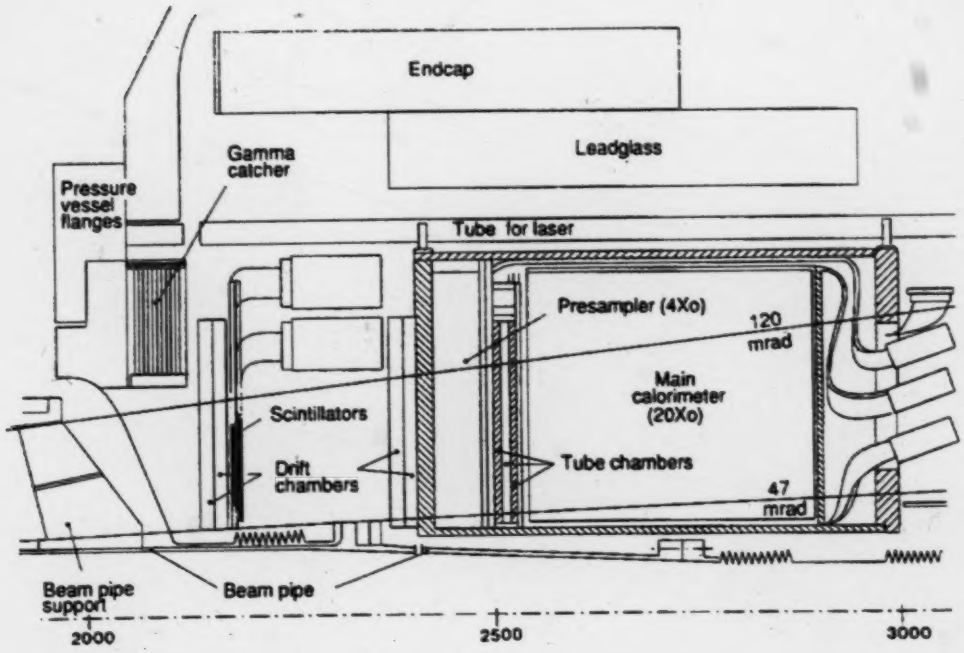

Figure 2.9: Cross sectional view of the OPAL forward detector situated between 2 and 3 m from the interaction region.

after the pressure bells of the central detector, and fill the holes at the center of each electromagnetic endcap calorimeter, surrounding the beam pipe. The forward detectors can accept particles arriving from the interaction point at angles between 47 and 120 mrad, with the only obstructions being the 2 mm carbon fibre beam pipe and 2 mm of aluminum from the central detector pressure vessel.

Each detector consists of tube chambers and drift chambers situated directly in front of an electromagnetic calorimeter and surrounding a presampler device. The three layers of proportional tube chambers, along with the drift

chambers, measure the angles of the scattered electrons and positrons, and provide electromagnetic shower positions to an accuracy of 3 mm. The forward calorimeter consists of 35 sampling layers of plastic scintillator placed between layers of lead. The calorimeter is divided into 16 azimuthal segments, with the sampling layers readout via wavelength shifter to vacuum phototetrodes.

A ring of lead-plastic scintillator modules known as the gamma catcher provides coverage to remove a gap in the acceptance of the forward detectors between the inner edge of the electromagnetic endcap calorimeter and the start of the forward calorimeter. Mounted on either side of the beam pipe 7.85 m from the interaction region are the far forward monitor counters composed of small lead-scintillator calorimeter modules. The purpose of the far forward monitor is to detect electrons scattered in the range of 5 to 10 mrad that are deflected outwards by the low-beta quadrupole magnets.

In an effort to improve the luminosity measurement, in 1994 the Silicon-Tungsten calorimeter was installed in both OPAL endcap regions. Each detector is a sampling calorimeter located roughly 240 cm from the interaction point and provides angular coverage in the range of 25 mrad to 59 mrad.

Each calorimeter consists of 19 layers of silicon detectors placed between 18 layers of tungsten. Directly in front of each calorimeter is a bare layer of silicon to detect preshowering, with the next 14 silicon layers each behind 3.8 mm of tungsten, and the final 4 layers behind 7.6 mm of tungsten, corresponding to 1 and 2 radiation lengths of material respectively.

Each silicon layer consists of 16 wedge shaped silicon detectors, each covering 22.5° in ϕ and the radial region between 6.2 cm and 14.2 cm. The wedges are further subdivided into 64 individually readout pads in the $r - \phi$ plane. Adjacent

wedges within a layer are offset by 800μm in z, and consecutive layers are offset in ϕ by half a wedge in order to complete the coverage of the detector.

2.3 The Trigger and Online Data Flow

The OPAL trigger system is designed to provide high efficiency for the various physics reactions, and good rejection of backgrounds arising from cosmic rays, from interactions of the beam particles with the gas inside the beam pipe or the wall of the beam pipe, and from noise. Events are only recorded by the data acquisition system if they satisfy certain trigger conditions, and for runs > 3514, pretrigger conditions. Several independent conditions are imposed on the subdetector signals in order to trigger on physics reactions, providing a highly redundant and efficient trigger.

2.3.1 The OPAL Trigger

The trigger system [2, 14] of the OPAL detector divides the 4π solid angle into 144 bins, with 6 bins in θ and 24 bins in ϕ, to form what is known as the trigger matrix. Input to the trigger matrix is provided by the central tracking chambers, time of flight counters, electromagnetic calorimeter, hadron calorimeter, and muon chambers. The trigger information from the hadron calorimeter is not used in the overall trigger decision.

Subdetector trigger signals divide into the two categories of stand-alone signals (such as multiplicity counts or energy sums), and lower threshold signals from each of the bins in θ and ϕ. The trigger processor makes a decision by forming correlations in space between subdetectors in θ-ϕ together with the stand-alone

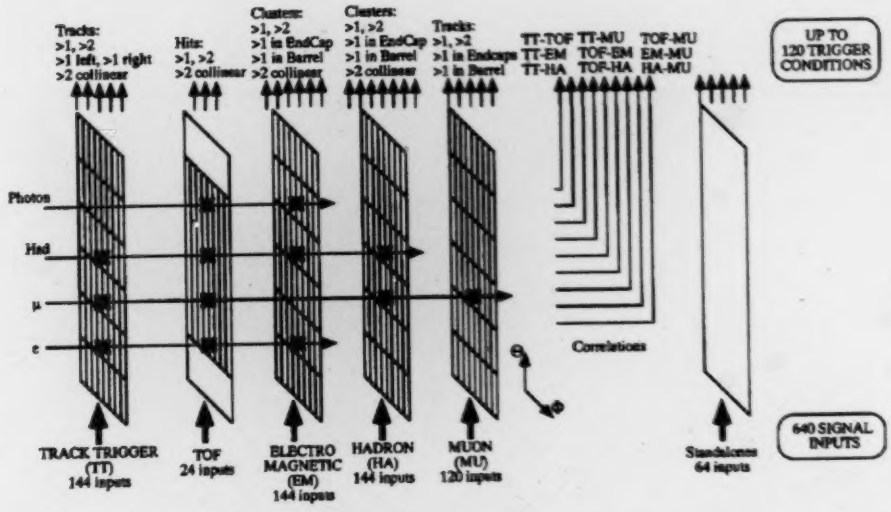

Figure 2.10: Overview of the trigger generation by the θ-ϕ matrix. A formal trigger decision is made from the various subdetector inputs. The sensitivity to various particle types is shown.

signals.

The trigger signals from the various subdetectors are logically combined in the central trigger logic. An overview of the trigger generation by the $\theta - \phi$ matrix is given in Figure 2.10.

The original OPAL trigger system was designed as a single stage trigger. With LEP1 running in 4+4 bunch mode (a detailed explanation of bunch modes can be found in Section 3.1.2), the time between a bunch crossing and a trigger decision summed with the required subdetector reset time was approximately 20 μs, less than the interbunch spacing of 22 μs or 45 kHz.

In 1992, a two-stage trigger system was implemented capable of operating under conditions with a greater bunch crossing rate than encountered in 4+4

mode. A new first stage pretrigger [15] performs an essentially deadtime-free first level decision to produce a pretrigger rate of 1-2 kHz while operating with the 90 kHz bunch crossing rate encountered with 8+8 Pretzel mode. The original trigger is essentially unchanged and acts as a second level trigger. Subdetector pretrigger signals, like the trigger signals, are divided into stand-alone signals from energy sums, and lower threshold signals from a reduced 1×12 bin segmentation in $\theta - \phi$. The pretrigger processor reaches a decision by performing multiplicity counting and attempts to form correlations in $\theta - \phi$ between subdetectors, and also uses the stand-alone signals.

The central trigger processor combines the information for all the individual subdetectors and the $\theta - \phi$ matrix and makes a decision to either accept or reject the event. Due to a high degree of redundancy in the trigger system, the efficiencies for the physics channels $e^+e^- \rightarrow$ hadrons, leptons, $\gamma\gamma$ and small angle Bhabha scattering are $\geq 99.9\%$.

Information concerning the pretrigger and trigger decision, the inputs to the $\theta - \phi$ matrix, subdetector readout time, and bunch identification, is made available offline in pretrigger and trigger definition files. Since pretrigger and trigger conditions may vary between OPAL runs, the definition files are necessary to decode trigger information offline.

2.3.2 Online Data Flow

When a beam crossing is selected by the central trigger logic to contain a potentially interesting event, the General Trigger Unit (GTU) signals each of the individual subdetectors to be read out. Each of the sixteen subdetectors is read out separately by its own special front-end readout electronics into local system

crate(s) (LSC). For each subdetector the LSCs perform data reduction, formatting, and data preparation for the software filter. The subevent structures from the 16 subdetector and 2 pretrigger and trigger LSCs are assembled by the event builder (EVB) into a single data structure.

Upon assembly by the EVB, the completed events are passed in sequence to the filter processor. Once in the filter, the events are monitored and undergo a fast analysis before being compressed and written to disk. At this stage events are classified into various physics categories and events flagged as background can be rejected or passed on at a reduced level. Poorly measured events account for typically 15-35 % of all triggers and are rejected.

The headers of all events reaching the filter, whether rejected or not, are recorded on disk to help in book-keeping. The events passing the filter are written to disk files in 20 Mbyte long partitions. These complete events, along with subdetector calibration information, is copied from the filter disk to a farm of workstations performing online event reconstruction.

Online Event Reconstruction

A collection of Unix workstations located on the surface at the OPAL interaction point execute the online event reconstruction software, commonly known as ROPE. ROPE processes the raw data known as digits from the various subdetectors and writes the event information in the data summary tape (DST) format.

Digits consist of data in the form of output from TDCs, ADCs and other similar units. With an appropriate set of calibration constants, drift chamber hit coordinates or calorimeter energy can be reconstructed. Each subdetector has a set of routines that take the raw data and processes it into quantities that can be

used in physics studies. Information about track parameters, the event primary vertex and secondary vertices, dE/dx, time of flight, calorimeter energies and muon hit positions are stored into the DST format. ROPE also provides a set of routines that allows this DST information to be accessed for subsequent offline analysis.

The various subdetector calibration constants are usually available within an hour of the events being recorded. Once the events have been passed through the online reconstruction they are written to an output buffer disk. Events which meet the physics selection criteria are stripped off and transferred over the network to the OPAL offline analysis facility at the main CERN site. The partitions from each data-taking run, which usually correspond to one fill of LEP, are sorted, moved onto permanent disk storage, and backed up on cartridge. The events recorded by OPAL is typically available for offline analysis within a few hours of the end of a run.

2.3.3 The OPAL Detector Simulation Software

In order to gain an understanding of the acceptances and efficiencies of the OPAL detector, the GOPAL [16] Monte Carlo simulation program has been developed, and is based upon the CERN GEANT [17] detector description and simulation package.

In order to simulate the response of the OPAL detector to a given physics event, the physics event itself must be first simulated through the use of an event generator program. The event generator program calculates the cross section for the requested physics process, and generates the initial particle configuration and kinematics at the interaction point. This information can then be passed into the

GOPAL simulation program to determine the response of the OPAL detector to this type of event.

The GOPAL program defines the OPAL detector in terms of a set of predefined GEANT shapes, providing information on the location, layout, and material composition of each subdetector. Tracking of particles through the various subdetector volumes is performed by GEANT. During each tracking step the probability of an interaction occuring is calculated, along with the processes of multiple Coulomb scattering and energy loss. When a track passes through a sensitive volume (such as a drift cell in the vertex chamber), a 'hit' is registered, and the corresponding particle position and momentum are stored. GEANT also simulates secondary physics processes such as hadronic interactions in the detector material, photon pair production, and particle decays.

Once all particles have been tracked through the detector, the hit information is collected for each subdetector and the detector response is simulated, including detector resolution effects and inefficiencies. This stage is known as digitization, and produces a data structure identical to raw OPAL data. The digitized information is then processed by the ROPE event reconstruction code and written out in the standard DST format for later analysis.

CHAPTER 3

The Tile Endcap (TE) Detector

In May of 1996, the Tile Endcap (TE) detector was installed in both endcaps of OPAL.

This installation enhances the trigger capabilities in the endcap region by providing valuable trigger redundancy required to maintain efficient triggering in the presence of higher beam backgrounds expected at LEP2. The TE detector also provides: the ability to tag bunchlets during bunch train running; a more effective cosmic ray veto; and, a veto for Standard Model backgrounds to the search for new physics at LEP2.

In the following sections the motivation for the installation of a fast scintillation detector in the OPAL endcaps is presented in the context of the conditions expected at LEP2 and under bunch train operations. The design of the TE detector which provides a robust and versatile trigger will subsequently be covered, detailing both the mechanical and optical layout of the detector.

3.1 Motivation

The trigger system of the OPAL detector is designed to provide high efficiency for various physics reactions, and has been shown to provide good rejection of a variety of backgrounds by imposing several independent conditions on the subdetector

signals. It is recognized though that the capabilities of the OPAL trigger diminish when considering the backgrounds expected while running at LEP2, particularly in the endcap region of the detector.

3.1.1 Pre-TE Trigger Conditions

Prior to 1996 [18], pretrigger and trigger signals in the forward region $0.8 \leq |\cos\theta| \leq 0.95$ were provided by the jet (CJ) and vertex (CV) tracking chambers, along with the endcap muon chambers (ME) and the electromagnetic (EE) calorimeter. These are all separate signals at the pretrigger level. Triggering on CJ and CV, along with ME, are efficient for minimum ionizing particles. At the track level, CJ and CV are put into coincidence in order to reduce the already high trigger rate in the forward region experienced in CJ alone. Persistent noise problems though in EE have increased the trigger thresholds to approximately 700 MeV, well above minimum ionizing. Furthermore, the track trigger efficiency in the region of $|\cos\theta| > 0.88$ decreases, and declines to zero for $|\cos\theta| \geq 0.95$.

Various backgrounds, such as synchrotron radiation and beam-gas interactions, encountered at LEP affect the performance of the OPAL trigger. Synchrotron radiation increases the pretrigger rate, and may limit the gain at which the CV can be operated if the background is sufficiently severe. The beam gas interactions can cause spurious track triggers by producing curling tracks at low radius in both the CV and CJ. These backgrounds exist at LEP1, and are expected to increase at the higher energies of LEP2, particularly due to the higher beam currents required to maintain a high luminosity.

The possibility of upgrading the existing endcap presamplers (PE) to provide the required triggering capabilities had been examined [19]. As PE consists of

only a single layer of chambers any trigger which depends upon PE would be very sensitive to noise. An increase in synchrotron radiation background is expected at LEP2, and as such the number of noise hits in the PE chambers would also be expected to increase. Therefore, the PE chambers would not be able to provide an efficient standalone trigger signal which would be sensitive to minimum ionizing particles. The TE detector, situated between the EE and PE, will be able to provide good time resolution and a very high efficiency for minimum ionizing particles. By placing TE in coincidence with existing triggers, a redundant trigger system will be created without the cost of raising trigger thresholds in an environment of increased backgrounds.

3.1.2 Bunch Trains

Since August of 1989, LEP has been operating under a variety of injection and particle acceleration schemes. Running began initially with 4 bunches of electrons and 4 bunches of positrons countercirculating around the LEP ring (4+4 operation), and has continued with 8+8 operations in the socalled Pretzel scheme, which describes the particle orbits as they circulate around the LEP complex. This mode is limited at injection to bunch currents of approximately 350 μA, the maximum attainable for operations with a beam energy of 45 GeV. The Pretzel scheme has a maximum injection current of less than 1 mA.

At LEP2, the electron and positron beam energies have been doubled to approximately 92 GeV. The current goal of running at LEP2 is for each experiment to achieve 500 pb^{-1} integrated luminosity within a three year period. This would require from LEP a peak luminosity of approximately $7\times10^{31}cm^{-2}s^{-1}$ operating in 8+8 bunch mode, compared to $1.5\times10^{31}cm^{-2}s^{-1}$ achieved during 1993

under LEP1 conditions. At present, injection currents of approximately 1 mA are available, but exceed the capabilities of the Pretzel scheme. For the Pretzel Scheme to remain in use, the bunch currents would have to be increased by a factor of 8 in order to maintain a constant value of the beam-beam tune shift (ξ_x and ξ_y) at LEP2 energies. Experimentally, the observed lower bunch currents of 350 μA have been found to arise from horizontal beam-beam interactions in mid-arc where the momentum dispersion of the beams is a maximum.

A solution to overcome the limitations of running in Pretzel mode which has been developed is known as the Bunch Train scheme [20, 21], and has been operational at both LEP1 and LEP2. In the initial 4 bunch design, the beams are separated in the vertical plane at the location of the 8 interaction points. For physics runs, the orbit separations in the four experimental interaction points are switched off to achieve colliding beams. In Pretzel mode, the 8 additional beam-beam encounters in mid-arc are avoided by causing horizontal separations in the arcs.

In bunch train mode, the extra beam-beam interactions would occur in the straight sections both upstream and downstream of the interaction point, as well as the interaction point itself. Therefore it is necessary to separate the bunches at the extra beam-beam interaction points, and rather than separate the bunches horizontally as in the Pretzel scheme, the bunches are separated in the vertical plane. Here the momentum dispersion is theoretically zero, and in practice is much smaller than the horizontal dispersion at mid-arc. The vertical separations are achieved by placing electrostatic separators both upstream and downstream of the interaction points. The maximum length of the train, and therefore the maximum number of bunches in a train, is determined by the maximum separation-bump length.

The LEP experiments have imposed an upper limit of 750 ns on the total length of a bunch train. From the resulting minimum distance from the interaction points to the first separator, the minimum inter-bunch spacing is approximately 74.2 m or 247.5 ns, limiting the number of bunches in a train to four at LEP1. Therefore operating with bunch trains at LEP1 consists of 4 trains with 4 bunches per train, and a bunch current of 0.5 mA. With these operating characteristics, a luminosity of $6.3 \times 10^{31} \mathrm{cm}^{-2}\mathrm{s}^{-1}$ is expected for physics runs at energies near the Z^0 mass.

At LEP2, the parameters of bunch train operation differ from those of LEP1. There are still 4 trains per beam, but the beam current maximum of 8 mA is achieved with 2 bunches per train providing the maximum luminosity with the minimum number of bunches, and a bunch spacing of approximately 148 m or 495.0 ns, twice that for bunch trains at LEP1. Operating in this mode at LEP2 energies of approximately 90 GeV per beam, a luminosity in excess of $8 \times 10^{31} \mathrm{cm}^{-2}\mathrm{s}^{-1}$ is expected to be achievable.

With both LEP1 and LEP2 running in bunch train mode, the maximum length of a bunch train will be approximately 750 ns, with the number of bunches per train depending upon the beam energy. For both cases OPAL treats a bunch train as a single bunch collision, but with a large timing uncertainty [18, 22]. This in particular affects the EE performance.

Typical signals in EE last on the order of 1.5 μs, while the total ADC gate is only 1 μs, and has already been optimized to yield good energy resolution performance. Running with bunch trains will require the timing gates to be expanded by 750 ns in order to cover signals at all possible collision times within a train. This will have two effects. First, a widening of the integration gate time

results in increased noise; secondly, the proportion of EE signal which falls within the ADC gate depends upon the timing and thus is different for each bunch, with the amount of signal from the first and last bunch lower than for the middle two bunches. Estimates of the reduction in signal for the outer two bunches indicated that a variation of 14.5 % in signal is expected. In order to limit the smearing of the energy resolution to the approximately 1 % level, the signal reduction is needed to be known with an accuracy of 7 %.

As mentioned in Section 3.1, an upgrade of PE to provide trigger and online bunch collision information during bunch train operation is very difficult. By providing a fast time of flight system in the endcap region, namely TE, it will be possible to accurately determine online the bunch collision time, and pass this information onto the other subdetectors. Corrections could then be made online to the measured EE energy for a given bunch crossing, and would be particularly useful in the case of an all neutral event in the endcap region. Without TE, offline determination of the bunch crossing time from track fitting would be necessary, resulting in a significant increase in the offline data handling.

The installation of a fast endcap trigger detector has several direct applications to ongoing physics analyses. By combining the bunch crossing time with information provided by other subdetectors, TE is able to assist in the reduction of several background processes [7].

3.2 The TE Mechanical and Optical Design

Prior to installation, various designs were considered for the TE detector. Through the use of computer simulations and prototype development, the existing TE

design [7] was achieved. In this section, the various spatial and performance constraints encountered will be reviewed, along with a discussion of the final TE detector design, covering both the mechanical layout and optical characteristics of the detector. The specific optical properties of the various materials utilized in TE will also be given, as they are important parameters to the detector simulation software.

3.2.1 Design Constraints and Considerations

The principle constraints on the design of TE were: the limited space available in the endcap region; the magnetic field of the OPAL detector; the need to maximize the endcap coverage; the limited space available for signal cable readout; and the need for adequate light output. Placed directly between the electromagnetic endcap calorimeter and the endcap presampler TE had to be accommodated within approximately 2.5 cm of space. The space constraints eliminated the possibility of local use of phototubes and lightguides and led to the use of 10 mm thick scintillator tiles read out using wavelength shifting (WLS) fibre for TE. The fibres were embedded in grooves machined in the scintillator tiles. To transport the light out of the endcap region, clear optical fibres were coupled to the WLS fibres via precision optical connectors. The transported light then could be detected by shielded photomultiplier tubes situated outside of the endcap region.

3.2.2 Tile and Electronics Readout

As shown in Figure 3.1, the TE detector is placed directly between the presampler and electromagnetic calorimeter in both endcaps of OPAL. In each endcap TE

occupies 15 mm of space longitudinally and provides coverage in the angular region $0.78 < |\cos\theta| < 0.96$ through 48 physical divisions in ϕ and 3 physical divisions in θ. Figure 3.1 also demonstrates the layout for a 1/24 sector of the detector.

At least two separate mechanical elements per sector were needed in order to match the truncated cone shape of the endcap lead glass blocks. The two outermost physical divisions in θ were grouped together into 24 sectors in each endcap in order to match the existing ϕ segmentation of the OPAL trigger, as well as to economize on the number of photomultiplier channels necessary to read out TE. The inner 24 sectors are single piece scintillator tiles and are not restricted beneath the endcap presampler. Each of these tiles is read out by a separate photomultiplier, and can later be disconnected from the OPAL trigger in the presence of high background rates which may arise from their proximity to the beamline.

Tile and Optical Design

The TE tiles were manufactured of Bicron BC408 [23] scintillator, and were machined with a 2 mm deep sinusoidal-like groove path on both top and bottom faces to accommodate the WLS fibre. The groove pattern chosen allows for the collection of light at both ends of each fibre, and maximizes the length of fibre embedded within the scintillator. The final layout design of the WLS fibres was chosen, on the basis of simulation and prototype testing, to maximize the light yield per fibre while recognizing the space constraints which limit the total number of fibres which can exit the pole tip region. This is important since light is lost in the conversion of blue scintillator light to green as well as in the optical

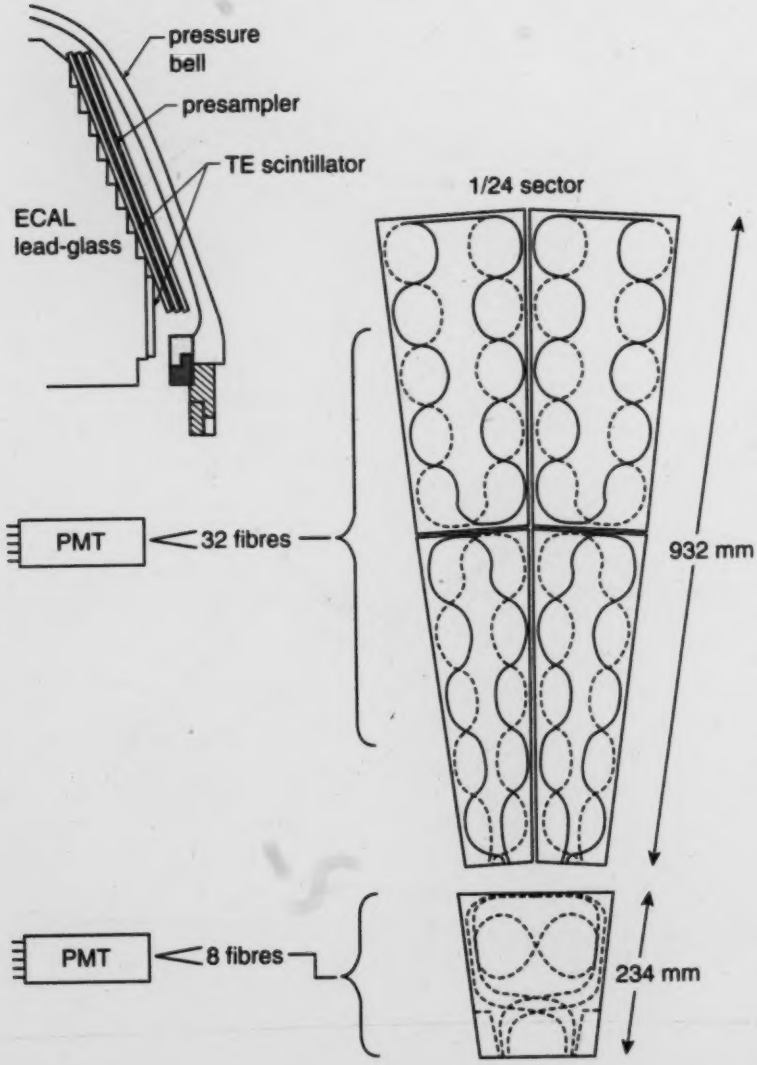

Figure 3.1: Layout of a 1/24 sector of the TE detector.

connectors and clear optical fibre. By using WLS fibres the distribution of scintillation photon emission directions is traded for a new distribution in which the WLS photons are emitted isotropically and thus have a greater opportunity to be collected as part of the readout of the scintillating tile.

To provide a high surface reflectivity and light tightness around the scintillator, each sector was wrapped with 150 μm Tyvek and 50 μm Tedlar respectively. Endbars bolted to a backplate at the inner and outer radii secured the wrapping and sectors, and allow the WLS fibres to exit the scintillator. The endbars also provided a locating hole for a light emitting diode which could be used to help calibrate and monitor the performance of each TE sector.

Two 1 mm diameter Kuraray Y11-200-non−S multiclad WLS fibres [24] were embedded in each of the grooved trenches, and coupled via precision optical connectors to 13 m long 1 mm diameter clear Hoechst Infolite ER51 optical fibre [25]. Figure 3.2 schematically shows the connector used to couple the WLS and clear optical fibres. This connector was designed and built by staff at the Centre for Subatomic Research at the University of Alberta using Delrin [26] plastic. The connectors provide stable alignment of the fibres to an accuracy of 10 μm. By polishing to a fibre surface flatness of a few microns the connector further provide a high degree of light transmission from the WLS to clear optical fibre. The WLS fibre holes of the connector vary in diameter in order to prevent damage during disconnection if necessary.

A description of the optical properties of the various components used in the construction of TE is provided in section 3.3 as they are necessary inputs to the detector simulations discussed in Chapters 7 and 8. Details of the production and assembly process of each TE segment can be found elsewhere [7].

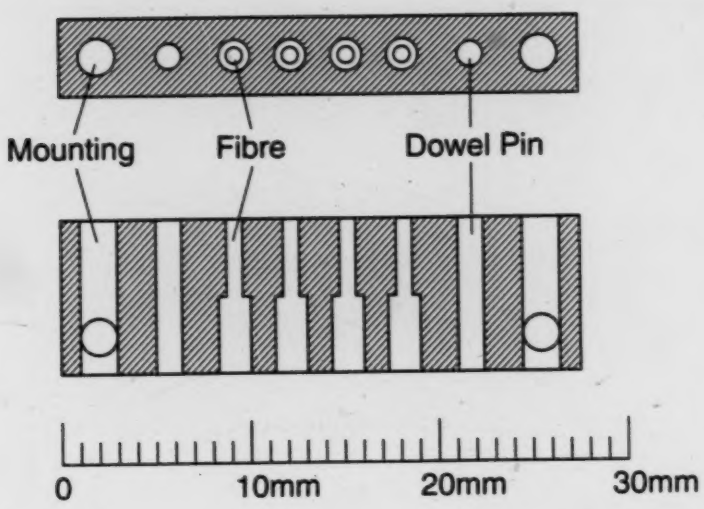

Figure 3.2: Coupler to connect the WLS and clear optical fibres.

The 1 mm diameter clear optical fib-ER carries the light from the WLS fib-ER outside of each endcap region to an array of Electron Tubes Ltd. 9902SKA photomultiplier tubes [27]. The choice of photomultiplier tube was made based upon its quantum efficiency for 500 nm wavelength light, gain, cost, size, and uniformity of response over most of the photocathode [28]. A study of the photomultiplier tube response indicated that the electron optics of the tube results in a systematically lower response in one quadrant. To ensure contact with the three quadrants of the tube that have uniform response, a special optical coupler, shown in Figure 3.3, was designed to support the fibres.

The photomultipliers are mounted in four boxes containing 12 tubes each, and are placed on the pole hooks which support the pole tips of the OPAL detector. Mu-metal and electrostatic shielding are required as the magnetic field is still substantial, nearly 30 to 50 Gauss in this region.

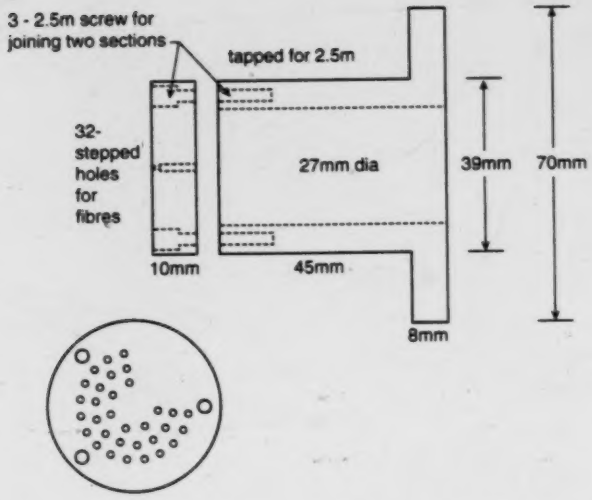

Figure 3.3: Coupling device to connect the clear optical fib-ER to the photomultiplier tubes.

Electronics

As with all other subdetectors in OPAL, the TE detector electronics must interface the photomultiplier tube signals with the OPAL trigger matrix, and as well must provide stand-alone signals to assist in monitoring the performance of the detector. The front end readout electronics used to achieve this is schematically shown in Figure 3.4.

The signal from each photomultiplier tubes is passed through a splitter into two signals. The first signal is sent to 16 bit CERN CIA ADCs, while the other signal is passed to Analog Devices AD96685BQ 1 ns comparators which can discriminate the signal with remote threshold control. The discriminated signals are then passed to 1 ns/count 16 bit Lecroy 2277/3377 TDCs, as well as to a matching module which prepares the signals for input to the OPAL trigger

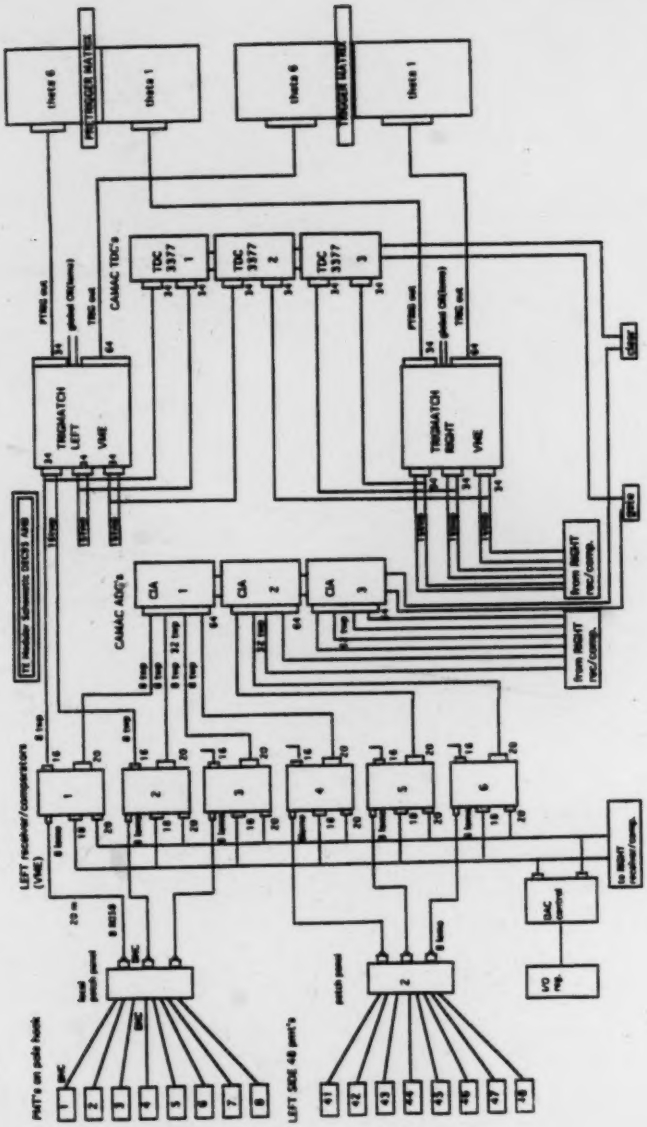

Figure 3.4: Front end electronics which interface the TE signals to the existing OPAL Pretrigger and Trigger Matrix.

BC-408 Plastic Scintillator	
Light Output (% Anthracene)	64
Wavelength of Maximum Emission $\lambda_{max}(nm)$	425
Decay Constant (main component) $\tau_{decay}(ns)$	2.1
Bulk Attenuation Length $L_{att}(cm)$	380
Refractive Index n	1.58
H/C Ratio	1.104
Density $\eta(g/cm^3)$	1.032
Softening Point ($\deg C$)	70

Table 3.1: Physical constants of BC-408 plastic scintillator.

matrix (discussed in Section 2.3.1).

3.3 Scintillator and Fibre Properties

The characteristics of the materials used to construct the TE detector, particularly the optical properties of the plastic scintillator and the wavelength shifting and optical fibres, are important inputs to the simulations of the TE prototype and final designs.

3.3.1 Plastic Scintillator BC408

Each sector of the TE detector is constructed from Bicron BC408 plastic scintillator [23, 29]. BC408 is a general purpose scintillator particularly suited to time of flight and large area detectors. It is manufactured from a Polyvinyltoluene base, and has a higher light yield compared to most plastic scintillators, approximately 64 % that of Anthracene. Table 3.1 summarizes the physical properties of BC408 scintillator.

The emission spectra of BC408, demonstrating the relative light output as a function of wavelength, is shown in Figure 3.5, indicating a primary emission wavelength of 425 nm in the blue region of the optical spectra. From tests carried out during TE development, BC408 scintillator has been shown to provide the necessary light yield and durability to act as a fast trigger in the OPAL endcap.

3.3.2 Kuraray Y11 Wavelength Shifting Fibre

Embedded within the scintillator tiles are looms of Kuraray Y11-non S WLS fibre. The Kuraray fibre is a double clad fibre consisting of a core material of refractive index 1.60 surrounded by two thin layers of material with differing refractive indices of 1.49 and 1.42 respectively. The core material absorbs an incoming photon and then re-emits a photon of different wavelength. The two cladding layers act to trap the emitted photon via total internal reflection, which can then propagate down the length of the fibre. Compared to single clad fibres, the Kuraray multiclad fibre provides a greater optical acceptance of photons, and therefore allows the propagation of more photons to the end of the fibre. By utilizing a WLS fibre, the primary scintillator photon emission distribution is essentially exchanged for the distribution of reemitted photons within the fibre, thereby allowing improved light collection.

To transport the light which reaches the WLS fibre end to the photomultiplier tubes situated outside the endcap region, Hoechst Infolite ER51 clear fibre [25] was chosen for its low attenuation of 120 dB/km at 500 nm. This 1.0 mm diameter clear fibre is a single clad fibre of $n_{core} = 1.49$ and $n_{clad} = 1.42$. A thin light-tight polyethylene outer jacket increased the overall fibre diameter to 1.5 mm.

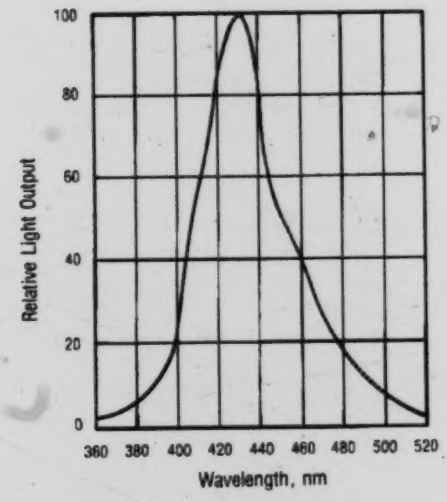

Figure 3.5: Emission spectra of BC-408 scintillator.

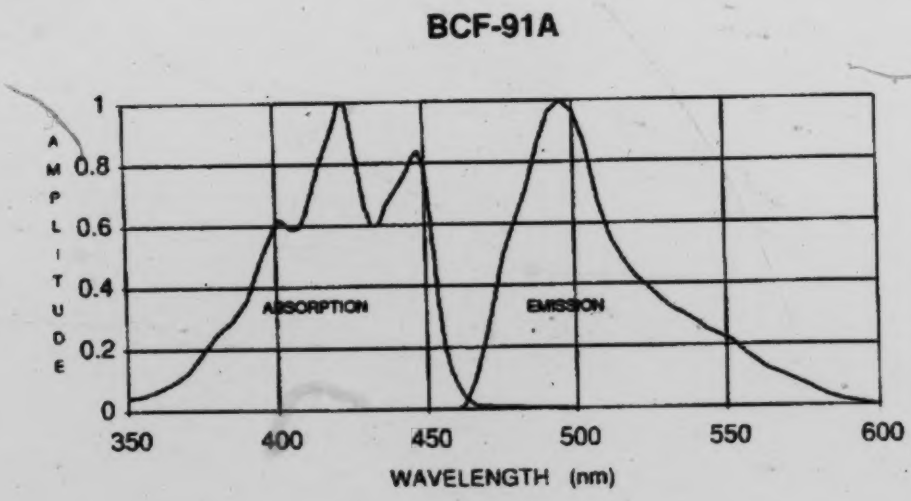

Figure 3.6: Absorption and emission spectra of BCF-91A WLS fibre.

BCF-91A Wavelength Shifting Fibre	
Peak Emission Wavelength $\lambda_{max}(nm)$	494
Decay Constant $\tau_{decay}(ns)$	12.0
Attenuation Length $L_{att}(cm)$	> 350
H/C Ratio	0.994
Core Density $\eta(g/cm^3)$	1.05

Table 3.2: Physical constants of $BCF\text{-}91A$ wavelength shifting fibre.

3.3.3 Bicron BCF-91A Wavelength Shifting Fibre

Most of the TE prototype development utilized the singleclad WLS fibre BCF-91A [29]. BCF-91A is constructed from a polystyrene based core with a single acrylic PMMA (polymethylmethacrylate) cladding layer. The core and cladding layers have refractive indices of 1.60 and 1.49 respectively, with the cladding thickness being typically 3% of the fibre diameter. Various properties of BCF-91A are listed in Table 3.2.

The BCF-91A WLS fibre has a primary absorption wavelength in the blue region of the optical spectra, clearly overlapping with the maximum emission wavelength of the BC408 scintillator, and reemits photons at a peak emission wavelength of 494 nm in the green. The sensitivity of the Electron Tubes Ltd. photomultiplier tube is well matched to this wavelength of light. The relative absorption and emission amplitudes for BCF-91A are shown in Figure 3.6.

The relative absorption amplitude of the BCF-91A fibre depends upon the fluor concentration, and therefore the wavelength of the incoming photon. The point inside the WLS fibre where the primary photon is absorbed depends upon the photon mean free path inside the fibre core material. The value of the mean free path is also wavelength dependent, and is shown in Figure 3.7.

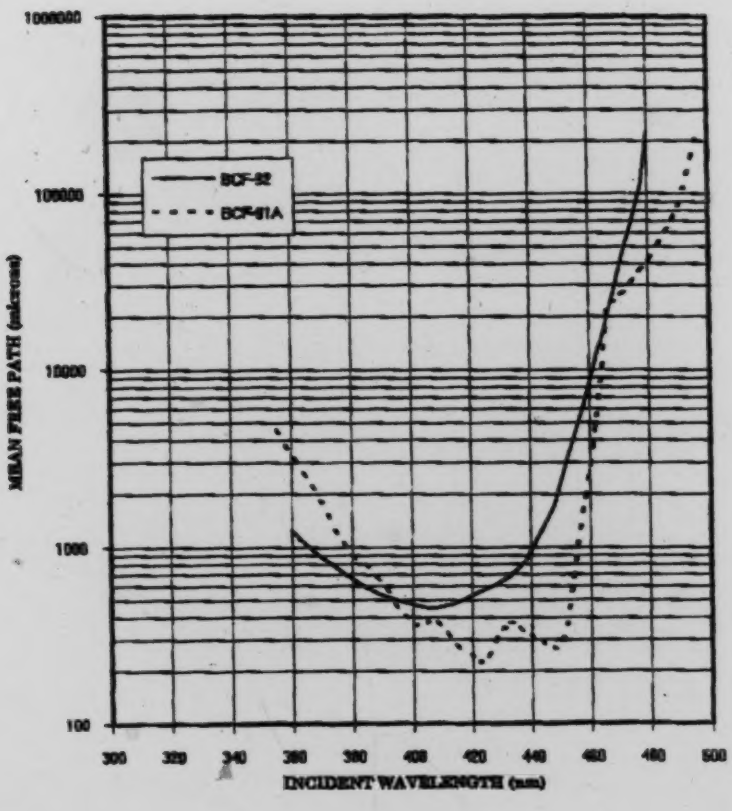

Figure 3.7: Values of the Mean Free Path of incident light in BCF-91A WLS fibre as a function of incident photon wavelength.

Of the scintillation light emitted by BC408, photons with a wavelength between about 400 and 450 nm have the greatest likelihood of undergoing absorption in the WLS fibre core of BCF-91A, with mean free path values in the range of about 0.2 to 0.4 mm. Therefore one would expect that photons near the peak emission wavelength would be predominantly absorbed near the outer edges of the WLS fibre core for a 1 mm diameter fibre, away from the fibre axis. A small amount of photons outside the primary emission range will be absorbed closer towards the center of the fibre. For instance, primary photons with a wavelength of about 460 nm are emitted at 40 % of the peak wavelength rate, but have a mean free path of about 2 mm. Therefore the probability for absorption is reduced, and should be uniformly distributed within the fibre cross-section.

CHAPTER 4

Scintillator and Optical Fibre Physics

One of the most often and widely used particle detection devices in particle physics today is the scintillation detector. Certain materials when struck by a charged particle or ultraviolet (UV) radiation will emit a small flash of light, otherwise known as a scintillation. Information concerning the incident radiation can be determined by coupling the scintillator material to an amplifying device such as a photomultiplier, such that the scintillations can be converted into electrical pulses which can be counted electronically. Scintillator detectors through their main properties of sensitivity to energy, fast time response, and pulse shape discrimination, can provide a wealth of information about the incident radiation. Scintillator materials in use today include organic crystals and liquids, plastics, inorganic crystals, gases, and glasses. The most common and versatile scintillator material are the organic plastics, as used in the TE detector.

In the design of the TE detector given in Chapter 3, wavelength shifting (WLS) fibres are used to carry the light of each scintillating tile detector segment out of the OPAL endcap region. Such fibres are dielectric materials and, for the purpose of calculating the propagation of photons, can be described by geometric optics.

In the following sections an overview of the scintillation process will be given with emphasis on the mechanism for light generation in plastic organic scintillators, the most widely used type of scintillator material. The efficiency

of plastic scintillators will also be covered, along with its dependence upon the performance capabilities of the photomultiplier tube. A discussion of the optical properties of dielectric optical fibres will be provided to demonstrate the transition from an electromagnetic to geometric description of photon propagation inside optical fibres.

4.1 The Scintillation Process

Scintillator materials exhibit the property known as *luminescence*. Luminescent materials, when exposed to certain forms of energy such as radiation, absorb and reemit the energy in the form of visible light. The time evolution of the reemission process is described as a simple exponential decay such that the number of photons N emitted at time t is given by

$$N = \frac{N_0}{\tau_d} \exp \frac{-t}{\tau_d} \tag{4.1}$$

where N_0 is the total number of emitted photons, and τ_d is the decay constant. Due to the complex composition of most scintillators, the reemission process for such materials can be described by the sum of several exponential decay terms. Most scintillators typically have one component which decays faster than the others, and as such the reemission process can be described as

$$N = A \exp \frac{-t}{\tau_f} + B \exp \frac{-t}{\tau_s} \tag{4.2}$$

where τ_f and τ_s are decay constants of the fast and slow components of the reemission respectively. The relative magnitudes A and B vary between materials. The presence of fast and slow decay constants accounts for the successful technique of pulse shape discrimination capable with some scintillator materials.

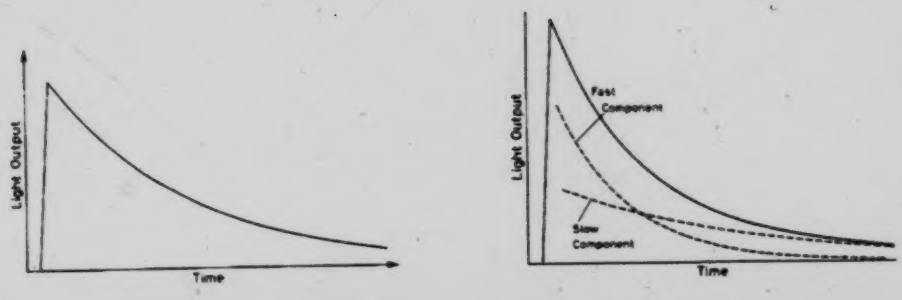

Figure 4.1: Shown above are the simple single (left) and more accurate two-component (right) exponential decay descriptions of scintillator light reemission. The solid line represents the total emitted light decay curve including both fast and slow components.

Figure 4.1 demonstrates both the simple single exponential and more accurate two-component exponential decays. The finite rise time from zero to maximum is usually shorter than the decay time in most materials, and can be ignored for simplicity.

If the reemission process occurs within typically 10^{-8}s the process is considered 'fluorescence'. A more precise definition of fluorescence will be provided below when discussing plastic organic scintillators, but its use here should be sufficiently clear in terms of the reemission time.

4.1.1 Organic Scintillators

Organic scintillators [30, 31] are manufactured from aromatic hydrocarbon compounds containing linked or condensed benzene-ring structures, and are distinguished by their very fast decay times, typically a few nanoseconds or less.

The scintillation light arises from transitions made by the free valence

electrons in the scintillator molecules. These electrons occupy the π molecular orbitals [32], are delocalized and are not associated with any particular atom in the molecule. Figure 4.2 shows schematically an energy level diagram for these orbital states. The ground singlet state as well as the first and second excited singlet states are labelled as S_0, S^*, and S^* respectively. The same labelled scheme also applies to the triplet ground and excited states. A fine structure is associated with each energy level due to the excited vibrational modes of the molecule. Between the electron levels, the energy spacing is typically a few eV, whereas the vibrational level separation is on the order of a few tenths of eV.

The ionization energy from penetrating radiation excites both the electron and vibrational levels, as shown by the solid arrows. The singlet excitations generally decay in less than 10 ps to the S^* state without the emission of radiation. This process is known as internal degradation. From the S^* state there is a high probability of a radiative transition within a few nanoseconds to one of the vibrational states of the ground state S_0, shown by the wavy lines. This process is known as fluorescence, and is described by the fast exponential decay component of the reemission process described in 4.2.

A similar degradation process occurs with the excited triplet states, bringing the system to the lowest triplet state T_0. Transitions from T_0 to S_0 are highly forbidden by the multipole selection rules, and as such decays instead occur primarily through the interaction with another excited T_0 molecule through the reaction

$$T_0 + T_0 \rightarrow S^* + S_0 + \text{phonons} \tag{4.3}$$

The S^* state then decays via fluorescence as mentioned above. The light emitted via this process is delayed by a time characteristic of the interaction

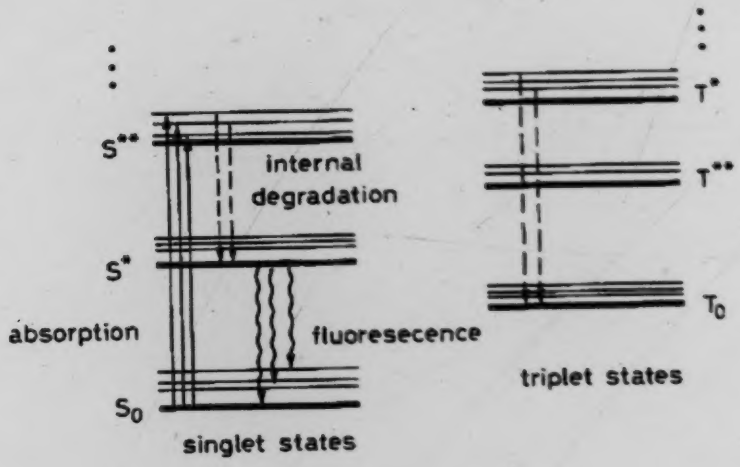

Figure 4.2: Shown are the singlet (S) and triplet state (T) energy levels of an organic scintillator molecule.

between the excited molecule, and corresponds to the slow component of the emitted scintillator light in 4.2.

Due to the molecular nature of luminescence in these materials, organics can be used in either crystalline, liquid, or plastic form, and still preserve their scintillation properties. Plastic scintillators are quite flexible and can be easily machined and shaped into desired forms, and are therefore the predominant type of organic scintillator used in high energy physics experiments.

Organic Plastic Scintillators

Plastics scintillators are solutions of organic scintillator used in conjunction with a solid plastic solvent, the most common examples being polyvinyltoluene, polyphenylbenzene and polystyrene. The plastic solvent base is the ionization-sensitive portion of the plastic scintillator, and is described by the molecular deexcitation mechanism given above.

Upon deexcitation, the base emits ultraviolet (UV) photons with short attenuation lengths on the order of millimeters and would be absorbed shortly after being emitted if not for the presence of primary fluor solutes. Fluors exhibit the property correctly termed as fluorescence, in which the initial molecular excitation occurs via the absorption of a photon and de-excites through the emission of a photon of longer wavelength. Primary fluor solutes such as PBD, p-Terphenyl, and PBO are dissolved in concentrations on the order of 1 % by weight, and efficiently reradiate absorbed energy at wavelengths where the base is more transparent.

The suitability of a fluor is characterized by what is known as the Stokes Shift [31]. The Stokes Shift is the difference between the major absorption and emission peak wavelengths of the fluor, and defines the extent of self-absorption of the fluor. Large values of the Stokes Shift are usually desired for use in plastic scintillators so as to reduce the amount of self-absorption.

At the above mentioned concentrations, the average distance between a fluor molecule and an excited base unit is about 1×10^{-8}m, far less than a wavelength of light. At such small distances, the dominant mode of energy transfer from base to primary fluor is via a resonant dipole-dipole interaction described by Foerster [33]. The use of a primary fluor as a result can decrease the decay time and improve the light yield of the scintillator.

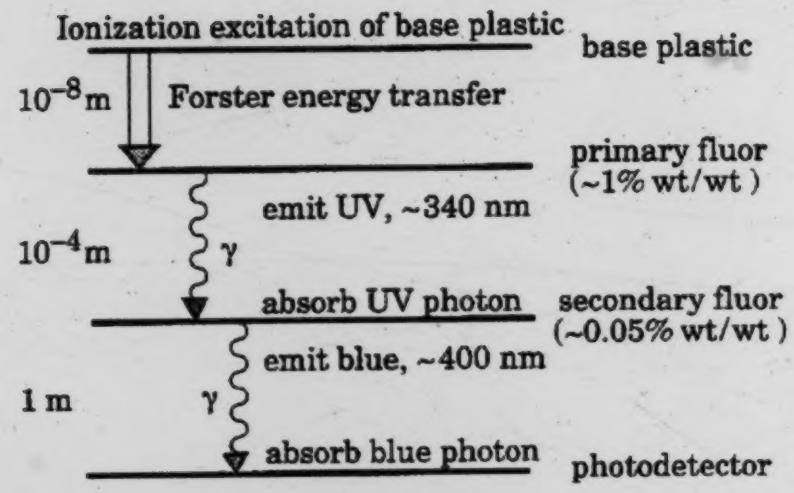

Figure 4.3: Scintillation mechanism for a typical plastic scintillator, including the Foerster energy transfer, as well as the primary and secondary fluor behavior. The approximate fluor concentrations and energy transfer distances are also shown.

As shown in Figure 4.3, the light emitted by the primary fluor is still in the UV spectrum, and therefore in many plastic scintillators a secondary fluor must be added to shift the wavelength of the photon to a longer value, extending the attenuation length in the plastic base. Secondary fluors are are dissolved in concentrations of typically 0.05 % by weight.

Plastic scintillators are characterized by a fast decay time and high light output. The finite rise time that was ignored in the light output description of equation 4.2 cannot be neglected for plastics, and as such the best description has been shown [34] to be given by the convolution of exponential and Gaussian distributions,

$$N(t) = N_0 f(\sigma, t) \exp \frac{-t}{\tau} \tag{4.4}$$

Scintillator	σ(ns)	τ(ns)
NE102A	0.7	2.4
NE111	0.2	1.7
Naton 136	0.5	1.87

Table 4.1: Gaussian and exponential parameters for several plastic scintillators describing the light pulse distribution.

where $f(\sigma, t)$ is a Gaussian with standard deviation σ, and τ is the decay constant. The values of σ and τ for various common plastic scintillators are given in Table 4.1.

The plastic scintillator BC408 utilized in the TE detector has a composition and light yield very similar to both PILOT F and NE102A [35], and is also well described by equation 4.4.

Scintillator Efficiency

An important property of a scintillator is its light output or efficiency for converting ionization energy to photons, as it determines the scintillator's efficiency and resolution. In general, the light output for different types of particles at the same energy is different, and even for a given particle type the light yield doesn't always vary linearly with particle energy.

To characterize a scintillator material, it is convenient to define an average energy loss required for the creation of a photon. For plastic scintillators this value is on the order of 100 eV/photon for electrons, with efficiency decreasing for heavier particles in general. In contrast, other scintillators such as Anthracene, NaI, and BGO require average energy losses of 60, 25, and 300 eV respectively per scintillation photon generated.

Scintillation detector efficiency not only depends upon the photon generation efficiency of the scintillator material, but also the quantum efficiency of the photomultiplier tube. The quantum efficiency refers to the probability of photoelectron emission for a photon of a given wavelength incident upon the photocathode. Due to the wavelength dependency, a proper selection of scintillator material and photomultiplier must be made to ensure the spectral emission range is consistent with the spectral response of the photomultiplier, and to maximize the quantum efficiency. Typical values of quantum efficiency for most photomultipliers are on the order of 20% to 30%. Other criteria for choosing a photomultiplier include the tube gain, noise, crosstalk, timing, and spatial and anode-to-anode uniformity.

4.2 Optical Fibres

A discussion of the optical properties of dielectric optical fibres will be provided to demonstrate the transition from an electromagnetic to geometric description of photon propagation inside optical fibres. For multimode optical fibres such as BCF-91A a purely geometrical optics approach is sufficient to accurately describe photon propagation and allows for the simulation of scintillating tile-WLS fibre detectors.

4.2.1 Leaky Ray Theory of Optical Waveguides

Cylindrical optical waveguides can be examined via electromagnetic theory to describe the propagation of waves along the fibre. This exact description [36] involves the decomposition of the electromagnetic fields into the bound (discrete)

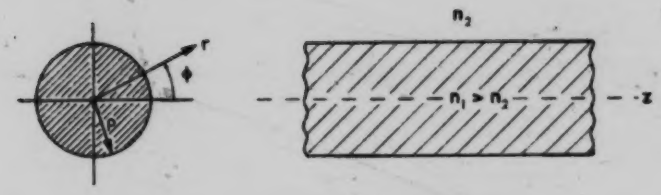

Figure 4.4: Optical fibre of circular cross section with radius ρ and refractive index n_1, surrounded by an unbound medium of refractive index n_2.

and unbound (continuous) mode spectrum.

Consider an infinite cylinder of radius ρ and index of refraction n_1 surrounded by an unbounded medium of refractive index n_2, as shown in Figure 4.4.

Derivation of the optical fibre electromagnetic fields can be made from the scalar functions $\hat{\psi}$ that satisfy the reduced wave equation

$$(\nabla^2 + k_1^2)\hat{\psi} = 0 \quad , r < \rho \tag{4.5}$$

$$(\nabla^2 + k_2^2)\hat{\psi} = 0 \quad , r > \rho \tag{4.6}$$

where r is the polar radius,

$$k_1 = \omega\sqrt{\mu\epsilon_1} = 2\pi n_1/\lambda \quad ,$$

$$k_2 = \omega\sqrt{\mu\epsilon_2} = 2\pi n_2/\lambda \quad , \tag{4.7}$$

ϵ_1 and ϵ_2 are the dielectric constants of the waveguide and its surrounding medium respectively, μ is the permeability of the medium, and λ is the wavelength in vacuum. Due to the symmetry about the fibre axial or z direction, the fields can be written in the form

$$\hat{\psi}(r, \phi, z) = \psi(r, \phi)e^{i\beta z} \tag{4.8}$$

where β is the component of the wave vector. As a result equations 4.5 and 4.6 become

$$(\rho^2\nabla_t + U^2)\psi = 0 \quad , r < \rho \tag{4.9}$$

$$(\rho^2\nabla_t + Q^2)\psi = 0 \quad , r > \rho \tag{4.10}$$

where

$$U^2 = (\rho k_1)^2 - (\rho\beta)^2 \tag{4.11}$$

$$Q^2 = (\rho k_2)^2 - (\rho\beta)^2 \tag{4.12}$$

Here ∇_t is the transverse or z independent part of the gradient ∇, and U and Q are the transverse components of the dimensionless wave vector inside and outside the waveguide, respectively.

It is convenient to define a dimensionless frequency V to describe the propagation of waves inside the optical fibre. V is defined as

$$\begin{aligned} V^2 = \; & U^2 - Q^2 = (\rho k_1^2)^2 - (\rho k_2)^2 \\ = \; & (\rho k_1 \sin\theta_c)^2 \end{aligned} \tag{4.13}$$

and

$$\sin\theta_c = (1 - (n_2/n_1)^2)^{1/2} \tag{4.14}$$

where θ_c is the complement of the critical angle.

As mentioned above, the electromagnetic fields can be decomposed into bound and unbound modes. Bound modes are derived from the real β_{lm} solutions of 4.9 and 4.10. In order to describe the radiation from waveguides the unbound modes must be examined, but this analysis is considered to be extremely complicated and difficult to express in a usable form. Therefore an approximation to

the radiation field can be made by considering what are known as leaky modes, which are found from certain complex β_{lm} solutions to 4.9 and 4.10.

By taking the small wavelength limit the fields of a mode can be shown to be formed by a family of rays where each ray of the family is incident on the boundaries at the same angle to the normal. Bound modes are formed by a family of rays that undergo total internal reflection, while leaky modes are formed by a family of rays that only partially reflect from the cylinder walls.

The solutions [36] to the eigenvalue equations 4.9 and 4.10 are given by

$$\psi = J_l(Ur/\rho)e^{-i(l\phi)} \quad , r < \rho \tag{4.15}$$

$$\psi = H_l(Qr/\rho)e^{-i(l\phi)} \quad , r > \rho \tag{4.16}$$

where ψ is the z component of either the electric or magnetic field, H_l is the Hankel function of the second kind, and J_l is a Bessel function. Bound mode solutions can be shown [36] to obey the condition

$$0 \leq U_{lm} < V \quad , 0 < |Q_{lm}| \leq V \tag{4.17}$$

with fields that exponentially decay far from the fibre, and as such Q_{lm} is pure imaginary and U_{lm} and V are pure real. In general each mode of circular optical waveguide will fail to satisfy the radiation condition for V below a certain $V = V_{lm}^{co}$, known as the cutoff for mode lm where $J_{lm}(V_{lm}^{co}) = 0$. For $V < V_{lm}^{co}$ there are solutions to the eigenvalue equation yielding complex β_{lm}'s, which correspond to fields that attenuate in the direction of propagation. We define a position

$$r_{tp}^{lm} = \rho(l-1)/Q_{lm} \tag{4.18}$$

which is called the *turning point* or caustic, and is the origin of the radiation.

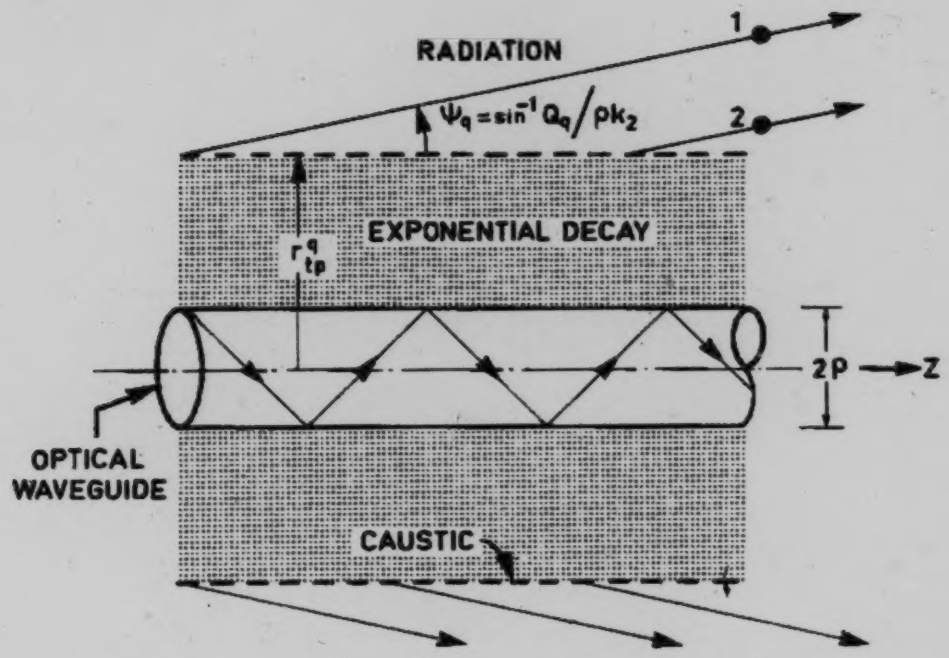

Figure 4.5: Fields of the leaky q'th mode on an optical waveguide of circular cross section. Shown is the radiation caustic or turning point r^q_{tp}.

Figure 4.5 schematically shows the fields of the leaky q'th mode and the caustic r^q_{tp}.

Bound modes are defined by $r^{lm}_{tp} = 0$. As $r^{lm}_{tp} \to \rho$ the modes rapidly become leaky. The leaky modes can be subdivided into the two categories of refracting ($r^{lm}_{tp} = \rho$) and tunneling ($\rho < r^{lm}_{tp} < \infty$). The refracting leaky modes attenuate because their fields are made up of waves that undergo refraction at the core-cladding boundary, while tunneling leaky modes attenuate because their fields are made up of waves that undergo partial reflection at the core-cladding boundary due only to the curvature of the cross-section. This curvature loss is

due to a form of electromagnetic tunneling. The waves in general tunnel from the core-cladding boundary through the evanescent region as shown in Figure 4.5 to emerge at the caustic as radiation. If the core-cladding interface were not curved, then the waves would undergo total internal reflection. Tunneling modes generally leak very slowly compared to refracting modes, and their leakage vanishes as the wavelength approaches zero.

Modified Geometric Optics

Instead of using electromagnetic theory, it is possible to apply modified geometrical optics to the study of multimode optical waveguides and fibres, which are characterized by a value of the dimensionless frequency $V \gg 1$. Using the definition of V given in equation 4.13, and substituting in the values of the fibre radius ρ, core refractive index n_1 and peak photon wavelength λ, the Bicron BCF-91A WLS fibre can be shown to fit this classification with $V \simeq 3550$, and as such this analysis is directly applicable to the fibres used for TE development.

As mentioned in the previous section, the fields of a mode are formed by a family of rays each incident on the boundaries at the same angle to the normal. If θ_c is the complement of the critical angle and θ_z is the angle of the ray with respect to the fibre axis, then only rays with $\theta_z \leq \theta_c$ are trapped by total internal reflection. This is in comparison to the incorrect prediction by Fresnel's laws that all rays incident at angles greater than the critical angle are trapped. Defining the complement of the angle of incidence θ_n as

$$\theta_t = \pi/2 - \theta_n \tag{4.19}$$

then Fresnel's laws require $\theta_t < \theta_c$ for a ray to be trapped. When a ray is

incident at an angle $\theta_t > \theta_c$ Fresnel's laws state that it is partially reflected while undergoing refraction, and the amount of light lost to radiation can be found by summing the loss at each reflection. Expressing this loss in terms of an attenuation coefficient, the power $P(z)$ of a ray after traveling a distance z is given by

$$P(z) = P(0)e^{-\alpha z/\rho} \tag{4.20}$$

where ρ is the fibre core radius and

$$\alpha = 2(\frac{\sin^2\theta_z}{\theta_c \cos\theta_z})[(\frac{\theta_t}{\theta_c})^2 - 1]^{1/2} \tag{4.21}$$

This expression is valid only for weakly attenuating rays with $\theta_t > \theta_c$, and fails for cases when θ_t is too close to θ_c.

In the ray treatment of waveguides there are also rays that fall into the category of tunneling rays which satisfy the requirement

$$\theta_t < \theta_c \quad , \theta_z > \theta_c \tag{4.22}$$

While all rays with $\theta_t < \theta_c$ are predicted by Fresnel's laws to be trapped, in fact the decomposition of the tunneling leaky modes into rays shows that rays with $\theta_z > \theta_c$ will undergo partial reflection. Due to the boundary curvature the rays are undergoing a form of electromagnetic tunneling and are not refracting. The attenuation is entirely due to the curvature of the cross-section only. The partial reflection is not accounted for by Fresnel's laws. It is also possible to write a dimensionless attenuation coefficient for tunneling rays for the case when $\theta_t < \theta_c$, and is given by

$$\alpha = 2(\frac{\sin^2\theta_z}{\theta_c \cos\theta_z})[1 - (\frac{\theta_t}{\theta_c})^2]^{1/2} \exp\left(2l \cosh^{-1}(l/Q) - 2(l^2 - Q^2)^{1/2}\right) \tag{4.23}$$

where

$$l = k\rho(\sin^2\theta_z - \theta_t^2)^{1/2} \tag{4.24}$$

$$Q = k\rho(\sin^2\theta_z - \theta_c^2)^{1/2} \tag{4.25}$$

For $\theta_t \simeq \theta_c$, 4.23 simplifies to

$$\alpha = 2(\frac{\sin^2\theta_z}{\theta_c\cos\theta_z})[1 - (\frac{\theta_t}{\theta_c})^2]^{1/2}\exp\left(-2/3[\frac{k\rho(\theta_c^2 - \theta_t^2)^{3/2}}{\sin^2\theta_z - \theta_c^2}]\right) \tag{4.26}$$

This expression is applicable for most tunneling rays of interest.

A significant portion of the radiation field can persist for enormous distances within the circular optical waveguide for $V \gg 1$, so that both the guided and radiation field are required to represent the power flow even at great distances from the source. In comparison, for a slab waveguide, the radiation field spreads from within the slab waveguide in a very short distance from the source, essentially a few waveguide diameters, so the power transmitted from within the slab is represented entirely by the guided portion of the fields. The difference arises from the existence of rays skew to the axis in the circular waveguides.

From the electromagnetic analysis, rays with $\theta_z \leq \theta_c$ are trapped by total internal reflection. All other rays with $\theta_z > \theta_c$ undergo partial reflection and eventually their energy within the waveguide is depleted, and it is these rays that make up the radiation field. For the circular waveguide most of the rays are skew to the fibre axis, and only rays with $\theta_t > \theta_c$ undergo refraction and attenuate rapidly. But the radiation field is also composed of tunneling rays with $\theta_t < \theta_c$, $\theta_z > \theta_c$, erroneously predicted by Fresnel to be trapped by total internal reflection, which only partially reflect and eventually leak from the waveguide. Also, many tunneling rays have such small attenuation that they can be considered trapped

even over distances kilometers in length. Due to the complicated nature of the electromagnetic theory treatment of optical waveguides, the modified geometric optics approach is the most suitable.

Although we have discussed the ray approach to multimode optical waveguides, it is also necessary to consider the waveguides under illumination from a source. The discussion most suited to describe the illumination of WLS fibre such as BCF-91A is associated with incoherent illumination from what is known as a diffuse or Lambertian source. A diffuse or Lambertian source is one where each differential area dA of the source emits light in all directions yielding a power distribution given by

$$dP = I(\theta_0)d\Gamma dA \quad ,0 \leq \theta_0 \leq \pi/2 \tag{4.27}$$

with an intensity distribution of

$$I(\theta_0) = I_0 \cos\theta_0 \tag{4.28}$$

where θ_0 is the angle relative to the normal. The Lambertian source is the most typical used in practice and approximates the output of a light emitting diode (LED). An LED can also have a nonuniform intensity distribution with the light output decreasing towards the boundaries of the source and I_0 depending upon the cylindrical radius r from the source. Such a distribution can be described by a Gaussian

$$I_0(r) = A \exp -\alpha r^2/\rho_s^2 \tag{4.29}$$

where ρ_s is the source radius, and A and α are positive constants.

For a multimode fibre, it is possible to use ray tracing and the attenuation coefficient given in 4.23 for tunneling rays to determine the amount of light at any

distance z along the fibre. It can be shown [36] that the sum of all tunneling rays gives the power P^R of the radiation field within the fibre, and is given by

$$\frac{P^R}{P^{inc}} = T \int_{\theta_c}^{\pi/2} d\theta \sin\theta \cos\theta \int_{\sqrt{1-p^2}}^{1} \sqrt{1-x^2}(1 - \exp(\alpha(x)z/\rho))dx \qquad (4.30)$$

The results of a classical geometric optics approach can be achieved by setting $\alpha = 0$ or $z = 0$. Figure 4.6 demonstrates numerical results for fraction of incident power within the fibre when illuminated by an incoherent source for various values of V as a function of z/ρ, where z is the distance along the waveguide and ρ is the fibre radius. Since BCF-91A wavelength shifting fibre has a dimensionless frequency $V \simeq 3550$, it is clear that even over large distances such as $1.4m$ the fraction of incident power remaining within the fibre is very high and greater than 95%. Therefore classical geometric optics is a very suitable approach to consider when treating ray propagation down wavelength shifting fibres. This shall be the focus of the next section.

4.2.2 Geometrical Optics

Geometrical ray optics can readily describe the propagation of light through optical fibres. Between reflections the ray follows a straight line and, on reflection from the interface, its direction is determined by Snell's laws [37]. Thus the incident ray, reflected ray and normal, or radial direction, lie in the same plane, and the angles of incidence and reflection relative to the normal are equal.

Meridional and Skew Rays

Rays can be separated into two possible categories. Rays which cross the fibre axis between reflections are *meridional rays*, while rays which never cross the fibre axis

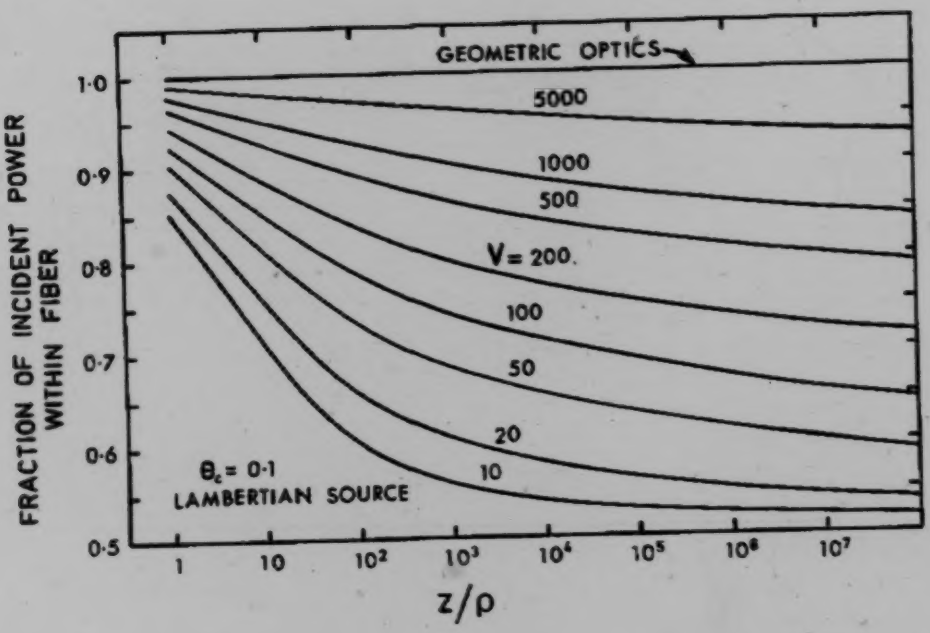

Figure 4.6: Shown above is the fraction of incident power within the fibre as a function of z/ρ for illumination from an incoherent source. The values shown are for various V. The fraction of power remaining within the fibre is greater than 0.95 for BCF-91A ($V \simeq 3550$) over distances of 1.4 m.

are called *skew rays*. Figure 4.7 demonstrates the two ray types. The meridional rays lie in a plane of width 2ρ, where ρ is the fibre core diameter, through the axis. The trajectory of a meridional ray can be specified with the angle θ_z between the path and the z-direction which is defined as the fibre axis. The ranges of θ_z are determined by the refractive indices of the core and cladding materials and total internal reflection.

Meanwhile skew rays follow a helical path, whose projection onto the cross-section is a regular polygon. The trajectory can be further described such that the

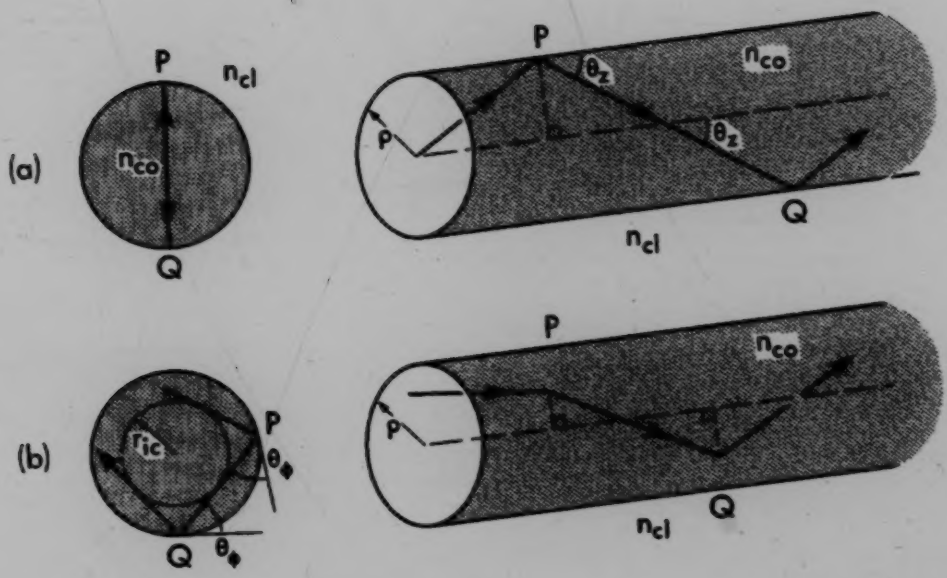

Figure 4.7: Shown above are the ray paths for photons emitted within the core of a step-index fibre, which can be classified into a) meridional rays and b) skew rays. The projection of the ray path onto the core cross-section is also shown.

midpoints between successive reflections all touch a cylindrical surface of radius r_{ic}, known as the *inner caustic*. The specification of a skew ray trajectory not only requires knowledge of θ_z, but also the value of a second angle θ_ϕ which represents the angle in the core cross-section between the tangent to the interface and the projection of the ray path. The angles θ_z and θ_ϕ are shown in Figure 4.7.

The angles θ_z and θ_ϕ are spherical polar angles relative to the axial direction PQ as shown in Figure 4.8. Also shown is α, the angle between the incident and reflected rays and the normal. From projections, the three direction angles are related such that

$$\cos\alpha = \sin\theta_z \sin\theta_\phi \tag{4.31}$$

The radius of the inner caustic only depends upon the skewness angle, and is given by

$$r_{ic} = \rho \cos \theta_\phi \tag{4.32}$$

For meridional rays $\theta_\phi = \pi/2$, and as such $r_{ic} = 0$.

A ray is predicted by Snell's laws to refract at P if $\alpha < \alpha_c$, where α_c is the critical angle defined by

$$\sin \alpha_c = \frac{n_{clad}}{n_{core}} = \cos \theta_c \tag{4.33}$$

The ray will undergo total internal reflection if $\alpha > \alpha_c$. Therefore one is led to believe that all rays with $\alpha > \alpha_c$ are bound. As discussed in Section 4.2.1 this is not a completely valid statement, as only certain rays satisfying this condition are bound. From the ray-path equation [38] the condition for a ray to be bound has been shown to be

$$0 \leq \theta_z < \theta_c \tag{4.34}$$

This arises since Snell's laws have been derived for reflection from planar surfaces, whereas the fibre interface is curved. The condition in 4.34 for a ray to be bound yields a cone of angles at each position in the fibre core cross-section that can describe both meridional and skew rays. Skew rays which do not satisfy the condition set out in equation 4.34 are labelled as tunneling rays. Therefore rays propagating down step-clad fibres, such as WLS and scintillating fibres, can be classified into three possible categories.

$$\text{BoundRays}: \quad 0 \leq \theta_z < \theta_c \tag{4.35}$$

$$\text{RefractingRays}: \quad 0 \leq \alpha < \alpha_c \tag{4.36}$$

$$\text{TunnelingRays}: \quad \theta_c \leq \theta_z \leq \pi/2$$

$$\alpha_c \leq \alpha \leq \pi/2 \tag{4.37}$$

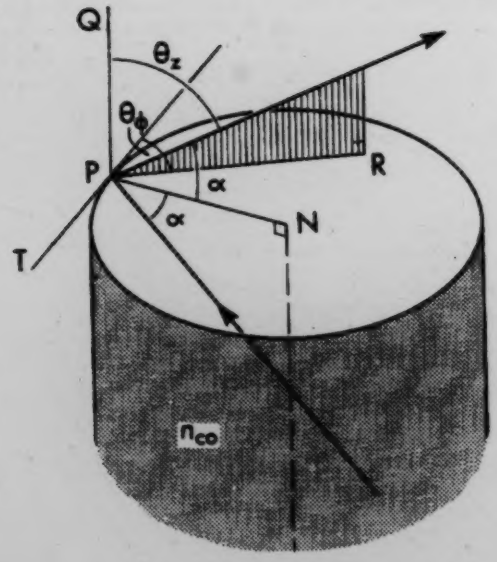

Figure 4.8: Shown above are the angles describing the reflection of a ray incident on an interface of a step-profile fibre. The angle of incidence or reflection, α, is with respect to the normal PN. Both incident and reflected rays make angles θ_z with the axial direction PQ, and θ_ϕ in the cross-section between the tangent PT and the path projection.

As will be discussed in the Chapter 5, all simulations of the TE detector prototypes have utilized the geometric optics approach in which Snell's law for reflection for planar surfaces is being applied to reflections at curved surface interfaces. While the conditions used are as previously stated not completely correct, the use of the multimode optical fibre BCF-91A with V$\simeq$3550 clearly indicates the suitability of the geometrical optics approach.

Ray Invariants

The trajectory of any particular ray path is described by the constant angles θ_z and θ_ϕ. Using these angles it is possible to define two ray invariants, $\overline{\beta}$ and $\overline{l}$, in terms of θ_z and θ_ϕ such that

$$\overline{\beta} = n_{core} \cos\theta_z \tag{4.38}$$

$$\overline{l} = n_{core} \sin\theta_z \cos\theta_\phi \tag{4.39}$$

$$\overline{\beta}^2 + \overline{l}^2 = n_{core}^2 \sin\alpha^2 \tag{4.40}$$

where n_{core} is the refractive index of the fibre core material. The value of $\overline{\beta}$ accounts for the translational invariance of the fibre along its axis, and $\overline{l}$ accounts for the azimuthal symmetry of the fibre. For meridional and skew rays, $\overline{l} = 0$ and $\overline{l} > 0$ respectively. Using these invariants, equations 4.37 can be rewritten in the form

$$\text{BoundRays}: \quad n_{clad} < \overline{\beta} \leq n_{core} \tag{4.41}$$

$$\text{RefractingRays}: \quad 0 \leq \overline{\beta}^2 + \overline{l}^2 < n_{clad}^2 \tag{4.42}$$

$$\text{TunnelingRays}: \quad n_{clad}^2 < \overline{\beta}^2 + \overline{l}^2 \leq n_{core}^2$$

$$0 \leq \overline{\beta} < n_{clad} \tag{4.43}$$

Therefore for a bound ray with given $\overline{\beta}$, the value of $\overline{l}$ is restricted to within the range $0 \leq \overline{l} \leq n_{core}^2 - \overline{\beta}^2$. The range of possible values describing a bound ray, as well as those for refracting and tunneling rays, in the $\overline{\beta}-\overline{l}$ plane is schematically shown in Figure 4.9.

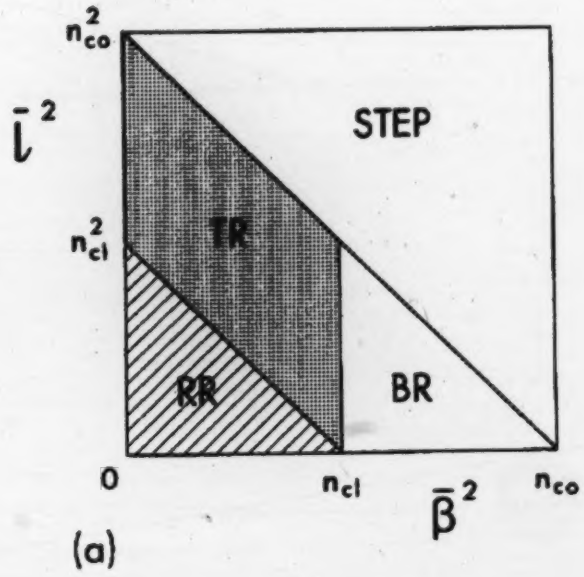

Figure 4.9: Shown above is the schematic distribution of bound (BR), refracting (RR), and tunneling (TR) rays in the $\overline{\beta} - \overline{l}$ plane for a step-profile fibre.

Trapping Efficiency

One important property to be considered when studying WLS fibres is the trapping efficiency, the amount of isotropically emitted light which is trapped in the forward region due to total internal reflection. The trapping efficiency of the WLS fibre is dependent upon the location of the secondary photon emission relative to the fibre axis, as well as the direction of emission.

An alternative to expression 4.37 which defines the conditions for a bound ray, describing a photon emitted inside the core of an optical fibre, but determined using geometric optics, can be shown [39] to be given by the equation

$$\sin\theta\sqrt{1-\frac{1}{r^2}(p_x\sin\phi - p_y\cos\phi)^2} \leq \sin\theta_{tr} \tag{4.44}$$

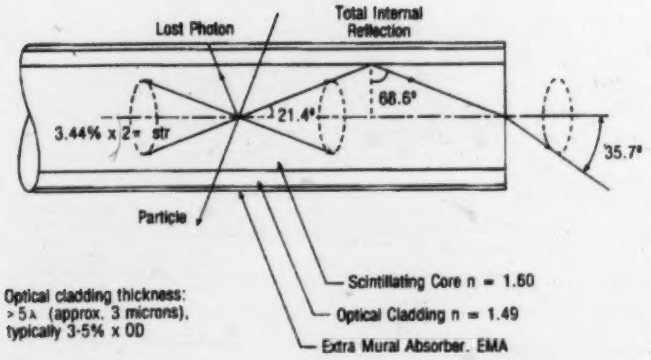

Figure 4.10: Shown is the geometrical acceptance of emitted photons inside the core of the WLS fibre.

where r is the radius of the fibre core, (p_x, p_y) is the photon generation point, (θ, ϕ) is the direction of the photon emission in polar coordinates, and θ_{tr} is the trapping angle defined by the refractive indices of the core and cladding materials $(\cos\theta_{tr} = n_{cladding}/n_{core})$.

For photons emitted along the fibre axis (meridional rays), the trapping efficiency only depends upon the refractive indices of the core and cladding materials [39], and 4.44 simplifies to

$$TE = \frac{1}{2}(1 - \frac{n_{cladding}}{n_{core}}) \tag{4.45}$$

This is on the order of 3.4 % for BCF-91A, such that the photons are trapped within a cone, as shown in Figure 4.10. When considering light emitted from positions successively further off axis, the polar angle of the trapped photons depends upon the azimuthal orientation of the emitted light. For photons emitted in the plane defined by the emission point and the fibre axis (meridional rays), the trapping still occurs within the cone angle.

Due to the higher polar angle acceptance for emission points off axis, a larger proportion of photons which reach the end of the WLS fibre are expected to be skew rays. For BCF-91A the trapping efficiency for such off axis photons is typically 7 %. This expected behavior has been verified by various simulations [40] of both scintillating and WLS fibres, and will be demonstrated in later sections of this analysis.

CHAPTER 5

Simulation Tools

High energy physics experiments are continually increasing in complexity. The processes of detector design and optimization, the development and testing of reconstruction and analysis programs, and the interpretation of experimental data each require simulation studies of the detector geometry and layout. GEANT is a system of detector description and simulation tools to assist in such studies. In this chapter an overview of the GEANT detector description and simulation package will be given. A second package, GUIDEIT, will also be discussed in the context of the limitations of GEANT. Together these two software packages provide a platform for the complete simulation of the prototype and final design TE scintillating tiles. The capability of GUIDEIT to supplement the simulation results provided by GEANT will be demonstrated through a comparison of simulation and data taken for a single optical fibre.

5.1 Simulation Packages

5.1.1 GEANT Version 3.21

At the most basic level, GEANT Version 3.21 [17] simulates the passage of elementary particles through matter. The geometrical layout and composition of the detector is defined by the user through a set of routines, and describes the

experimental setup as a structure of geometrical volumes. Each volume can be provided with a specification of tracking medium parameters and material type which GEANT 3.21 uses to transport, or track, particles through an experimental setup in order to provide a simulation of detector response. The tracking of particles through the setup is affected by volume boundaries and particle interactions with matter, as well as any specific processes associated with the particle, and also by the magnetic field if present. The particle trajectories and response of declared sensitive detector components are recorded for subsequent analysis.

For reference purposes, version 3.21 of GEANT will be commonly referred to as GEANT throughout the remainder of this thesis.

In addition to detector geometry, GEANT can accept input from various Monte Carlo event generators. To aid in the debugging and development of detector design, an interactive interface is provided to yield graphical representations of detector setup, as well as particle trajectories.

The execution of GEANT to simulate a high energy physics experiment is a three step process including initialization, event processing, and program termination.

The initialization process in GEANT fills various data structures necessary to describe material and particle properties, as well as determines the energy loss and cross-section tables for various materials. The user specifies the detector geometry and tracking parameters associated with the various media. Furthermore, the user specifies which elements of the detector to be considered as sensitive elements in which detector response is to be simulated.

The GEANT program then performs the simulation of the desired number of events, where for each event the same series of routines to process and track the

event through the detector elements are executed. The kinematics of the event are either read from an external Monte Carlo generator or generated by GEANT, and are stored in various event data structures. The event kinematics are described in terms of vertices, each of which describes to GEANT the particle types and trajectories. Each particle is propagated through the detector setup and tracked. Upon traversing a detector element which has been declared as a sensitive volume, the user can store useful information such as position, momentum, and energy loss. This information can then be used to simulated detector response such as pulse heights. Together these two sets of information are known as hits and digits. All the various electromagnetic and hadronic interactions are simulated within GEANT. During each tracking step the user is given control to take appropriate actions such as storing hits, writing out data structures, and specifying which generated secondary particles are to be tracked. Control of the event processing and tracking is then returned to GEANT.

Upon completion of all event processing, the various data structures which were written out are closed, and GEANT is terminated.

5.1.2 GUIDEIT

GUIDEIT (Version 1.1) [41] is a simple and efficient software package designed to model scintillator and light guide systems. Comprised of a set of Fortran routines, GUIDEIT provides a straightforward method to describe various geometries and optical characteristics, and traces the propagation of optical rays through this geometry. In GUIDEIT all photons travel in straight lines between surfaces, and all scattering effects are neglected. The ray tracing is performed by determining the intersection point of a ray with a surface and deciding upon the appropriate

action to be taken, whether it be refraction, reflection, or absorption, and then continuing to trace the ray propagation through the geometry. All reflections of rays at surfaces are specular following the assumption that all surfaces are smooth. Diffuse reflection has not yet been implemented in GUIDEIT.

Surfaces can be declared by the user to possess various properties which determine the behavior of a photon which is incident upon that surface. Surfaces can be declared as bare, having a metal wrapping such as aluminum foil, or perfectly reflecting. The surfaces that are available in GUIDEIT are PLANEs, CIRCULARs (discs), CYLINDERs, BENTs (cylinder sections), CONEs (truncated cones), and CONSECs (conic sections of rotation). Most shapes can be described by combinations of surfaces that compose the faces of the required shape. For example, a cube would be described by six planes, and a circular rod would be described by a cylinder and a disc on each end.

The overall scintillator-light guide system can be a composite of several independent shapes known as sequences. While tracing the photon through the setup, only intersection points of the photon ray with the surfaces belonging to the current sequence are computed, thereby reducing the number of surface searches required to be performed at each step of the simulation.

5.2 The GEANT Description of Scintillation Detectors

With the latest version of GEANT, (Version 3.21), no routines exist to simulate the scintillation process. In order to simulate the scintillation mechanism the existing structure of GEANT has been adapted to perform scintillation at the

user level utilizing the pre-existing Cerenkov photon routines. This procedure, as implemented to perform the work described in this thesis, is based greatly upon the design and testing procedures associated with the TE prototype scintillating tiles, but is easily extendable to general detector geometries and arrangements.

Scintillation is the emission of optical photons generated from the ionization energy loss of charged particles passing through a material, and has been discussed earlier in this thesis. The energy loss is in general distributed uniformly along the particle trajectory through the scintillator with the generated photons emitted at positions along or very near (on the order of 10^{-8} m) to the generated ionization column.

Upon passing through the scintillator material, the charged particle ionization energy losses are typically on the order of 2 MeV $\cdot$ cm^{-1} traversed for a minimum ionizing particle [31]. For an approximately 1 cm thickness of plastic scintillator this corresponds to $\approx$ 20 000 photons emitted within the scintillator, or 10 000 photons/MeV. This is a very large number of photons to track through the geometrical setup, and as such is a prohibitively excessive number of particles to track requiring an immense amount of computing time to simulate. As an alternative the number of photons generated for each MeV of energy deposited in the scintillator is restricted to approximately 500, with a maximum number of 5000 primary photons in the GEANT tracking stack, thereby reducing the required computing time. Subsequent analysis of the simulation results can then be scaled to reflect the correct light yield for the amount of energy deposited for any given event.

Furthermore, to account for a wide variety of conditions experienced during the prototype testing (such as scintillator surface polish quality and wrapping

material reflectivities) all values of surface reflectivity and material attenuation length used within GEANT during photon tracking were set to unity and infinity respectively. Subsequent analysis of the Monte Carlo results then yield the total distance travelled and the number of reflections which occured. Various values of attenuation length and surface reflectivity can then be applied, allowing for a determination of the optimal parameters which bring the Monte Carlo into agreement with the experimental results.

The user scintillation routines generate the appropriate uniform distribution along the particle trajectory through the scintillator and pass to GEANT the emission position of the primary photons which are considered secondary particles within the GEANT framework. The particle which passes through the scintillator and generates photons through ionization energy loss is labelled the primary particle.

Each of the photons is given a random direction of emission to provide a uniformly distributed number of photons per unit solid angle. The user routines also calculate the photon wavelength which corresponds to the scintillator material to be simulated. Simulation of the decay time of the scintillator is also performed in the user scintillation routines. A random polarization is also given to the emitted photon.

The generated secondary particle, treated by GEANT as a Cerenkov photon, is placed in what is known as the GEANT tracking stack. The photon is then tracked by GEANT through the scintillator until it is either absorbed or exceeds the maximum number of allowable tracking steps, typically 10 000. At such point of absorption or interaction all information concerning the photon hit position, current volume, time of flight, pathlength, momentum, and number of reflections

at all interfaces are recorded.

Since the TE prototype scintillating tiles also contained wavelength shifting fibres, the secondary process of wavelength shifting has also been simulated at the user level in GEANT in a fashion similar to the primary scintillator photon generation. Upon termination of a primary photon tracking, it is determined whether the current hit position and volume correspond to a section of the wavelength shifting (WLS) fibre. If the absorption or interaction occurred within the fibre core, then a second wavelength shifted Cerenkov photon is placed within the GEANT tracking stack. Again the photon is emitted isotropically, is placed in the GEANT tracking stack, and propagated through the detector geometry. The wavelength of the emitted photon is again determined randomly based upon a user specified distribution which describes the emission spectra of the fibre.

Trapping of the secondary photons inside the fibre occurs due to total internal reflection, and is determined only by the relative refractive indices of the fibre core, cladding layer, and surrounding scintillator materials. As such, the majority of the secondary photons will escape the fibre and enter the scintillator. These photons will in reality propagate through the scintillator until they are attenuated, and will not undergo absorption in the fibre core or reach the end of the fibre where a photomultiplier has been affixed. Simulation of such escaping secondary photons is therefore restricted in order to reduce the amount of computing time spent on tracking photons which will never reach the end of the WLS fibre. Once a secondary photon is generated inside the fibre, it will only be tracked until it escapes from the fibre into the scintillator material. Upon escaping that particular photon is removed from the GEANT tracking stack, and tracking continues with the next photon in the queue.

Upon either absorption or termination of the secondary wavelength shifted photon, the data structures associated with the secondary photon are read out and include measures of the photon hit position, current volume, wavelength, momentum, pathlength, time of flight, and number of reflections experienced while propagating down the WLS fibre.

At the end of the simulation, we therefore have the information about the incident particle which traverses the scintillator, as well as both the primary and secondary photons. The photon wavelength, emission position, final hit position, momentum, pathlength, time of flight, and number of reflections all act as input to the simulation analysis code which applies realistic values for the various surface reflectivities and material attenuation lengths. A direct comparison between the simulation and the observed measurements is then possible.

5.3 GEANT-GUIDEIT Combination

The GEANT software is limited in its capability to act as a complete and robust ray tracing utility. As discussed previously in Chapter 4, each photon ray trajectory which propagates down an optical fibre maintains several constant ray path parameters such as the angle of incidence with respect to the surface normal, and the distance to the inner caustic from the center of the fibre.

5.3.1 GEANT Failure During Ray Tracing

Two constant ray path parameters have been found not to remain constant during the secondary photon tracking procedure for GEANT. The tracking of the primary scintillating photons does not suffer from difficulties as the photons are tracked

only through planar surfaces as opposed to surfaces with curved boundaries.

Figure 5.1 provides an example of the extent to which GEANT fails to track the secondary photons correctly through the fibre geometry. A Monte Carlo simulation was performed of a single photon emitted at one end of a 500 cm long multiclad optical fibre of 0.0415 cm radius. The photon was emitted from a point near the fibre core-cladding interface with an emission angle of $(\theta, \phi) = (11.9°, 65.7°)$, where θ is the angle of emission with respect to the fibre axis, and ϕ is the angle of emission with respect to the x-axis in the fibre cross-section. These angular variables were chosen to have the photon trapped inside the fibre core due to total internal reflection and not enter either of the cladding layers. Therefore this photon can be described as a skew ray.

The photon emitted in this direction will intersect the fibre surface at a 78.8° angle of incidence, and should remain constant throughout the entire tracking procedure. In GEANT the value of the angle of incidence and the angle with respect to the fibre axis θ vary, and as a result alter the value of the track inner caustic radius r_{ic}. The value of the inner caustic radius decreases dramatically indicating that the photon path has transformed from a skew to meridonal ray, and has become more aligned towards the fibre axis. Therefore the GEANT tracking has indeed violated the requirement that the ray path parameters remain constant, and will yield incorrect results, particularly when considering the photon location as a function of time in the fibre cross-section. The source of the GEANT tracking failure is unknown at this time.

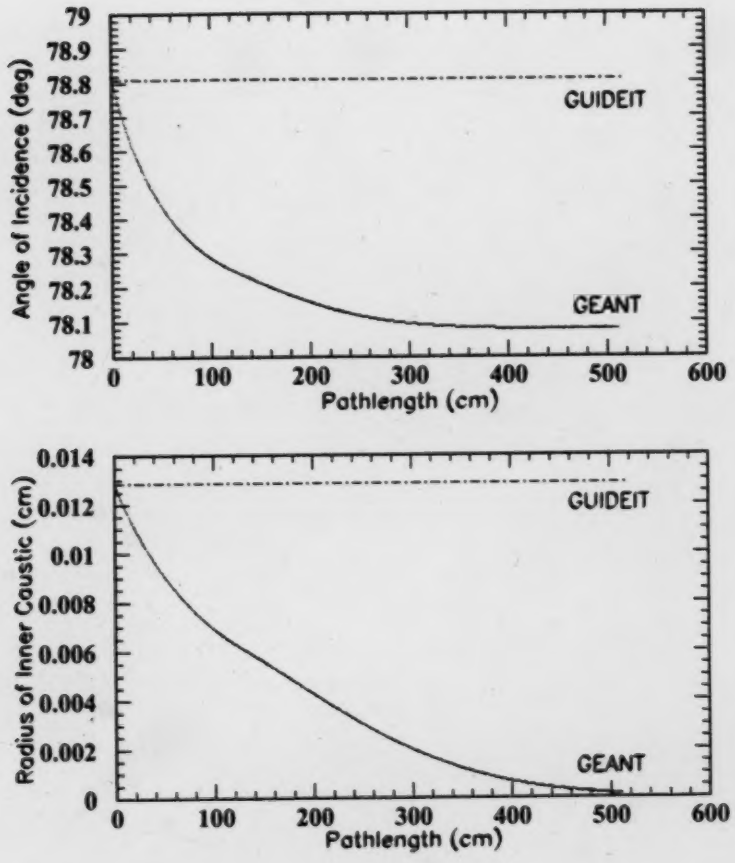

Figure 5.1: Variation of the angle of incidence and the inner caustic radius as a function of pathlength during GEANT tracking.

In contrast, the same fibre layout and photon emission position and direction were simulated using GUIDEIT. Both the angle of incidence and the radius of the inner caustic remained constant throughout the entire tracking procedure. Therefore in this respect GUIDEIT performs properly whereas GEANT does not. Due to the failure to provide a complete description of the scintillation and wavelength shifting mechanisms and the subsequent photon tracking in GEANT, GUIDEIT has been adapted to work alongside GEANT to perform the tracking of the secondary photons through the WLS fibre.

Therefore for the TE simulations the user has the option at runtime to perform the secondary photon tracking either via GEANT or GUIDEIT. If the GUIDEIT option is chosen, tracking of the primary scintillation photons proceeds as usual under the framework of GEANT. Once the photon is absorbed, GEANT passes the necessary hit position information to the various GUIDEIT routines which then isotropically emit a secondary photon and track it through the WLS fibre geometry. Only the WLS fibre geometry is defined for GUIDEIT. If a secondary photon escapes the fibre, photon tracking terminates and control is returned to GEANT. Upon termination of the GUIDEIT tracking, information regarding the current position, time of flight, pathlength, and wavelength are written out, but only for photons which have managed to reach the end of the fibre, corresponding to the location of the photomultiplier. Also recorded are the number of reflections occuring at each of the fibre surfaces. No information is stored for the secondary photons which have escaped the WLS fibre geometry. This limitation is due to the nature of the tracking method implemented by the GUIDEIT routines.

5.3.2 GEANT-GUIDEIT Geometry Description Limitations

A further limitation of GEANT has been encountered through the unavoidable description of the bent fibre segments in the TE scintillating tiles via a series of connected straight fibre segments with non-planar end-faces. This geometric approximation was dictated by the limited number of GEANT volume definitions available. The geometric accuracy of the bent fibre constructed from the straight cylinders improves with increasing number of segments per fibre bend. This has the disadvantage of increasing the number of surfaces which the photons must intersect, and as a result increases the tracking time. The photon ray path parameters will also likely vary due to the imperfect geometrical description. Figure 5.2 demonstrates the GEANT approximation of a torus segment with the series of cylinders along with the valid torus segment. The difference in the two geometry descriptions is predominant at the interface of two straight segments which extend beyond the definition of the torus volume. The accuracy of the results obtained from GEANT alone are therefore limited in the context of a full simulation of both the primary and secondary photon emissions.

The GUIDEIT software was adapted in order to overcome the geometric limitations of GEANT and provide an accurate description of bent fibres. Version 1.1 of GUIDEIT permitted the description of straight cylinders or fibres only. The utility of GUIDEIT was extended further as part of this work through the addition of a new shape definition describing the toroid geometry, thereby allowing the description of bent fibres to be simulated in combination with GEANT. Such an addition is not easily achievable in the GEANT framework. The necessary routines to define the toroidal geometry and to perform the calculation of the ray-surface

intersection points in GUIDEIT were added. Determination of the intersection points requires the calculation of the real roots of a quartic polynomial. A further discussion of the implementation of toroidal tracking in GUIDEIT can be found in Appendix A.

As will be mentioned in the discussion of the TE prototype and final design scintillating tiles in Chapter 7 and Chapter 8 respectively, a large portion of the wavelength shifting fibres embedded within the scintillator will be bent through an arc of constant curvature, and many of the primary scintillation photons will be absorbed in these regions. The hit position determined by GEANT though in actuality may be outside the definition of the toroidal shape, as recall that the bent fibre sections must be described in GEANT as a series of aligned cylinders with nonplanar faces. If the hit position were to be directly translated to the toroidal geometry, the secondary photon generation point would many times originate outside the fibre and therefore not undergo tracking in GUIDEIT.

To remedy this problem, whenever a primary photon absorption has occured in a bent fibre region a new randomly determined emission position is determined in the plane defined by the absorption location seen by GEANT and the fibre axis which defines the normal to the plane. As a result the secondary photon emission position is guaranteed to be inside the region defined as the fibre core, and will be included in the toroidal geometry. Also the selection of a random position in the plane should accurately represent the distribution of primary absorption locations relative to the fibre axis for all locations around the fibre layout.

The combined accuracy of the ray path parameters and toroidal geometry tracking of GUIDEIT and the particle kinematics and energy loss calculations

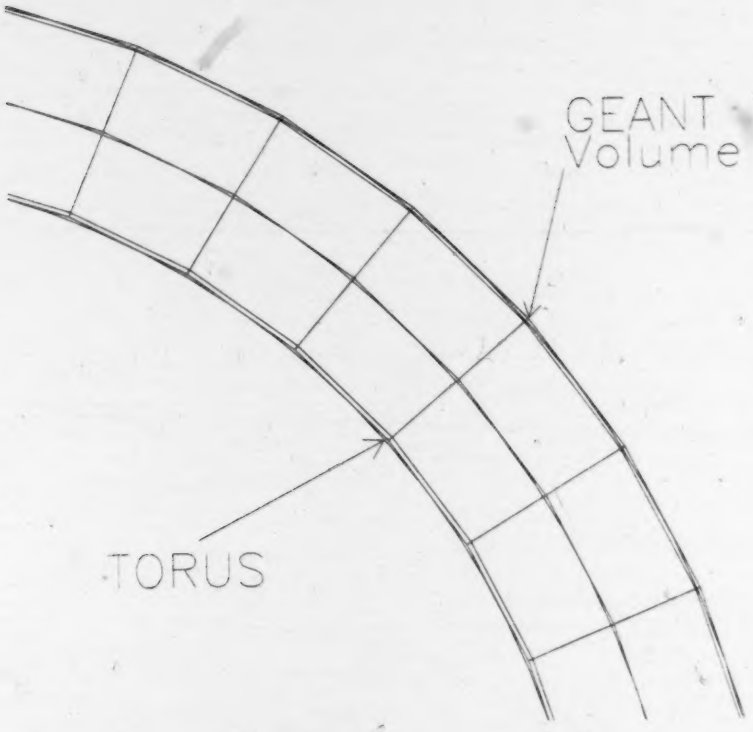

Figure 5.2: GEANT approximation of a toroidal segment by a series of connected cylinders with noncoplanar faces.

of GEANT together form an accurate and efficient method of providing a full simulation of a scintillating-wavelength shifting fibre detector.

5.4 Parallel GEANT

As mentioned previously in Section 5.2 a reduced number of photons is tracked in GEANT to simulate the scintillation mechanism. For the generated Monte Carlo events the number of photons to be simulated is still quite large.

To assist in the production of Monte Carlo several routines have been written by myself in order to distribute the workload of event generation onto both networks of workstations and massively parallel computers. The distributed or parallel GEANT was achieved utilizing the PVM (Parallel Virtual Machine) [42] programming library of software. PVM allows for a relatively simple execution of a wide variety of parallel computing paradigms for a distributed memory system of computers, including message passing.

The Master-Slave method was chosen to generate Monte Carlo for the simulation of the TE prototype and final design scintillating tiles. In this approach a Master program decides the number of Slave processes which are to be executed (typically the number of computers available) and a set number of events are generated by each of the Slaves which operate independently. This degree of parallelism is known as event level parallelism, and is the the greatest degree of parallelism achievable with the version 3.21 of GEANT. The smallest unit of execution on any given computer which can also be running on another computer concurrently is the Monte Carlo event generation loop. For simplicity, each Slave process is a separate GEANT program generating events independently, with all communication occuring only between the Master and Slave processes. Upon startup, the Master process distributes to each Slave information to maintain event ordering and unique random number seeding. The Slave process then performs the three typical GEANT stages of initialization, event processing, and termination. Once a Slave processes has completed their task, a message is returned to the Master process indicating that the work has finished. When all Slaves have finished, the Master process then merges the Monte Carlo into a single data set, which can later be analyzed.

By running the GEANT-GUIDEIT simulation software in parallel, powerful computing resources such as the University of Alberta's SP2 (Scalable Power Parallel) computer and network of 21 RS/6000 workstations have been exploited to generate large numbers of event samples in a time much shorter than would be achievable simply using the computing available locally. The parallel GEANT application has also been successfully applied to both the ATLAS and OPAL detector simulation software packages.

CHAPTER 6

Single Optical Fibre Measurements With a CCD

The suitability of GUIDEIT as a ray tracing tool to simulate the propagation of light in the wavelength shifting fibres of the TE scintillating tiles is demonstrated though the simulation and measurement of the photon distribution in the cross-section of a single wavelength shifting fibre. An examination of this distribution will provide insight into the necessity for a high quality connector, such as that described in Chapter 3, to couple the wavelength shifting and clear optical fibres of the TE detector. The influence of various connector geometries on the measured light output of the TE tiles is covered in Chapter 7 with a more in depth discussion of the connectors given in Appendix B.

6.1 The Single Fibre Light Yield Experiment

To measure the distribution of photons in the cross-section of a typical wavelength shifting (WLS) fibre an experiment was constructed using a high resolution CCD array. Previous experiments [43] have been carried out elsewhere using a similar technique also to measure the photon distribution. The general layout of the experiment is shown schematically in Figure 6.1.

The 1 mm diameter BCF-91A WLS fibre of approximately 30 cm length was stimulated with incident blue light at a wavelength of 470 nm. To achieve the

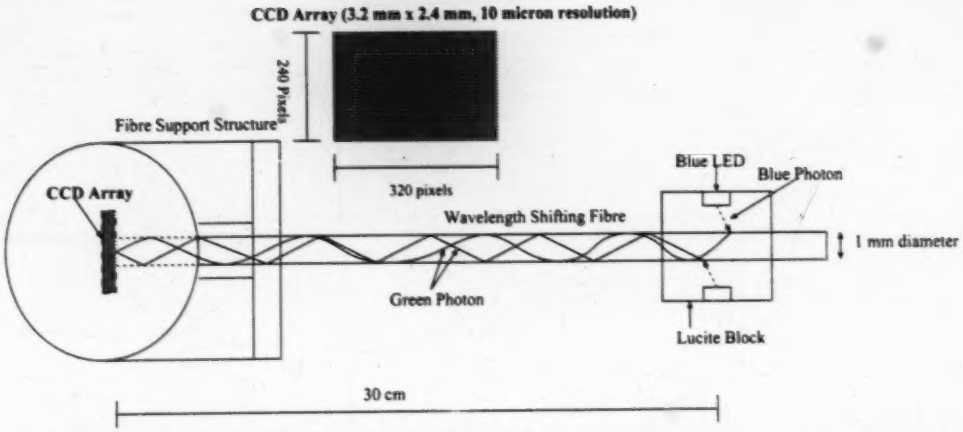

Figure 6.1: Schematic layout of the apparatus used to measure the light yield distribution in the cross-section of a WLS fibre stimulated with 470 nm blue light. The light output was measured with an approximately 3.2 x 2.4 cm^2 CCD array of 10 μm resolution.

stimulation an approximately 4 x 4 x 4 cm^3 lucite block was fitted with 4 Lite-On [44] 470 nm blue LEDs with the LEDs pointing to the centre of the block where the fibre was situated. A 1 mm diameter hole was machined though the centre of the lucite block to permit the placement of the fibre. The necessary circuitry to operate the LEDs was constructed. At the opposite end of the fibre was located a Connectix Black and White Quickcam [45] which operates through the use of an approximately 3.2 x 2.4 mm^2 CCD element. Work carried out has shown that the CCD array has a spatial resolution of approximately 10 nm [46]. Such a resolution is adequate to resolve the spatial structure of the wavelength shifted light which reaches the end of the fibre.

In order to determine the spatial distribution of the light yield in the fibre cross-section it was important to have the end of the WLS fibre as near as possible to the CCD array. Therefore, an IR filter located inside the CCD camera was

removed thereby reducing the the fibre-CCD array separation to the minimum value of approximately 1 mm. This separation is attributed to the presence of an $\approx$ 1 mm thick plastic window directly in front of the CCD. It was not possible to remove the plastic cover to permit the closer placement of the fibre to the CCD array. To achieve a smooth connection between the fibre and the plastic cover, the end of the fibre was polished, and fitted within a plastic mount to secure the fibre as close as possible to the plastic cover to the CCD array. Tension was applied by an elastic to the mount such as to press the fibre face uniformly against the plastic cover and minimize the separation. Although secured as closely as possible, the potential for a small air gap existed during data taking. A second small air gap is also possible to exist between the plastic cover and the CCD array itself, but has been neglected in the simulations. The thickness of the potential air gap between the fibre and plastic cover was estimated to be a maximum of 0.01 cm. The outer surface of the WLS fibre was wiped down and cleaned to remove any dirt or dust which may have collected during handling.

The end of the WLS fibre opposite to the end placed nearest to the CCD array was situated approximately 3 cm from the Lucite block. The far end of the fibre was not polished.

6.2 GUIDEIT Single Fibre Simulation

The arrangement shown in Figure 6.1 was specified through various input parameters to GUIDEIT. As the emission output of a LED is difficult to model, an approximation was made in order to simplify the execution. The wavelength shifting fibre was in the centre of a lucite block with 4 surrounding LEDs, with

the emission wavelength of 470 nm corresponding to an absorption length of approximately 3 cm as shown in Figure 3.7. Therefore, due to the trapping of the blue photons in the lucite block from total internal reflection, the assumption that the absorption location of the blue photons uniformly populates the fibre cross-section is a reasonable one. In GUIDEIT, only the propagation of the secondary wavelength shifted photons is simulated as there is no mechanism to simulate WLS within the GUIDEIT framework. As a result the emission locations of the secondary photons is determined at random so as to be uniformly distributed within the WLS fibre core, corresponding to the assumption made concerning the primary blue photon absorption.

To permit tracking of photons through an environment containing various layers of material where the photons can enter and exit a volume many times, the GUIDEIT tracking procedure was altered slightly to maintain the correct calculation of whether or not the criteria for total internal reflection is satisfied. In particular, the SURFACE subroutine was altered to ensure the correct value of refractive index was utilized for a photon which was for example traveling from a fibre cladding layer to the core material. This provision was not in place with the original GUIDEIT software, but has now been added to provide greater functionality to the program. Also because of the need to have photons possess the capability to travel through the same surface many times, and to simulate passage of photons through a toroidal geometry the list of options made available to a photon which is passes through a GATE has been increased. A GATE is defined as a surface through which a photon can travel that has an action associated with it, such as filling a histogram or indicating whether the next or previous sequence of objects is about to be entered. To provide the capability to track through multiple layers and toroidal geometries, the various GATE actions were extended

to also allow indication that either the next+1 or previous−1 sequence is about to be entered. This addition is necessary for the description of both straight and bent optical fibres.

The possibility of a small air gap between the face of the WLS fibre and the plastic cover was simulated with a thickness of 0.01 cm. The refractive index of the plastic cover was also unknown as no value was available from the manufacturer. Therefore all simulations were performed for the three values of refractive index given as 1.45, 1.50, and 1.55. These values were chosen due to their proximity to the refractive indices of various standard materials such as Lucite (≈1.49), Borosilicate glass (1.474), and fused quartz (1.458) [31].

The secondary wavelength shifted photons are emitted isotropically within the fibre covering both the forward (toward the CCD array) and backward (away from the CCD array) directions. Although the fibre face in the backward direction was not polished, photons which are emitted in the backward direction may still reflect and propagate down to the CCD array. Therefore, simulation runs were performed that included photons exclusively emitted in the forward direction as well photons emitted in both the forward and backward directions. The simulations were also performed with bulk photon attenuation cuts both applied and not applied. A photon attenuation length of 360 cm was assumed.

All combinations of photon emission direction, air gap/no air gap, with and without bulk attenuation loses, and refractive index were simulated. For each data sample one million photons were generated and tracked. The values of the core-cladding and cladding-air surface reflectivities were also set to 0.9999 and 0.99, respectively, and indicate the quality of the fibre surface finish. The surface reflectivity of the fibre-airgap interface was set to 0.98 to allow for some small

imperfections in polishing of the fibre face.

6.3 Experimental Data and Simulation Results

6.3.1 Image Processing

Measurement of the light yield from the single fibre was performed by software which controlled the readout of the CCD array. The three variables of Brightness, White Balance, and Contrast determined the image readout. The image file was converted to an ASCII text file which gave a pixel by pixel readout of the measured intensity. The scale of measurement is arbitrary and has a maximum value set in the software of 63 units. The fibre images taken were arrived at by adjusting the settings of the three variables such as to meet two criteria. The first was to ensure that the maximum range of pixel intensity values were achieved, covering the range of 0 up to 63 as completely as possible. The second criteria was that the amount of signal seen in the CCD array for the case of zero illumination of the fibre with blue light yielded on average some spurious noise in the CCD array. By adjusting the variables in order to detect spurious noise we achieve a good sensitivity to single photon hits at the CCD array, and also made use of the full dynamic range available.

6.3.2 Experiment and Monte Carlo Results

The CCD array consists of 320 x 240 pixel elements. The images taken were rebinned to a 80 x 60 array to ensure adequate statistics on a bin-by-bin basis. Figure 6.2 shows a three dimensional view of the measured signal for the single

WLS fibre. Although the the fibre image was centered on the CCD array the image extended slightly beyond the available viewing range.

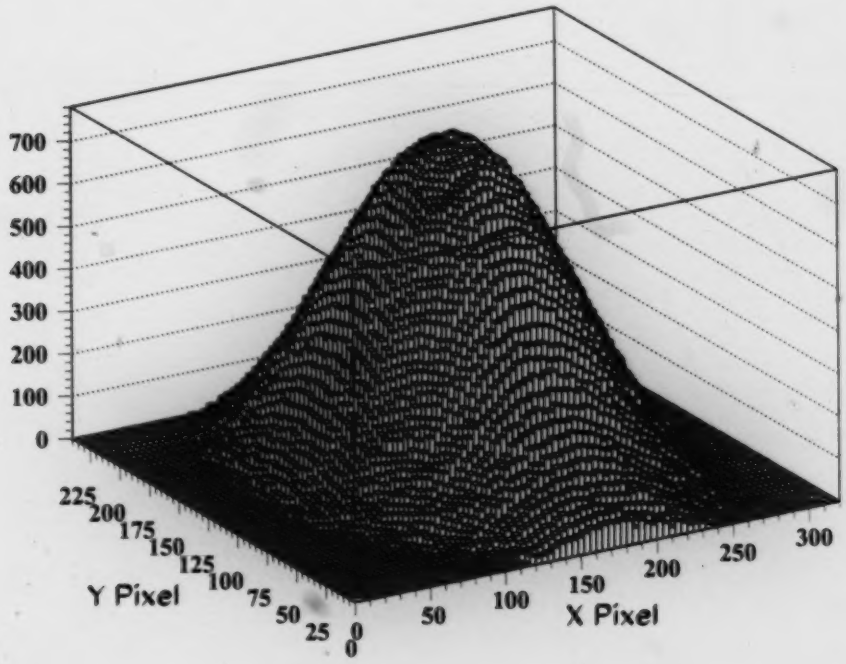

Figure 6.2: Three dimensional view of the light yield signal of a single WLS fibre readout via a CCD array approximately 1 mm from the WLS fibre end. The CCD array is 320 x 240 pixels with a linear resolution of 10 microns.

A comparison of the measured image to that predicted by simulation can be simplified by examining the data in terms of both a profile histogram and a slice histogram taken through the centre of the image. A profile histogram displays the measured two dimensional results as a one dimensional histogram through binning in one coordinate only. A slice histogram restricts the range of values of

a coordinate over which binning occurs while displaying it as a function of the other variable. By taking a slice through the centre of the distribution one can obtain a good estimate of the distribution about the symmetry axis define by the fibre axis. As a result a good comparison between experiment and Monte Carlo is achieved.

Figure 6.3 demonstrates the profile distributions of both the measured light yield and normalized Monte Carlo for a plastic cover refractive index of 1.45.

The Monte Carlo results which assumed a refractive index of n=1.45 with the presence of a 0.01 cm airgap between the WLS fibre face and the plastic cover match the data well, with the best description belonging to the case where photons were emitted in both the forward and backward directions. For the profile histograms the data and Monte Carlo are in good agreement with some excess entries at the centre position and at the tails of the distribution.

Figure 6.4 demonstrates the centre slice distributions of both the measured light yield and normalized Monte Carlo results. The centre slice distributions were arrived at by examining the image pixel values in the range of -0.002 cm $\leq y \leq$ 0.002 cm as a function of x coordinate. The centre slice data histogram on average passes through the Monte Carlo prediction assuming both forward and backward photon emission, a 0.01 cm airgap, and a photon attenuation length of 360 cm. A good prediction is also achieved by the Monte Carlo in which photons were emitted only in the forward direction with an airgap, and demonstrates less variation from bin-to-bin. In both cases a slight excess light yield at the centre of the image is expected from Monte Carlo compared to the measured results. The good prediction of the forward only emission Monte Carlo,

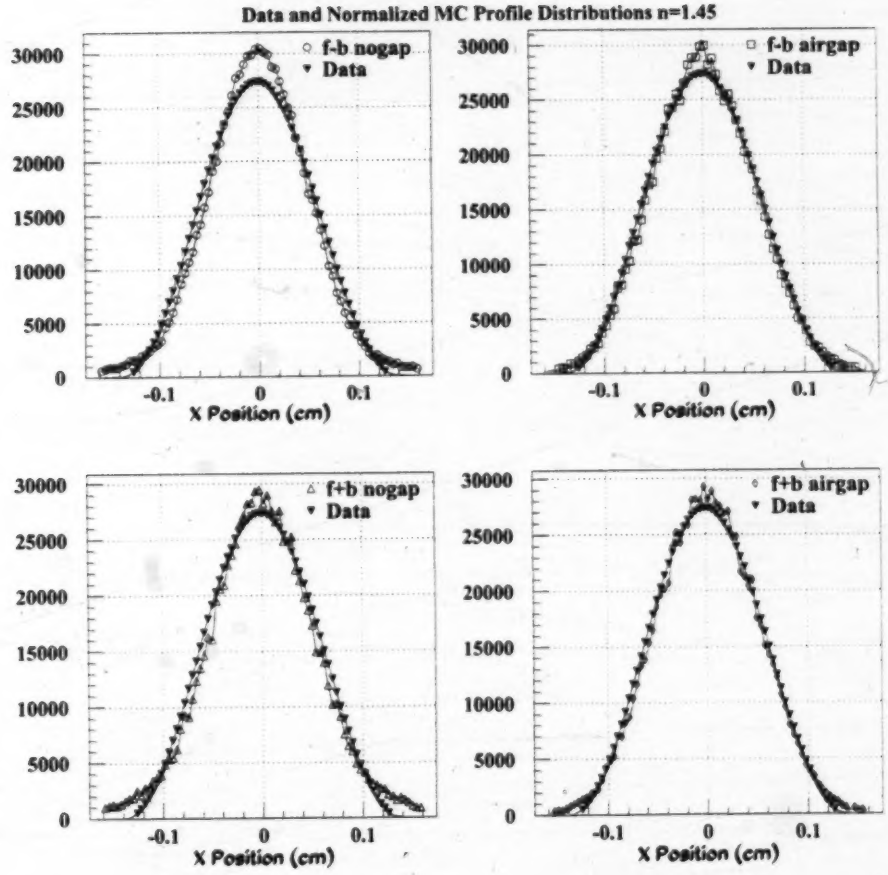

Figure 6.3: Profile view of the measured and normalized Monte Carlo light yield distributions for a plastic cover refractive index of 1.45. The top two histograms show the Monte Carlo predictions assuming photon emission only in the forward direction both with (f-b airgap) and without (f-b nogap) an airgap between the WLS fibre and the plastic cover. The bottom two histograms show the Monte Carlo predictions assuming photon emission in both the forward and backward directions also with (f+b airgap) and without (f+b nogap) an airgap. In all cases a photon attenuation length of 360 cm is assumed.

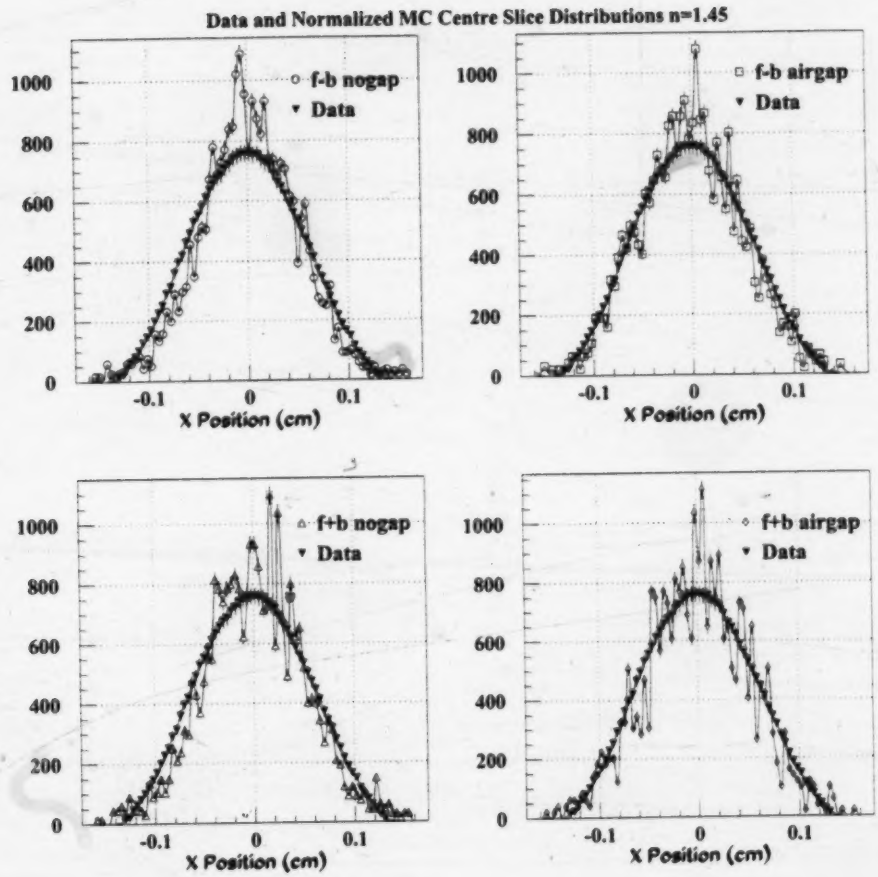

Figure 6.4: Centre slice ($-0.002\ cm \leq y \leq 0.002\ cm$) of the measured and normalized Monte Carlo light yield distributions for a plastic cover refractive index of 1.45. The top two histograms show the Monte Carlo predictions assuming photon emission only in the forward direction both with (f-b airgap) and without (f-b nogap) an airgap between the WLS fibre and the plastic cover. The bottom two histograms show the Monte Carlo predictions assuming photon emission in both the forward and backward directions also with (f+b airgap) and without (f+b nogap) an airgap. In all cases a photon attenuation length of 360 cm is assumed.

particularly along the tails of the distributions, could indicate that the rough surface finish of the fibre end away from the CCD array prevented a large portion of backward direction photons from reflecting and reaching the CCD.

Both the profile and centre slice histograms for the refractive indices of 1.50 and 1.55 do not agree very well with the data and are therefore not shown.

6.3.3 Photon Distribution in the Fibre Cross-Section

The profile and central slice distributions shown above are clear indicators of the photon distribution in the fibre cross-section immediately prior to exiting the WLS fibre. As mentioned previously in Chapter 4 the trapping efficiency of the fibre is determined by the refractive indices of the core and cladding materials, and is dependent upon the radial location within the fibre core where the photon originates. A reasonable assumption is that the wavelength shifted photons originating at the far end of the fibre are uniformly distributed in the fibre cross-section. If this assumption is valid then geometric optics dictates that the vast majority of the surviving photons that have propagated down to the other end will be skew rays. Such skew rays will be therefore more densely concentrated towards to outer radial region of the fibre core. Figure 6.5 shows a lego plot demonstrating the annular region in the fibre cross-section seen from the GUIDEIT simulation Figure 6.6 shows an end-on view of the photon distribution in the fibre cross-section.

The transition from the annular region at the fibre end to the peaked central distribution at the CCD array is evident from the series of distributions taken at 0.02 cm intervals along the direction of the fibre axis as shown in Figure 6.7, commencing at a distance of 0.01 cm from the fibre. The increased density of photons at the outer limits of the fibre core cross-section in Figures 6.5, and

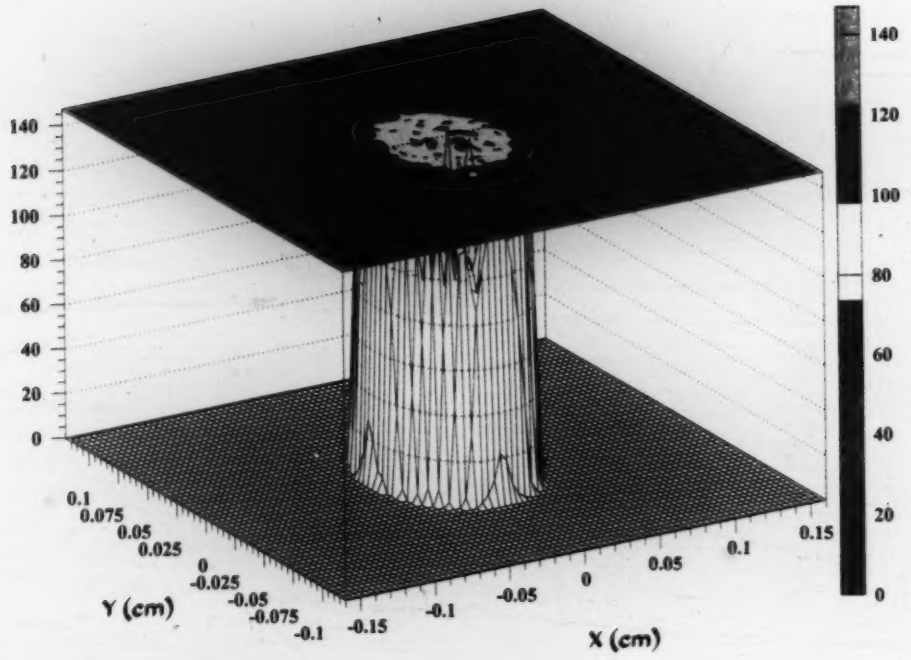

Figure 6.5: Distribution of photons in the fibre cross-section immediately prior to exiting the fibre.

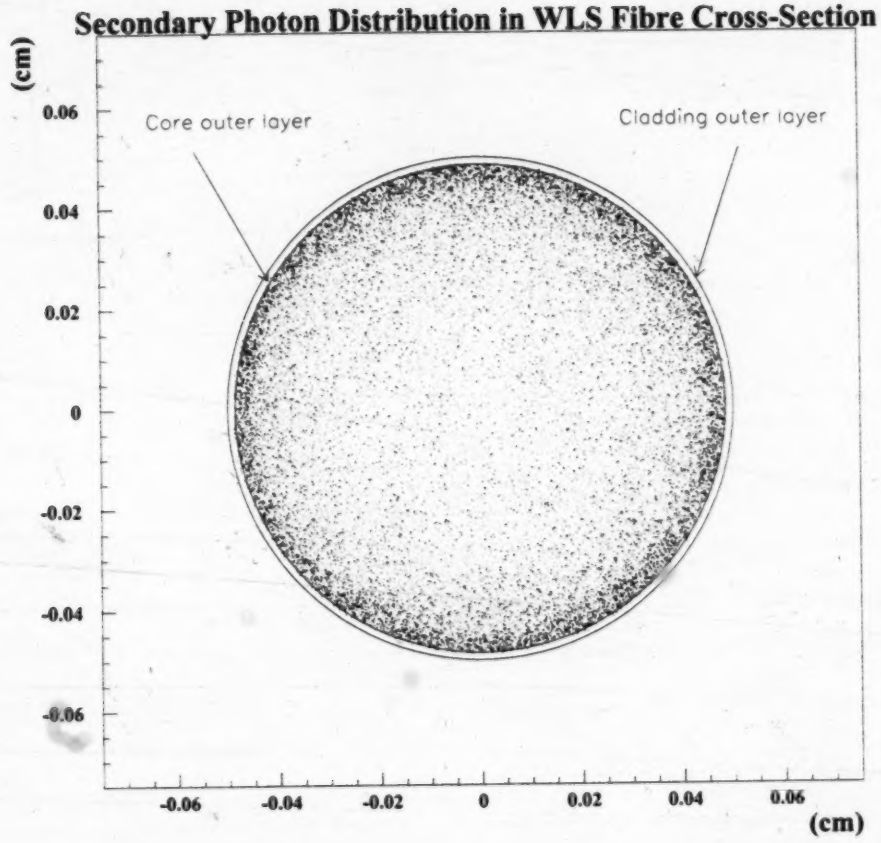

Figure 6.6: Distribution of photons in the WLS fibre cross-section for arising from uniformly distributed emission positions. The radial extent of the fibre core and cladding layers is also shown.

6.7 at a separation of 0.01 cm, steadily moves towards the centre of the viewable CCD aperture. The distribution not only transforms from annular in shape to a central peak but also spreads out beyond the radius of the WLS fibre.

Although the measurements presented include the effect of a intermediate layer of material between the WLS fibre and the CCD array, the resulting distributions are a clear indication of the increased photon density towards the fibre core-cladding interface due to the presence of skew rays. The increased photon density at the outer limits of the fibre core has also been observed by experiments carried out elsewhere [43].

6.3.4 Square Optical Fibre Simulation Results

Another confirmation of the tracking capabilities of the GUIDEIT software is evident when considering the simulation results for a 1 mm diameter square optical fibre. A square fibre was simulated in order to demonstrate the expected light yield distribution difference compared to that achieved with a round fibre. From optical ray theory, the trapping efficiency of a round fibre depends upon the relative refractive indices of the core and cladding layers as well as the radial location of the photon emission point. A greater number of photons will be trapped in the outer regions due to the increased acceptance of photons emitted with larger azimuthal angles, as discussed in Chapter 4. For square fibres though the geometric acceptance is constant for every point in the fibre cross-section [47]. As a result the end face of a uniformly illuminated WLS fibre will also be uniformly populated by photons.

Figure 6.8 demonstrates the simulated light yield distribution seen at the square fibre face immediately prior to exiting the fibre as well as at a distance

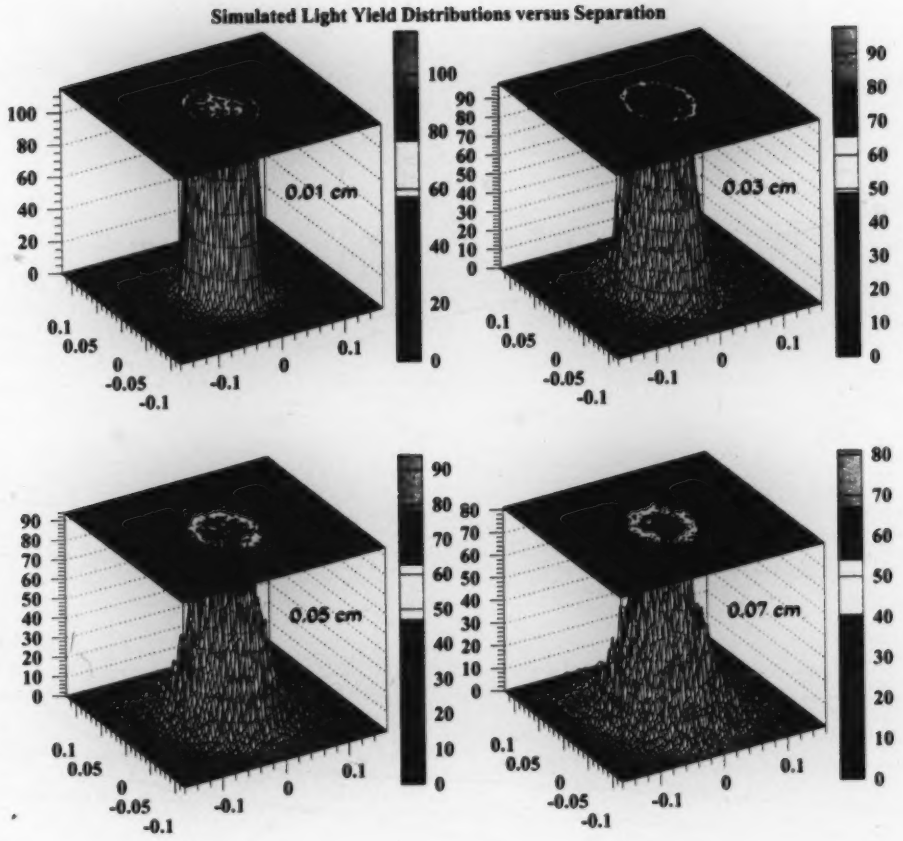

Figure 6.7: Distribution of photons in the plane perpendicular to the fibre axis for varying distances from the fibre end toward the CCD array.

of 1 mm from the fibre end. The 1 mm thickness corresponds to the plastic material directly in front of the CCD array, and a refractive of 1.45 has been assumed. A 0.01 cm thick airgap was also simulated to exist between the fibre face and the plastic cover. As can be seen the end face of the fibre from which the photons are about to escape is on average uniformly populated with photons. Even after traveling a short distance of 1 mm from the fibre the distribution has shifted and becomes peaked towards the centre of the fibre. The distribution is not entirely symmetric about the fibre axis as the square shape of the fibre is should still be apparent in the simulated CCD image. This difference from the round fibre light yield is made even more clear upon considering the square fibre Monte Carlo profile and centre slice distributions shown in Figure6.9. The square fibre distribution tails do not have the same extent as that seen for a round fibre, and greatly exceeds the observed photon intensity in the centre of the CCD image.

No square fibre was available to experimentally determine the light yield.

The close agreement between the simulation and the data for a 1 mm diameter WLS fibre has shown the capability of GUIDEIT to enhance the existing GEANT ray tracing routines. The application of the GEANT-GUIDEIT combination to simulate the prototype and final design TE scintillating tiles will now be discussed.

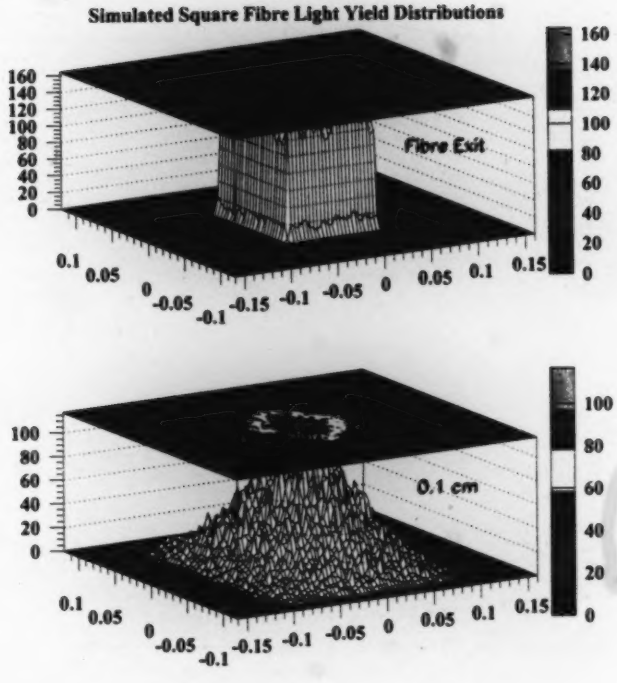

Figure 6.8: Distribution of photons in the square fibre cross-section immediately prior to exiting the fibre and after traveling through 1 mm of plastic of refractive index 1.45 towards the location of the CCD array.

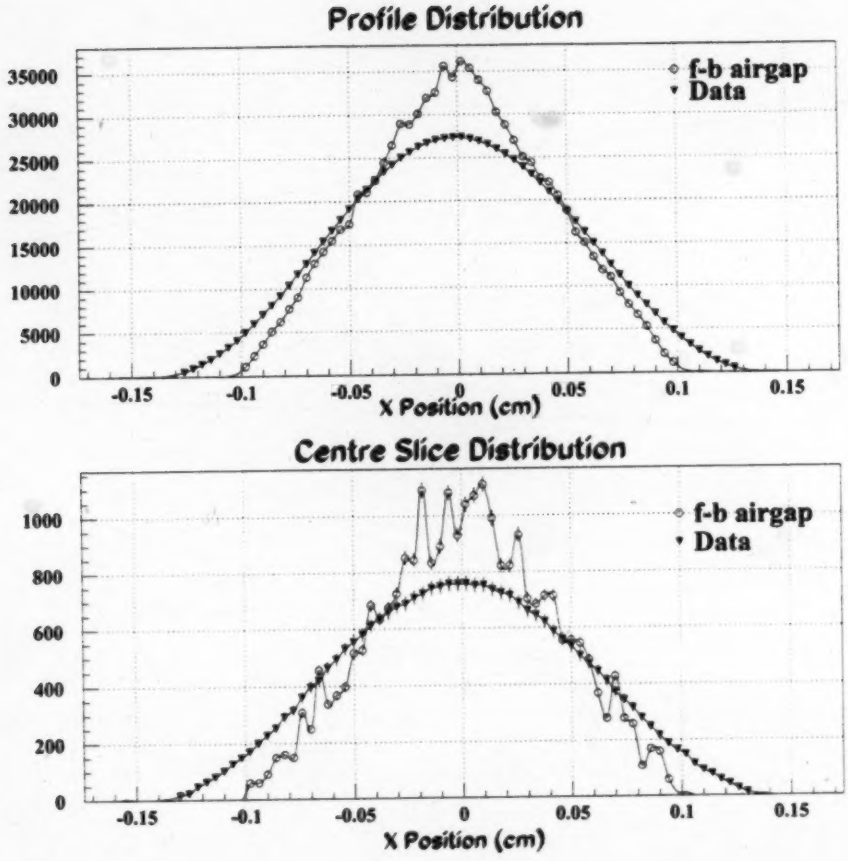

Figure 6.9: Profile and centre slice distributions of the measured round fibre light yield and Monte Carlo results for a square optical fibre with a plastic cover refractive index of 1.45. The Monte Carlo predictions assume photon emission only in the forward direction with an airgap (f-b airgap) between the WLS fibre and the plastic cover. A photon attenuation length of 360 cm is also assumed.

CHAPTER 7

Three Sigma Fibre Layout Scintillating Tiles

Much of the prototype testing of the TE scintillating tiles was performed by measuring the light yield due to the passage of incident cosmic ray muons as a function of position on the tile face. The use of cosmic rays as a diagnostic tool was well suited to determine the detector response to the passage of minimum ionizing particles.

7.1 Minimum Ionizing Particles

Energy loss in matter by charged particles (other than electrons) which are moderately relativistic occurs primarily through ionization. The mean rate of energy loss for such particles is given by the Bethe-Bloch equation [31, 30],

$$-\frac{dE}{dx} = 4\pi N_A r_e^2 m_e c^2 z^2 \frac{Z}{A}\frac{1}{\beta^2}[\frac{1}{2}\ln\frac{2m_e c^2\beta^2\gamma^2 T_{Max}}{I^2} - \beta^2 - \frac{\delta}{2}] \qquad (7.1)$$

where: N_A is Avogadro's number; z the charge of the incident particle in units of e; Z the atomic number of the medium; A the atomic mass of the medium; β is v/c of the incident particle; m_e the electron mass; c the speed of light; γ given by $1/\sqrt{1-\beta^2}$; T_{Max} the maximum kinetic energy which can be imparted to a free electron; and δ the density effect correction.

At non-relativistic energies the energy loss dE/dx is dominated by the overall $1/\beta^2$ factor and decreases with increasing velocity until a minimum is

reached at $v \approx 0.96\,c$. At this point particles are considered to be minimum ionizing. For particles of the same charge the minimum in dE/dx is almost equal.

7.2 Cosmic Rays

Cosmic rays arriving at the surface of the earth have a mean energy of approximately 4 GeV [31]. Below energies of ≈1 GeV the energy spectrum is almost flat, and gradually rises to the primary distribution in the energy range of 10 to 100 GeV. The integral intensity of vertical muons with energies in excess of 1 GeV at sea level has been measured to be approximately 70 $m^{-2}\,s^{-1}\,sr^{-1}$ [48, 49]. This corresponds to an observed incident rate of $\approx 1.8\,x\,10^2$ $m^{-2}\,s^{-1}$ and is roughly equivalent to 1 $cm^{-2}\,min^{-1}$. The angular distribution of cosmic rays varies as $\cos^2\theta$ for muons of approximately 3 GeV energy, and approaches $\sec\theta$ for increasing energies.

Since the TE detector is required to be sensitive to minimum ionizing particles the cosmic rays incident upon the various prototype tiles were hardened by passing through approximately 12 cm of lead to ensure the muons triggered upon were indeed minimum ionizing, with energies in excess of approximately 250 MeV.

7.3 Experimental Setup: The Cosmic Ray Telescope

The performance of the various prototype scintillating tile geometries was measured through the use of a cosmic ray telescope. Figure 7.1 schematically shows

the layout of the scintillating tile and the telescope components. A pair of delay line wire chambers were placed above and below the scintillating tile, and provided the spatial coordinates of the cosmic ray muon trajectory with an accuracy of ≈ 2 mm in the x-y plane. Three scintillation detectors were arranged to act as a trigger and controlled the readout of the prototype scintillating tile. The third trigger scintillator, placed directly below a small layer of lead, was available to be put into the overall coincidence to require that the incident cosmic rays were indeed minimum ionizing.

Once a successful trigger has been accepted the ADC pulse height of the prototype tile was read out along with the spatial hit coordinates provided by the wire chambers.

In the prototype designs the wavelength shifting (WLS) fibres were coupled to 2.5 m long clear optical fibre. The optical fibres were subsequently connected to a Philips P2262B photomultiplier tube [50] which collects all the light and amplifies the signal. A fit of the photomultiplier ADC distribution using a Poisson distribution convoluted with a Gaussian photomultiplier single photon resolution function provides a measure of the mean number of photoelectrons.

The fitting function is given by

$$f(x) = \sum_{i=1}^{M} \frac{W_i}{\sqrt{2\pi}\sigma_i} \exp\left[-\frac{(x-\overline{x}_i)^2}{2\sigma_i^2}\right] \tag{7.2}$$

where M is the number of Gaussian photoelectron peaks, σ_i and $\overline{x}_i$ are parameters of the ith photoelectron peak such that $\overline{x}_{i+1} - \overline{x}_i$ is constant, and $\sigma_i = \sigma_1\sqrt{i}$ where σ_1 is the width of the single photoelectron distribution. This width represents fluctuations in the photomultiplier response due to the statistical nature

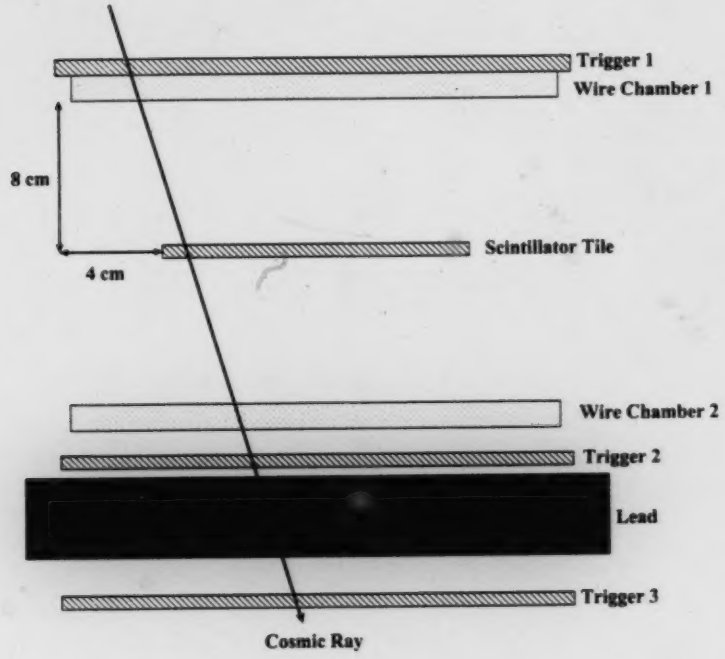

Figure 7.1: Layout of the cosmic ray telescope used to examine the prototype scintillating tiles.

of the photoemission at the photocathode, and secondary emission processes in the electron multiplier system. The values of W_i represent weighting factors such that the individual Gaussians are distributed according to a Poisson distribution of mean value μ and given by

$$W_i(i,\mu) = K\frac{\mu^i}{i!}\exp[-\mu] \tag{7.3}$$

During data taking the angular variation of the incident cosmic rays for recorded events were restricted to polar angles of $\theta < 15°$ in order to allow for a

well determined energy loss.

Various TE prototype designs were tested including scintillating tiles embedded with one, two, or three WLS fibres for readout. The most extensive work was carried out on the three fibre design, and will be discussed here in detail as it forms the basis of this thesis work.

7.3.1 The Three Sigma Prototype Tile

The three sigma fibre design consisted of a 10 x 10 cm^2 scintillator tile of 9.5 mm thickness embedded with three WLS fibre lengths arranged just inside the perimeter in machined grooves along both top and bottom faces of the scintillator. Each fibre was 1 mm in diameter and secured in its channel using optical cement with the same refractive index as the scintillator material. Two fibres were placed in the top channel while a single fibre was secured in the bottom channel.

The layout of each fibre included three 90° bends at a 2.5 cm radius of curvature, with a separation of 0.45 cm between the fibre and the scintillator tile perimeter. The layout of each fibre is termed *sigma* in shape. Each of the three fibres extended beyond the scintillator boundary for readout purposes, while the fibre ends which terminated within the scintillator were covered with a high reflectivity paint to redirect incident photons back towards the readout direction. The scintillating tiles were covered with Tyvec [51] reflective wrapping material and wrapped further with black tape to prevent any light leaks. Figure 7.2 shows a GEANT drawing of the three sigma fibre geometry and the relative positions of the fibres in the scintillator.

The average light yield and light yield uniformity were determined for each

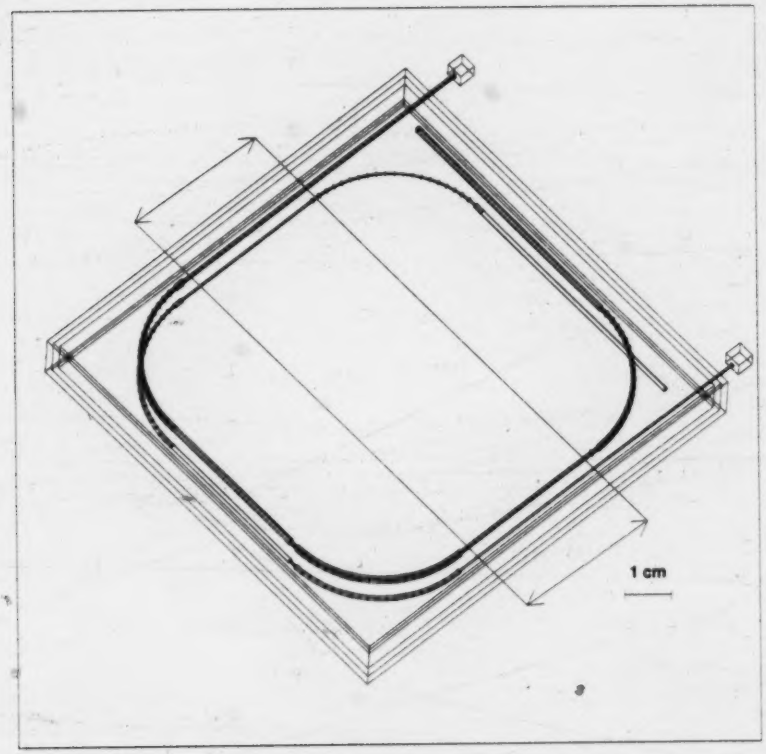

Figure 7.2: GEANT drawing of the 3 Sigma prototype scintillating tile geometry. The scan region examined with cosmic rays is also shown.

prototype configuration, both over the entire face of the scintillator as well as for a central 4.0 cm wide strip through the tile center. The scan region is also shown in Figure 7.2. Figure 7.3 [53] shows the measured ADC distribution for cosmic ray muons passing through the central scan region. The distribution was fit according to the function given in equation 7.2 and yielded a mean photoelectron output of 9.41 ± 0.03.

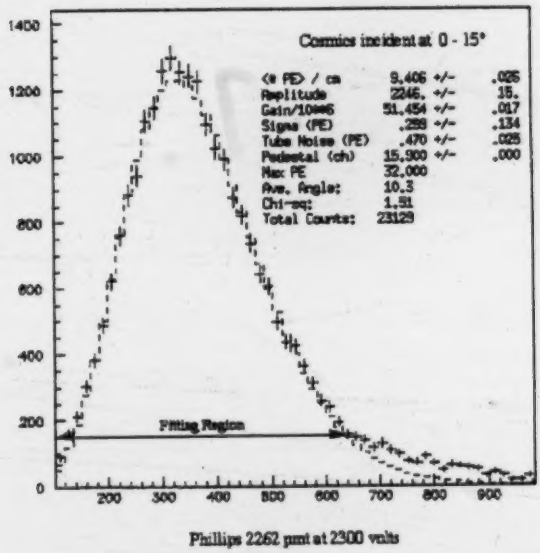

Figure 7.3: Measured ADC distribution for cosmic ray muons passing through the central scan region of the three sigma prototype scintillating tile. The distribution has a mean of 9.41 ± 0.03 photoelectrons.

7.4 Three Sigma Prototype Tile Simulation

The wrapping material surrounding the scintillator tile was simulated in GEANT as an airgap extending 0.5 mm beyond the surface of the scintillator tile with a covering perfectly reflecting surface. The reflective paint on the terminated fibre end was also designated to be perfectly reflective.

To simulate the three sigma prototype scintillating tile it was necessary to specify the placement of a circular cross-section fibre embedded within a tile of scintillator material, arranged in the form of a sigma layout as shown previously in Figure 7.2 for the three sigma fibre geometry.

It has been previously shown in Chapter 5 that GEANT Version 3.21 fails to correctly track photons down optical fibres. The inclusion of the various GUIDEIT ray tracing routines along with the additional capability of tracking through a toroidal geometry using GUIDEIT removes the flaws of the GEANT simulation and provides an accurate description of the prototype geometries.

In addition to the geometric description of the three sigma prototype tile the details of the measurement process using the cosmic ray telescope had to be considered in the simulation. In the GEANT simulation the incident cosmic ray muons were restricted to energies in excess of 250 MeV in order to be minimum ionizing, and were randomly distributed in $\cos^2\theta$ and ϕ with the requirement that $\theta < 15°$. These values match the conditions used in the studies performed with the cosmic ray telescope.

Upon passing through the scintillator material, the cosmic ray muons experience ionization losses and the emitted scintillation photons travel until absorbed within the core of the WLS fibre.

The mean free path of the scintillation photons inside the WLS fibre core material is wavelength dependent, as shown previously in Figure 3.7 for BCF-91A fibre. These values were provided as input to the GEANT simulation. Also provided were specifications of the material compositions of the various detector components including the WLS fibre core and cladding, scintillator, and wrapping materials. Based upon these values the GEANT program computes energy loss tables for the scintillator and other materials. The refractive indices and surface reflectivities for each component of the geometry are also specified in the simulation.

The Monte Carlo produces data structures containing values of: the photon hit position; wavelength; momentum; pathlength; time of flight;and number of reflections which occur at each surface for every primary scintillation photon which is absorbed inside a WLS fibre and for each secondary wavelength shifted (WLS) photon which reaches the end of the fibre where a photomultiplier would be located. To allow for a wide variety of material and construction conditions experienced during the prototype testing, all values of surface reflectivity and attenuation length were set to unity and infinity respectively. Various values of attenuation length and surface reflectivity were then implemented in a secondary analysis stage, allowing for a determination of the best parameters which bring the Monte Carlo into agreement with the measured results.

The main simulation program did not assume a specific WLS fibre to optical-fibre connector because of the wide range of possible connector geometries and construction quality. As will be shown in Appendix B the effect of the connector can be decoupled from the rest of the simulation. Each connector in turn will be applied to the value of the number of photons at the end of the WLS fibre to determine the number of photoelectrons at the photocathode. The simulation results provide a count of the number of photons which survive to the end of the WLS fibre rather than an ADC value. As a result of directly counting the photon output it is possible to easily determine the photoelectron output by applying the quantum efficiency of the photocathode.

The photomultiplier used in data taking was the Philips XP2262 [50] with a plano-concave lime-glass photocathode of refractive index n=1.52 at a wavelength of 500 nm. Figure 7.4 shows the spectral sensitivity $sk_e(\lambda)$ characteristic of the

λ (nm)	E(λ) (mA/W)	n(λ)
450.	77.5	0.2136
475.	67.5	0.1767
500.	55.0	0.1364
525.	40.0	0.0945
550.	27.5	0.0620
575.	13.0	0.0280

Table 7.1: Quantum efficiency of the Philips XP2262 photomultiplier tube Lime-glass photocathode as a function of wavelength.

photocathode. The sensitivity is defined as

$$E(\lambda) = \frac{I_k}{P(\lambda)} \tag{7.4}$$

where I_k is the photoelectric emission current from the cathode and $P(\lambda)$ is the incident radiant power. The spectral sensitivity is related to the quantum efficiency $\eta(\lambda)$ by

$$\eta(\lambda) = \frac{hc}{e}\frac{E(\lambda)}{\lambda} \tag{7.5}$$

Expressing $E(\lambda)$ in units of (A/W) and λ in nanometers simplifies equation 7.5 to

$$\eta(\lambda) = \frac{1240}{\lambda} E(\lambda) \tag{7.6}$$

Table 7.1 lists the approximate values of quantum efficiency for several values of photon wavelength.

As mentioned previously in Section 5.2 a reduced number of photons is tracked in GEANT to simulate the scintillation mechanism. The ratio of the simulated to true photon yield per MeV, along with the amount of energy deposited within the scintillator material, determines a multiplicative factor SF. The predicted number of photons to reach the end of the WLS fibre, given a realistic

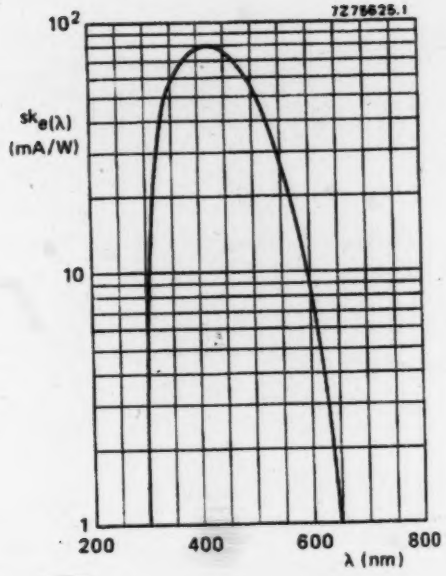

Figure 7.4: Quantum efficiency of the Philips XP2262 photomultiplier tube Lime-glass photocathode as a function of wavelength.

scintillation photon yield, is therefore the product of the scale factor SF with the Monte Carlo result for the number of photons at the end of the WLS fibre achieved with the GEANT reduced number of photons per MeV.

The quantum efficiency is applied to each of the photons individually as they reach the end of the WLS fibre. This is the most appropriate action as the quantum efficiency is wavelength dependent and a distribution of photon wavelengths are observed at the fibre end. For any given event the unscaled number of photoelectrons emitted if the photomultiplier tube were situated directly at the end of the wavelength shifting fibre is denoted by the quantity $N_{Unscaled}$. If a photon reaches the end of the fibre and successfully emits a photoelectron then

the number of unscaled photoelectrons emitted for the event i is given by

$$N_{Unscaled}(i) = N_{Unscale}(i) + QE(\lambda) \tag{7.7}$$

where $QE(\lambda)$ is the probability of photoelectron emission for a photon of wavelength λ as shown in Figure 7.4.

The multiplicative scaling factor SF needed to correct for the reduced number of scintillation photons emitted per MeV of energy deposited is only applied once all photons in the event have been tracked to completion. The final predicted number of photoelectrons N_{Scaled} for event i is given by

$$N_{Scaled}(i) = N_{Unscaled}(i) \cdot SF(i) \tag{7.8}$$

This distribution represents the number of photoelectrons which would be observed if the photomultiplier tube were coupled directly to the wavelength shifting fibre. By fitting the observed distribution with a Poisson distribution convoluted with a Gaussian the mean number of photoelectrons is determined. The effect of the connector will be shown to simply represent a multiplicative effect on the mean value. Therefore a good estimate of the final number of photoelectrons observed at the end of the optical fibre will be easily attainable.

Figure 7.5 shows a GEANT drawing of the passage of a muon through a prototype scintillating tile, where the secondary photon trajectory has been determined by GEANT. Visualization of the ray trajectory performed by GUIDEIT is not available.

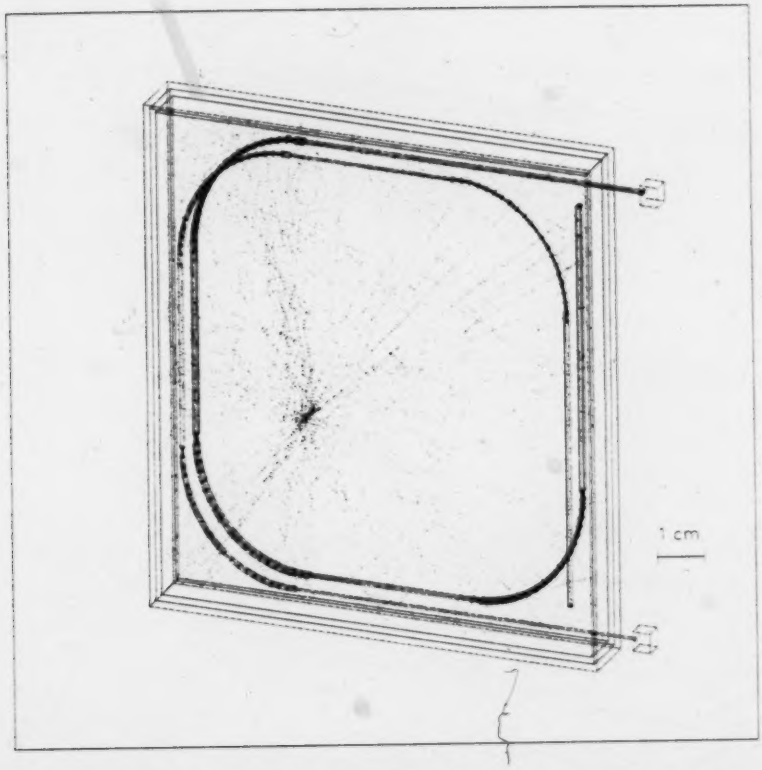

Figure 7.5: GEANT drawing of the passage of a muon through a 3 Sigma prototype scintillating tile and the emission of the scintillating photons. The trajectory of the secondary WLS photons as simulated by GEANT are also shown.

7.5 Cosmic Ray Scan and Monte Carlo Results

The three sigma fibre geometry was examined by measuring the ADC output due to the passage of cosmic ray muons both as a function of position across the face of the scintillator and globally to yield a measure of the average number of photoelectrons. A comparison with the generated Monte Carlo events was performed.

7.5.1 Light Yield Uniformity Studies

Due to the large amount of time necessary to simulate each event it was decided to restrict both the data sample and Monte Carlo such that events pass through a central 4.0 cm strip of the scintillator tile. Figure 7.2 schematically shows the region examined. The scan region overlaps with two straight sections of WLS fibre each a distance of 0.45 cm from the scintillator edge. The ADC light output is therefore expected to increase in these regions due to the enhanced geometric acceptance for scintillation photon absorption in the fibres.

With the experimental setup shown in Figure 7.1 the ADC output was measured for the passage of cosmic ray muons as a function of position in the y coordinate across the face of the scintillator. In each spatial bin the observed ADC distribution was fitted using a Poisson distribution convoluted with a Gaussian as given in equation 7.2 thereby yielding a measure of the photoelectron output as a function of position.

The simulation of the three sigma fibre geometry proceeded with the assumption of perfect surface reflectivities and infinite attenuation lengths. For each photon a record was kept of the number of interactions at each surface along with the total pathlength and time of flight. Each event was then analysed for a combination of surface reflectivity values. The simulated light output as a function of y-position was then compared to the measured result. Table 7.2 lists the range of surface reflectivity values used for each of the interfaces. The ranges selected were based upon material characteristics provided by the various component manufacturers and from other measurements of similar scintillation detector systems [41]. The values of the scintillation and WLS photon attenuation lengths were set to the scintillator and WLS fibre manufacturer's values of 380.0 cm and 360.0 cm,

TATBCUT	TASSCUT	AMCUT	CORSCUT	COCCUT	CLTCUT
0.800	0.500	0.650	0.650	0.995	0.985
0.850	0.550	0.700	0.700	0.999	0.990
0.900	0.600	0.750	0.750		
	0.650	0.800	0.800		
		0.850	0.850		
0.920	0.500	0.650	0.650	0.999	0.990
0.940	0.550	0.700	0.700		
0.960	0.600	0.750	0.750		
	0.650	0.800	0.800		
		0.850	0.850		

Table 7.2: Surface reflectivity values used in the Monte Carlo simulations of the three sigma fibre tile. Reflections may occur at the Tile-Air Top-Bottom (TATBCUT), Tile-Air Side-Side (TASSCUT), Air-Wrapping (AMCUT), Fibre Core-Reflective Surface (CORSCUT), Fibre Core-Cladding (COCCUT), and Fibre Cladding-Optical Glue (CLTCUT).

respectively, and were kept fixed in the simulation.

Reflection Characteristics

A large degree of uncertainty exists for the values of the surface reflectivities due to factors such as material production, machining quality, and wrapping technique. Therefore to determine the appropriate set of reflectivity values, each reflectivity parameter was varied independently of the remaining parameters, resulting in a total of 900 possible combinations to examine. The output for each combination is then compared to the observed photoelectron distribution. A method was devised to determine the reflectivities which best bring the Monte Carlo output into agreement with the measured results.

Reflections may occur at any of eight possible interfaces and the probability

for reflection is set by the values of the Tile-Air Reflectivity Top-Bottom (TATBCUT), Tile-Air reflectivity Side-Side (TASSCUT), Air-Wrapping (AMCUT), Fibre Core-Fibre End Surface (COSCUT), Fibre Cladding-Fibre End Surface (CLSCUT), Tile-Fibre End Surface (TSCUT), Fibre Core-Cladding (COCCUT), and Fibre Cladding-Glue (CLTCUT) reflectivities.

- Reflections at the Tile-Air Top-Bottom interfaces refer to reflections which occur at the interface between the scintillator tile and the surrounding air gap at either of the top or bottom large 10 x 10 cm^2 cast surfaces of the scintillator. Reflections which occur at this surface are dependent upon the value of the Tile-Air Top-Bottom reflectivity (TATBCUT).

- The Tile-Air Side-Side reflections also occur at the interface between the scintillator tile and the surrounding air gap but along the machine polished perimeter of the 9.6 mm thick scintillator tile. The probability for reflection at this surface is dependent upon the value of the Tile-Air Side-Side reflectivity (TASSCUT).

- Photons which fail to reflect at the Tile-Air interface will enter the 0.5 mm thick air gap and then undergo reflection at the surrounding wrapping material which is typically either Tyvec or aluminized mylar. Such reflections are controlled by the value of the Air-Wrapping reflectivity (AMCUT).

- The primary scintillation photons can also undergo reflection at the terminated WLS fibre end which is covered by a highly reflective paint. Reflections which occur at this interface are denoted as Tile-Painted Surface reflections, and in addition to being dependent upon the reflectivity of the applied paint, also depends upon the fibre surface polish quality. Reflections at this surface are controlled by the value of the Tile-Painted Surface

reflectivity (TSCUT).

Four reflection types are also possible for the secondary WLS photons.

- Upon emission within the WLS fibre core, the vast majority of the photons first reach the Fibre Core-Cladding interface and either undergo reflection or are transported to the fibre cladding layer. Reflections at this surface are controlled by the Fibre Core-Cladding reflectivity (COCCUT).

- Once in the fibre cladding layer, the photon propagates until it reaches the interface of the Fibre Cladding and the surrounding optical glue, which is used to affix the WLS fibres to the machined groves in the scintillator. Reflections which occur at this surface are controlled by the Fibre Cladding-Glue reflectivity (CLTCUT).

- Photons which propagate down the fibre in the direction away from the location of the photomultiplier tube may reach the terminated end of the fibre. This surface is typically polished and covered with a reflective paint. Reflections which occur at this interface are denoted as Fibre Core-Surface and Fibre Cladding-Surface reflections for photons which are respectively traveling in either of the fibre core or cladding layers. Reflections at this surface are controlled by the values of the Fibre Core-Surface (COSCUT) and Fibre Cladding-Surface (CLSCUT) reflectivity. These values of reflectivity are set equal to the Tile-Fibre End reflectivity (TSCUT) in the analysis.

The number of reflections at each of the eight interfaces are recorded for later analysis in the simulation. Although there are a large number of reflectivities to consider, it is possible to gain an indication of the reflectivity values which will provide a good constraint on the final selection of reflectivity parameters. This is

Scintillation Photons	Fraction of Photons
Scintillator - Air (Top - Bottom) Reflection	0.897
Scintillator - Air (Side - Side) Reflection	0.531
Air - Wrapping Material Reflection	0.545
Fibre Cladding - Scintillator Reflection	0.134
Fibre Core - Painted Surface Reflection	0.002
Fibre Cladding - Painted Surface Reflection	0.000
Fibre Core - Cladding Reflection	0.025
Scintillator - Painted Surface Reflection	0.000
WLS Photons	Fraction of Photons
Fibre Core - Painted Surface Reflection	0.477
Fibre Cladding - Painted Surface Reflection	0.000
Fibre Core - Cladding Reflection	0.997
Fibre Cladding - Optical Glue Reflection	0.003

Table 7.3: Fraction of primary scintillation and secondary WLS photons which encounter a reflection at the various geometric interfaces. The values reported were determined for the case of perfectly reflecting surfaces and infinite attenuation lengths.

provided by examining the fraction of the total number of emitted photons which undergo a reflection of a given type. Table 7.3 records the fraction of the total number of scintillation and WLS photons which experience a reflection at each of the interfaces under the condition of perfect reflectivity at each surface and infinite attenuation lengths.

From Table 7.3 it is seen that a high proportion of the scintillation photons will undergo at least one reflection at the Tile-Air (Top-Bottom) interface. This is expected since the two 10 x 10 cm^2 cast surfaces of the scintillator tile experience an increased geometric acceptance due to their large extent compared to the scintillator thickness of 9.6 mm. The next most dominant reflection types include reflections at the Tile-Air (Side - Side) and Air-Wrapping Material interfaces with

fractions of 0.531 and 0.545 respectively. The high proportion of reflections occuring at the Air-Wrapping Material interface is also expected due to coverage of the large cast scintillator surfaces with the wrapping material. A high likelihood of reflections occuring at the Tile-Air (Side - Side) interface is a consequence of the assumed perfect reflectivity at the Tile-Air (Top-Bottom) interface since each photon will easily be able to propagate the full width of the scintillator tile.

To a lesser degree the scintillation photons will experience reflections while attempting to propagate from the scintillator through the optical glue of the same refractive index and into the WLS fibre cladding layer. As the refractive index of the fibre cladding layer is less than that for the scintillator material it is possible for the photon to undergo total internal reflection and continue propagating in the scintillator material. Only if the angle of incidence is less than the critical angle will the photon enter into the WLS fibre. Approximately 0.134 of the scintillation photons experience a reflection at this interface.

Once inside the WLS fibre the scintillation photon will travel until it is absorbed. The distance travelled by the scintillation photon before absorption is wavelength dependent, as shown previously in Figure 3.7. Depending upon the photon wavelength the photon may travel a large distance and therefore undergo reflection at the Fibre Core - Cladding interface. The small fraction of scintillation photons which manage to enter the WLS fibre core and experience at least one reflection at the Fibre Core-Cladding interface is 0.025. This result assumes perfectly reflecting surfaces and no attenuation. Since scintillation photons can propagate down the WLS fibre before undergoing absorption it is also possible for such photons to reflect from the Painted Surface at the end of the fibre which terminates within the scintillator material. The fraction of scintillation photons which reflect at the Painted Surface is 0.002. The number of photons which either

propagate down the fibre cladding layer or are incident from the scintillator and experience at least one reflection at the Painted Surface is taken to be zero.

From the observation that a larger fraction of the scintillation photons reflect from the Tile-Air (Top-Bottom) interface, it is expected that there will be a high sensitivity of the Monte Carlo result to the value chosen for this reflectivity. This sensitivity may also exist, but to a lesser extent, to the reflection probabilities at the Air-Wrapping Material and the Tile-Air (Side-Side) interfaces.

The fraction of reflections experienced by the secondary WLS photons at the range of possible interfaces assuming perfect reflectivities and infinite attenuation lengths are also given in Table 7.3. As expected reflections at the Fibre Core - Cladding interface are experienced by nearly all (0.997) of the photons, with the exception of those most likely emitted inside the fibre core near to where the fibre extends from the scintillator out towards the expected location of the photomultiplier tube. The light yield is therefore expected to be very sensitive to any variations in the Fibre Core - Cladding reflectivity.

Since the WLS photons are emitted isotropically within the fibre it is expected that nearly one-half of the photons are emitted in each of the forward and backward directions, toward and away from the fibre end carried out to the photomultiplier location. A fraction of 0.477 of the total number of emitted wavelength shifted photons experience a reflection at the Painted Surface located at the terminated end of the fibre, and continue to propagate down the fibre towards the readout end. A small portion (0.003) of the WLS photons are also expected to propagate down the fibre cladding trapped between the core and the optical glue, which secures the fibre in the machined scintillator channels, due to total internal reflection. Almost no photons which are channeled down the cladding layer were

observed to experience a reflection at the Painted Surface.

From Table 7.3 it is easily seen that the majority of the scintillation photons will undergo at least one reflection at the Tile-Air (Top-Bottom) interface, with greater than half of the photons also experiencing reflections at the Tile-Air (Side-Side) and Air-Wrapping Material interfaces. Figure 7.6 shows the number of reflections experienced by the scintillation photons at each of the four most dominant reflection types. All of the distributions shown are for perfectly reflecting surfaces and infinite attenuation lengths. As expected the largest mean number of reflections occur at the Tile-Air (Top-Bottom) interface with a mean value of 10.04.

The high fraction of secondary WLS photons which undergo reflection at the Fibre Core-Cladding interface is also evident from the distribution of reflection counts shown in Figure 7.7. Again all of the distributions shown are for perfectly reflecting surfaces and infinite attenuation lengths. As seen from Table 7.3 only a small fraction of the photons (0.003) experience a reflection at the Fibre Cladding-Optical Glue interface. This is due to the fact that the fibre cladding layer acts to channel photons back into the fibre core. The subsequent photon direction may then be altered enough so as to trap the photon within the fibre core for the vast majority of its lifetime. Therefore it is rather unlikely that many wavelength shifted photons propagate over large distances within the fibre cladding.

Monte Carlo Chi-Square Minimization

The Monte Carlo simulation of the three sigma fibre tile was carried out assuming perfectly reflecting surfaces and infinite attenuation lengths. Each combination of possible reflectivities given in Table 7.2 was applied to the Monte Carlo sample.

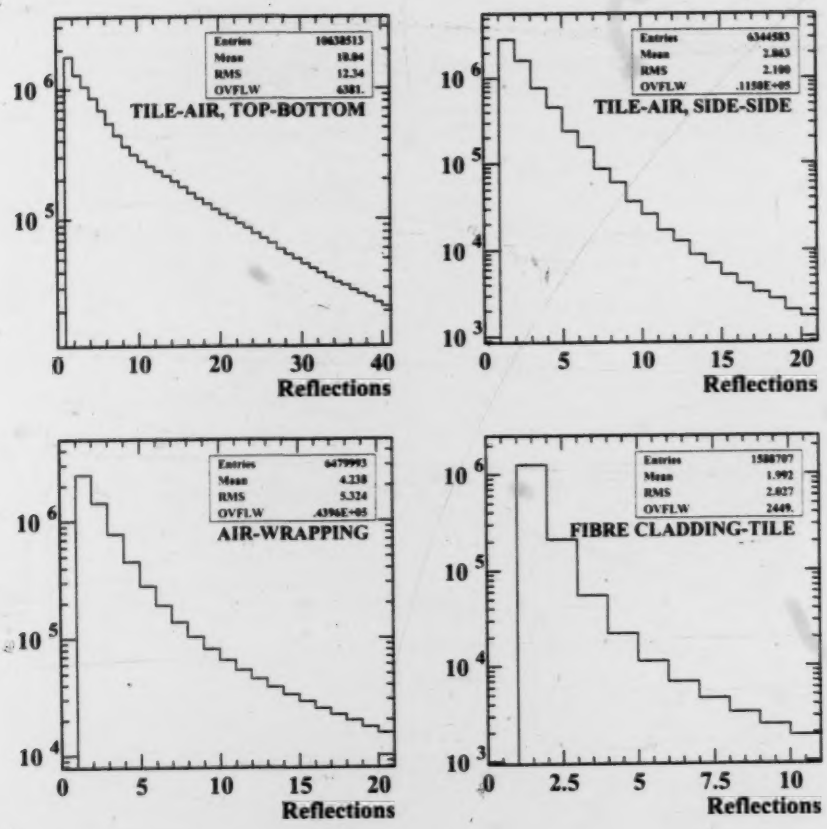

Figure 7.6: Number of reflections experienced by primary scintillation photons at the Tile-Air Top-Bottom, Tile-Air Side-Side, Air-Wrapping, and Fibre-Tile interfaces for perfectly reflecting surfaces and infinite attenuation lengths.

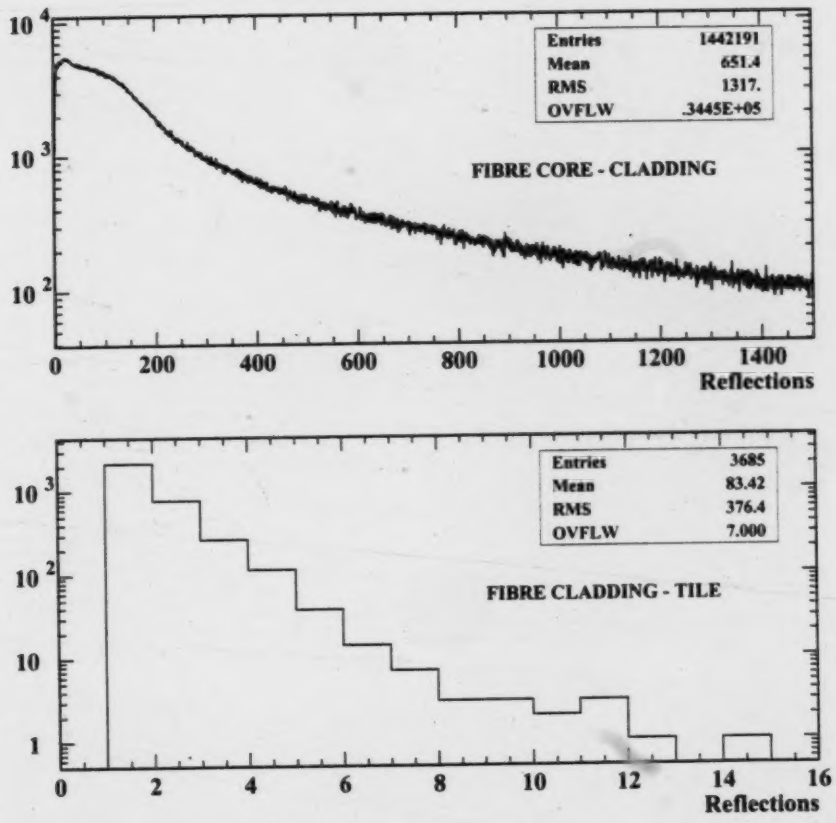

Figure 7.7: Number of reflections experienced by WLS photons at the Fibre Core-Cladding, and Fibre Cladding-Optical Glue interfaces for perfectly reflecting surfaces.

The resulting predictions of the light yield uniformity and average photoelectron output are then compared to measurement, with the best match between Monte Carlo and data determining the optimal set of reflectivities. The Monte Carlo and data were compared using the method of least squares with the optimal reflectivity values determined using chi-square minimization [30].

The method of least squares states that the function $f(x_i; a_j$ which best describes the observed distribution y_i minimizes the equation

$$\chi^2 = \sum_{i=1}^{n} \frac{(y_i - f(x_i; a_j))^2}{\sigma_i^2} \tag{7.9}$$

Although a specific function has not been tested in this analysis, the Monte Carlo prediction for the number of photoelectrons observed at the end of the WLS fibre represents the function value $f(x_i)$ in the least squares minimization of equation 7.9. The measured light yield in each spatial bin of the scan region is denoted by y_i.

For an analysis of the Monte Carlo results, a series of fitting routines based upon the Levenberg-Marquardt method [52] for fitting nonlinear functions was used. The routines [53] determine the number of photoelectrons observed for the passage of cosmic rays through the three sigma fibre tile geometry. Determination of the photoelectron output required fitting the ADC distribution with a Poisson distribution convoluted with a Gaussian as described previously in equation 7.2.

To accurately describe the observed distribution with such a function requires the determination of eight parameters, $PARAM(1)$, ... $PARAM(8)$ which included the following:

- PARAM(1): The mean number of photoelectrons per unit thickness, where unit thickness is defined as the scintillator tile thickness at normal incidence.

- PARAM(2): Amplitude of the histogram.
- PARAM(3): Gain of the photomultiplier tube / 10^6.
- PARAM(4): σ of the single photoelectron Gaussian (Photoelectron units) / $\sqrt{N}$ where N is the number of bin entries.
- PARAM(5): Tube noise (Photoelectron units)
- PARAM(6): Pedestal value.
- PARAM(7): Maximum number of Photoelectrons.
- PARAM(8): Average $\cos\theta$ value.

Initial values for each parameter are provided before the fitting procedure begins. During execution the values of $PARAM(7)$ and $PARAM(8)$ are kept fixed.

The Monte Carlo results provide a direct value for the expected number of photoelectrons which are present at the end of the WLS fibre and therefore does not simulate any effects which may be present due to a photomultiplier tube. Therefore, values such as the tube noise given by $PARAM(5)$ have been fixed at zero for fitting of the Monte Carlo results. The value of the photomultiplier gain was also altered to correspond to the Monte Carlo output. The relationship between the mean ADC value and the mean number of photoelectrons $\overline{NPE}$ is given by

$$\overline{NPE} = \frac{(\overline{ADC} - \text{Pedestal}) \cdot (\text{ADC Charge/Channel})}{(\text{Gain of PMT}) \cdot (\text{electron charge } e)} \tag{7.10}$$

where the pedestal value represents noise in the electron multiplier system of the photomultiplier tube in the absence of a true signal. Since the value of the ADC

charge/channel used in the measurements was 0.25 pC, equation 7.10 simplifies to

$$\overline{NPE} = \frac{1.56}{\frac{\text{Gain of PMT}}{10^6}}(\overline{ADC} - \text{Pedestal}) \tag{7.11}$$

To maintain a direct correspondence between the ADC values and the number of photoelectrons NPE the value of the photomultiplier gain $PARAM(3)$ was set to 1.56 for all fits performed on the Monte Carlo data. The average value of $\cos\theta$ was fixed in the fitting procedure.

The distribution of expected photoelectrons at the end of the wavelength shifting fibre for each spatial bin was fit using the above procedure. The value of $PARAM(3)$, the single photoelectron Gaussian resolution $\sigma/\sqrt{N}$, was varied so as to yield good reduced chi-square values for the fit performed in each of the 25 spatial bins. Once the optimal $PARAM(3)$ value was determined, the same value was used for the analysis of all remaining output files which correspond to the possible combinations of reflectivity parameters. Only the values of the mean number of photoelectrons ($PARAM(1)$) and the histogram amplitude ($PARAM(2)$) were allowed to vary during fitting procedure.

For each of the reflectivity parameter combinations the chi-square value of the Monte Carlo light yield uniformity was calculated according to equation 7.9, taking the variance σ_i^2 as the sum of the data and Monte Carlo distribution variances given by

$$\sigma_i^2 = \sigma_{MC,i}^2 + \sigma_{Data,i}^2 \tag{7.12}$$

The summation of the Monte Carlo and data variances is necessary since the means of both the data and Monte Carlo are determined from fits to the ADC and photon count distributions, respectively. Since the distributions are essentially Poisson in nature the variance is taken simply as the mean value from the fit procedure.

The values of the data and Monte Carlo variance are generally equal in value. Bin widths of 4 ADC channels and 4 photoelectrons were used in the fit of each distribution. The summation was performed over the 25 spatial bins of the scan region. The distribution of χ^2 values for the range of all possible reflectivity combinations is shown in Figure 7.8.

Shown in Figure 7.9 are the χ^2 values as a function of reflectivity value for each of the Tile-Air Top-Bottom, Tile-Air Side-Side, Air-Wrapping Material, and Fibre Core-Painted Surface interfaces. As mentioned previously and shown in Table 7.3, a high fraction of the scintillation and WLS photons experience reflections of these types, and therefore the resulting χ^2 fit value should exhibit some dependence upon the reflectivity values. This dependence is most visible when considering the Tile-Air Top-Bottom reflectivity. A minimum of the χ^2 value is clearly reached for a reflectivity of 0.92. The remaining interfaces account for a smaller fraction of the photon reflections and as such a minimum in the χ^2 value is not easily visible. However, an increased density of reflectivity parameter combinations which yield values of $\chi^2 < 0.2$ does appear for each of the reflection types.

All of the χ^2 values shown in Figures 7.8 and 7.9 correspond to reflectivity combinations from Table 7.2 assuming the maximum Fibre Core-Cladding (COCCUT) and Fibre Cladding-Optical Glue (CLTCUT) values of 0.999 and 0.990, respectively. A high degree of surface smoothness for the fibre core-cladding interface is expected because of the manufacturing technique [41]. Initial predictions of the light yield uniformity for the smaller values of $COCCUT = 0.995$ and $CLTCUT = 0.985$ were in poor agreement with the measured result. More specifically the light yield was underestimated compared to the observed output for scan points away from the WLS fibre readout. Therefore the χ^2 values for

these reflectivity combinations have been omitted from the analysis.

Therefore to determine a range of reflectivity values which best describe the data a selection of parameter combinations was chosen which minimize the value of χ^2. Figure 7.9 demonstrates the the range of minimum χ^2 values. A selection of 9 reflectivity combinations which minimize χ^2 was chosen as those most likely to describe the three sigma fibre tile. The values of χ^2 for these 9 combinations satisfy $\chi^2 < 0.036$ and are shown as a function of reflectivity value in Figure 7.10.

The reflectivity combinations which satisfy the χ^2 cut have Tile-Air Top-Bottom reflectivities of either 0.90, 0.92, or 0.94. Two of the other three reflectivity types, the Air-Wrapping Material and Fibre Core- Painted Surface reflections, also demonstrate small χ^2 values but over a larger range of reflectivity values. The best agreement between Monte Carlo and data is achieved for reflectivity parameter combination 424 with a χ^2 value of 0.0270. Figure 7.11 shows the Monte Carlo photoelectron distribution for each of the 25 spatial bins which result from the application of the reflectivity parameters of combination 424. Table 7.4 lists the full set of reflectivity values for each combination in order of ascending χ^2 value. The values of the scintillation and WLS photon attenuation lengths were fixed at 380.0 cm and 360.0 cm, respectively.

Shown in Figure 7.12 is the Monte Carlo photoelectron output distribution as a function of the position across the scintillator face for reflectivity combination 424 which exhibited the lowest value of $\chi^2 = 0.0270$. Also shown for comparison is the measured result determined from the data. The Monte Carlo result was normalized to match the total number of data entries. Schematically shown above the plot is a cross-sectional view of the scintillator and the relative positions of

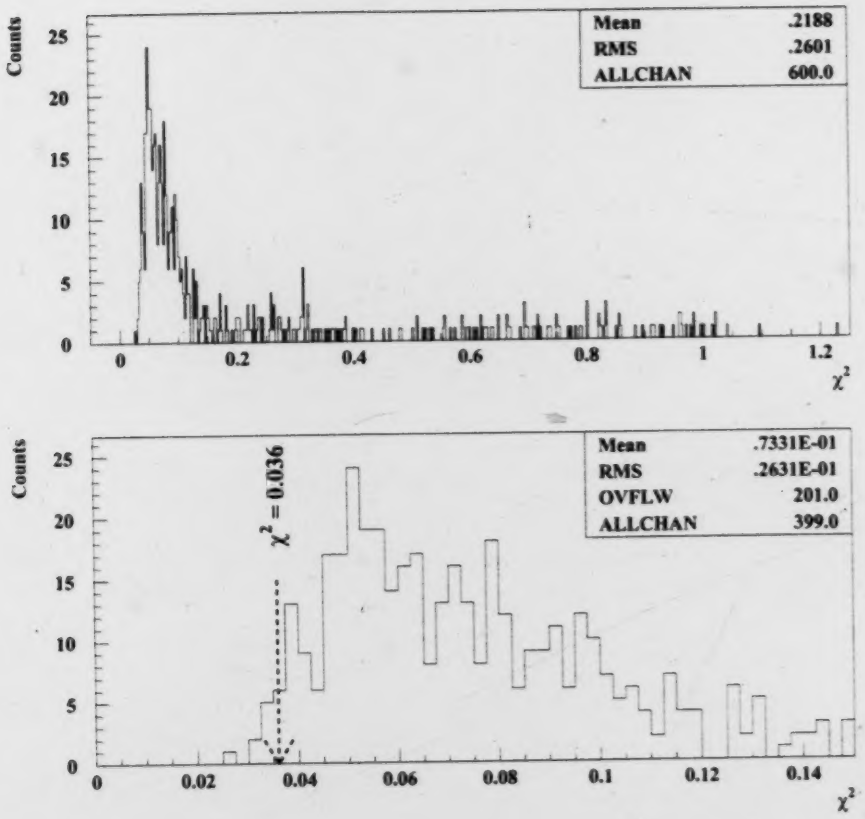

Figure 7.8: Distribution of Chi-Square values for all possible reflectivity values.

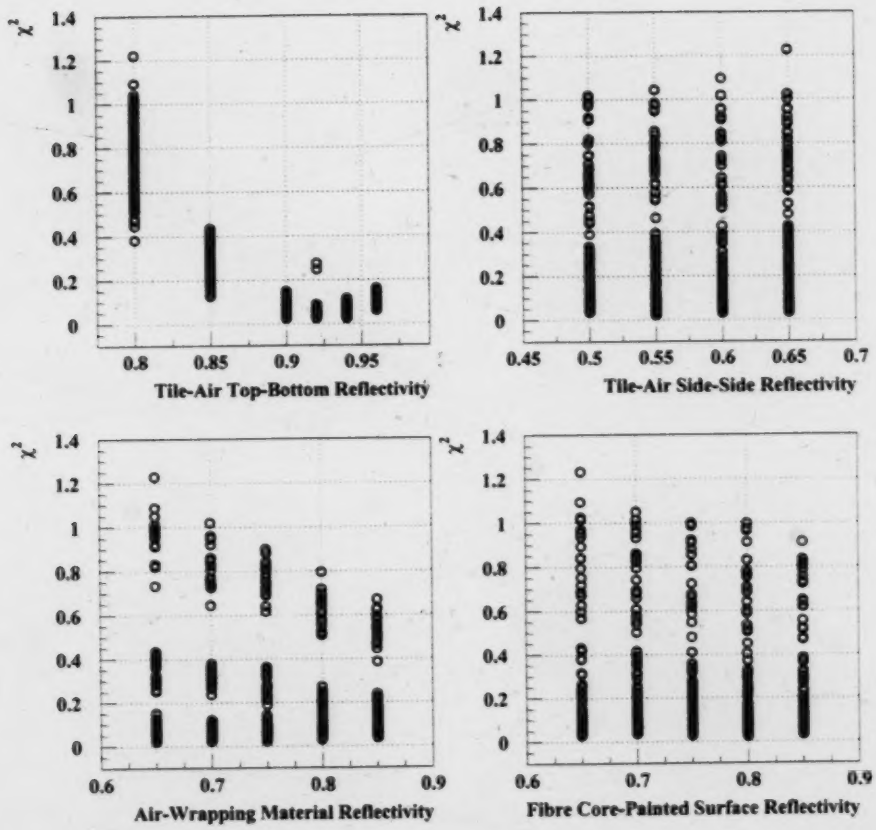

Figure 7.9: Chi-Square variation as a function of reflectivity values for Tile-Air Top-Bottom (TATBCUT), Tile-Air Side-Side (TASSCUT), Air-Wrapping (AMCUT), and Core-Surface (COSCUT) reflectivities.

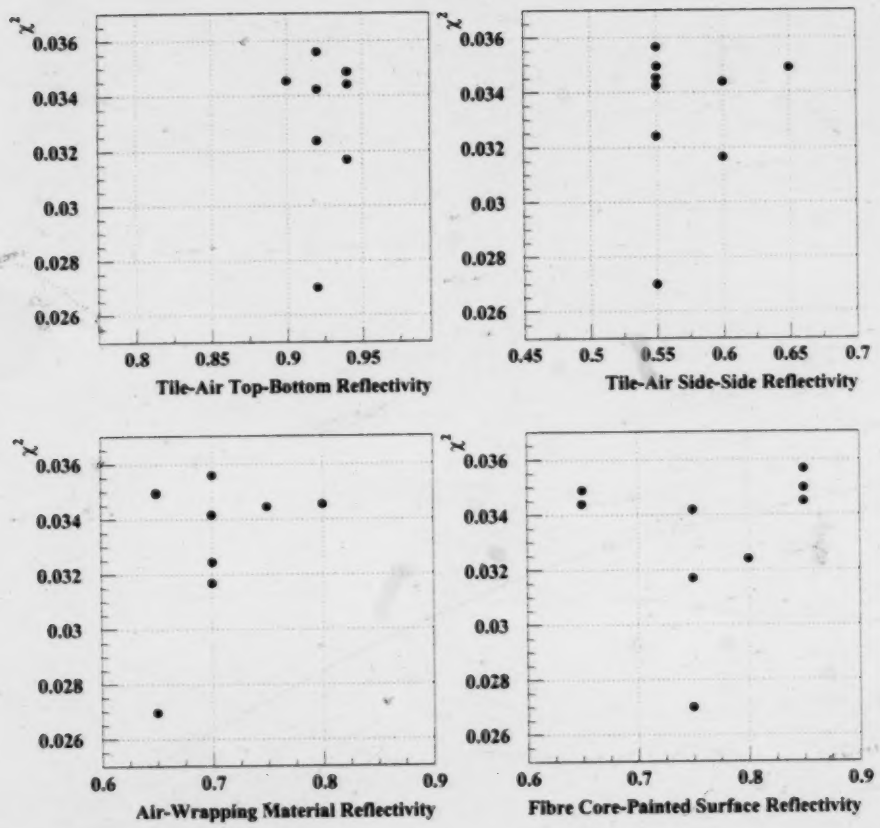

Figure 7.10: Chi-Square variation satisfying $\chi^2 < 0.036$ as a function of reflectivity values for Tile-Air Top-Bottom (TATBCUT), Tile-Air Side-Side (TASSCUT), Air-Wrapping (AMCUT), and Core-Surface (COSCUT) reflectivities.

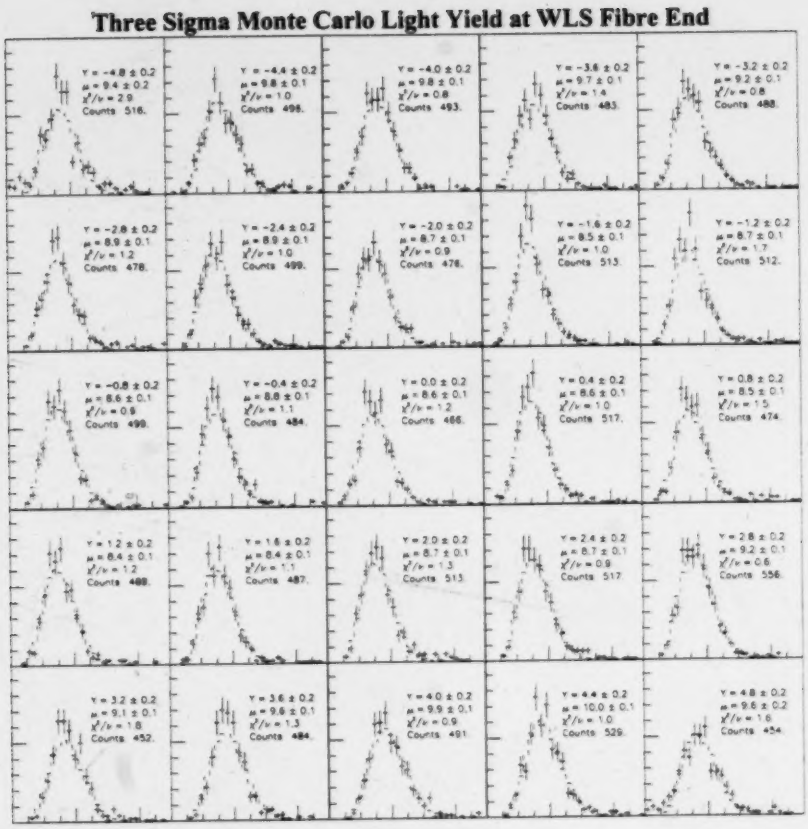

Figure 7.11: Simulated photoelectron yield at the WLS fibre end for each of the 25 spatial bins. The Monte Carlo result for reflectivity combination 424 was fitted with a Poisson distribution convoluted with a Gaussian to determine the mean number of photoelectrons.

COMBINATION	TATBCUT	TASSCUT	AMCUT	COSCUT	χ^2
424	0.92	0.55	0.65	0.75	0.0270
440	0.94	0.6	0.7	0.75	0.0316
496	0.92	0.55	0.7	0.8	0.0324
436	0.92	0.55	0.7	0.75	0.0342
332	0.94	0.6	0.75	0.65	0.0344
282	0.9	0.55	0.8	0.85	0.0346
305	0.94	0.55	0.65	0.65	0.0349
551	0.94	0.65	0.65	0.85	0.0349
556	0.92	0.55	0.7	0.85	0.0357

Table 7.4: Reflectivity value combinations yielding the minimum χ^2 values satisfying $\chi^2 < 0.036$. Reflectivity values are given for the Tile-Air Top-Bottom (TATBCUT), Tile-Air Side-Side (TASSCUT), Air-Wrapping (AMCUT), and Fibre Core-Reflective Surface (CORSCUT). All combinations have Fibre Core-Cladding (COCCUT) and Fibre Cladding-Optical Glue (CLTCUT) reflectivities of 0.999 and 0.990, respectively.

the WLS fibres. As expected there is an increased photoelectron output near the positions of the fibres at $y = \pm 4.45$ cm. There is good agreement between the Monte Carlo and measured results.

Figure 7.13 compares the Monte Carlo and measured results for the next three best reflectivity combinations which yield values of $\chi^2 < 0.0343$. There is good agreement between the simulation and data results even for these values with increased χ^2.

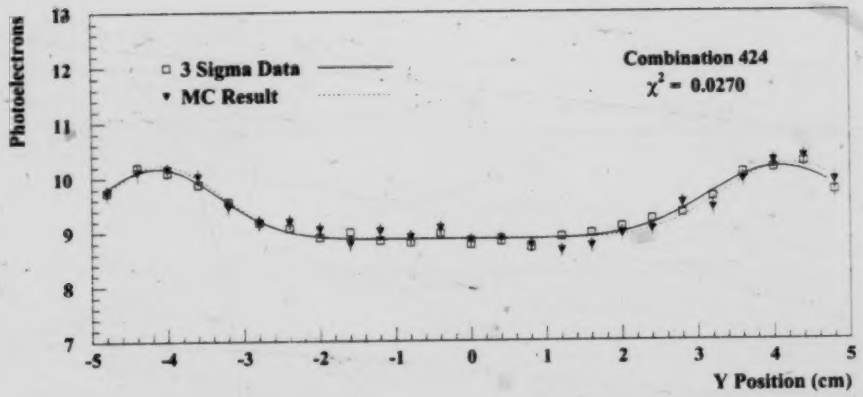

Figure 7.12: Comparison of the Monte Carlo and measured light yield of the 3 Sigma Prototype scintillating tile-WLS fibre combination as a function of position across the face of the scintillator for parameter combination 424. The scan region overlaps the WLS fibres at positions $y = \pm 4.45$ cm.

Photon Absorption and Attenuation Effects

It is instructive to examine in more detail the values of some of the quantities which are recorded as part of the simulation. Such variables include the pathlength travelled by the photons, as well as the number of reflections at each surface. Figure 7.14 shows the pathlengths for both scintillation and WLS photons. Included for each photon type are the pathlength distributions assuming each surface is perfectly reflective and with no losses due to attenuation. The expected photon pathlength which results from the application of the reflectivity cuts from combination 424 as listed in Table 7.4, as well for realistic attenuation lengths of 380.0 cm and 360.0 cm for the scintillation and WLS photons, respectively, is also

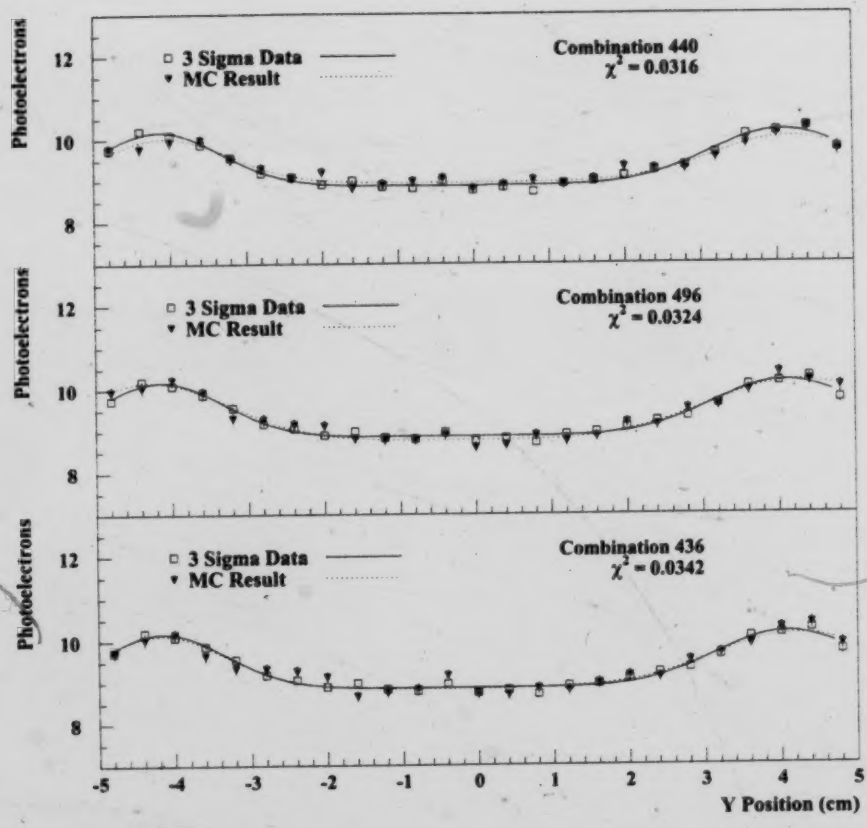

Figure 7.13: Comparison of the Monte Carlo and measured light yield for three of the reflectivity combinations with $\chi^2 < 0.0343$.

shown.

Both the scintillation and WLS photon pathlength distributions are marked by a series of peaks which decrease in amplitude as the pathlength progresses. These peaks in general result from the increased number of scintillation photon absorptions at various lengths along the WLS fibre due to the choice of scan region across the face of the scintillator. The primary scintillation photon pathlength peak represents photons which have been absorbed within the WLS fibre before the photon has traversed a distance slightly greater than the tile width of 10 cm.

To understand the origin of the peaks of the WLS photon pathlength distribution consider Figure 7.15 which displays the the distribution of values recorded for the distance from the scintillation photon absorption position along the fibre layout to the end of the fibre where the photomultiplier would be situated. The top figure represents all absorbed scintillation photons while the bottom figure represents only the scintillation photons whose secondary WLS photons survive to the photomultiplier position. The embedded length of each WLS fibre is 32.8 cm. Including a 1.0 cm extension beyond the boundary of the scintillator the total fibre length is approximately 33 cm. The scan region shown in Figure 7.2 covers the entire width of the scintillator from -5.0 cm to +5.0 cm in the y-direction and overlaps the wavelength shifting fibres at distances of $\pm$4.5 cm from the center of the tile. Due to the increased geometric acceptance in these regions, as expected there is an increased number of scintillation photon absorptions at these positions corresponding to distances of approximately 6.0 cm and 22 cm from the fibre readout end. The width of each peak is approximately 4.0 cm and corresponds to the width of the scan region in the x-direction. Outside of the two peak regions the values of the absorption location are evenly distributed with the exception of the fibre arc sections where there is a very slight decline in the number of absorptions.

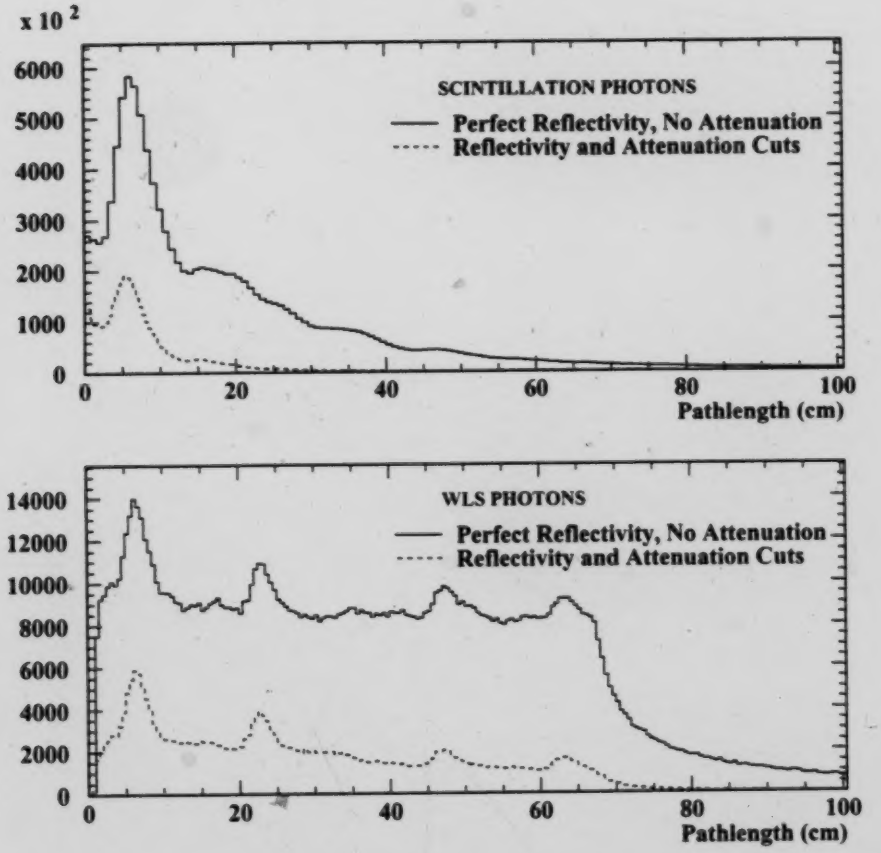

Figure 7.14: Pathlength of the scintillation and WLS (WLS) photons assuming perfect surface reflectivities and infinite attenuation length, as well as for realistic reflectivities and attenuation lengths corresponding to parameter combination 424.

This can be attributed to the smaller geometric acceptance at the fibre arc sections for photons originating in the central scan region compared to the straight fibre sections near the tile perimeter. The amplitude of the two scintillation photon absorption distance peaks are almost equal as expected.

The bottom plot in Figure 7.15 is the distribution of distances to the photomultiplier from the scintillation photon absorption location for WLS photons which reach the end of the fibre. Both the cases of perfect reflectivity and infinite attenuation lengths, as well as realistic values of reflectivity and attenuation for parameter combination 424 are shown. The difference in peak heights at distances of 6.0 cm 22.0 cm for this distribution is due to the loss of photons which are unable to propagate through the fibre arc sections without escaping as the probability for a photon to survive transmission though a 90° bend is high, but not 100%. A full discussion of transmission losses through bent fibres is given in Appendix A. Furthermore, WLS photons which originate inside any of the fibre arc sections also appear to experience a small reduction in the trapping efficiency compared to photons emitted in straight fibre sections due to the curvature of the fibre, again resulting in a slight decline in the number of photons which reach the fibre end from these regions.

With an understanding of Figure 7.15 the peaks observed in the photon pathlength distributions of Figure 7.14 can be explained in terms of the WLS photon origin within the fibre.

The first peak which occurs in the WLS photon pathlength distribution of Figure 7.14 represents scintillation photons absorbed approximately 6.9 cm from the fibre end which subsequently emit WLS photons in a direction pointing towards the photomultiplier. Therefore these photons travel a short distance

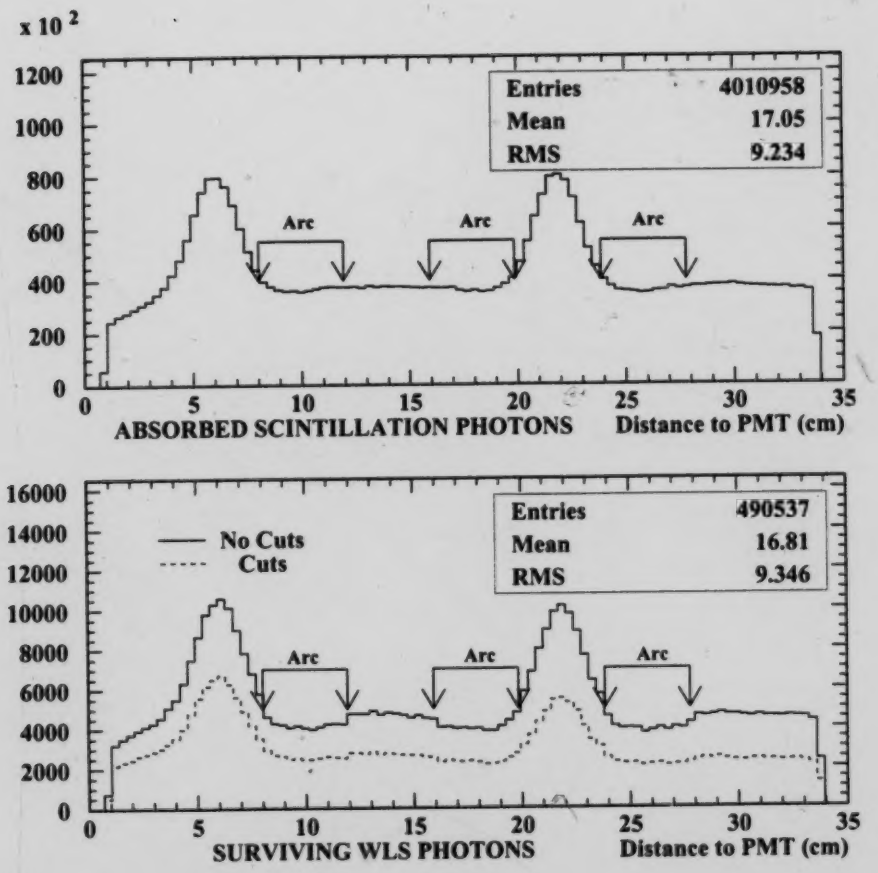

Figure 7.15: Distance from the readout end of the WLS fibre to the point of scintillation photon absorption for all photons (Top) and for surviving WLS photons (Bottom) assuming realistic reflectivities and attenuation lengths corresponding to parameter combination 424.

before arriving at the photomultiplier. If the emitted WLS photon is emitted in the direction away from the PMT then in order for the photon to eventually reach the PMT it must first reflect at the terminated end of the fibre. If successful in reaching the PMT the photon will travel a distance equivalent to approximately twice the embedded fibre length less the distance to the PMT at the time of emission. For photons originating approximately 6.9 cm from the PMT the total pathlength will be at the minimum 62 cm. These two man pathlength values of approximately 7.0 cm and 62 cm can be seen as the first and fourth peaks in the pathlength distribution for the WLS photons shown in Figure 7.14.

The second peak in the distribution of Figure 7.15 occurs at 21.9 cm, and is also visible in the WLS photon pathlength distribution. WLS photons emitted at this approximate position will travel distances of approximately 22 cm and 47 cm if emitted in either the forward or backward directions, respectively. The second and third peaks in the WLS photon pathlength distribution are visible at these distances. It should be noted that the values of the WLS photon pathlength in Figure 7.14 which are greater than 70 cm most likely represent photons propagating as skew rays, thereby traveling a total distance must greater that the distance from their emission point to th PMT along the fibre path.

Figure 7.16 shows the distribution of reflection counts recorded for the dominant reflection types experienced by the scintillation photons which are absorbed in the WLS fibre for both perfectly reflecting surfaces and the best fit result parameter combination 424. The distributions are shown on a log scale because of the large statistical Monte Carlo sample available. As expected the number of reflections occuring at the Tile-Air Top-Bottom interface decreases rapidly even for a high surface reflectivity of 0.92. A similar reduction in the number of reflections

at the Air-Wrapping Material and Fibre-Cladding-Tile interfaces, with reflectivities of 0.65 and 0.99 respectively, is also observed. As expected the largest rate of reduction in count occurs for the Tile-Air Side-Side reflections due to the poor surface reflectivity of 0.55. Reflectivities of this magnitude are expected since this surface is susceptible to imperfections from the machining and polishing process.

Figure 7.17 similarly shows the distribution of reflections for WLS photons which survive to the end of the fibre at the Fibre Core-Cladding and Fibre Cladding-Optical Glue interfaces for both perfectly reflecting surfaces and the case for reflectivity parameter combination 424. During propagation down the fibre the secondary photons will typically undergo many reflections and as such will fail to reach the end of the WLS fibre even with a high reflectivity value of 0.999. The number of reflections at the Fibre Cladding-Optical Glue interface also quickly reduce due to the reflection probability of 0.99 for combination 424.

7.5.2 Photoelectron Output

One of the important aims of the simulation is to provide an accurate estimate of the number of photoelectrons expected for a given configuration of scintillator with WLS fibre readout. Good agreement between the Monte Carlo and measured results was achieved when examining the expected light yield uniformity across the face of the scintillator-fibre detector. The determination of the average light yield for the entire scan region utilizes the same method as was already successfully applied to the light yield uniformity studies of Section 7.5.1.

The calculation of the average number of photoelectrons expected from the Monte Carlo required the fitting of the simulated output with a Poisson distribution convoluted with a Gaussian as given in equation 7.2. Since the fitting

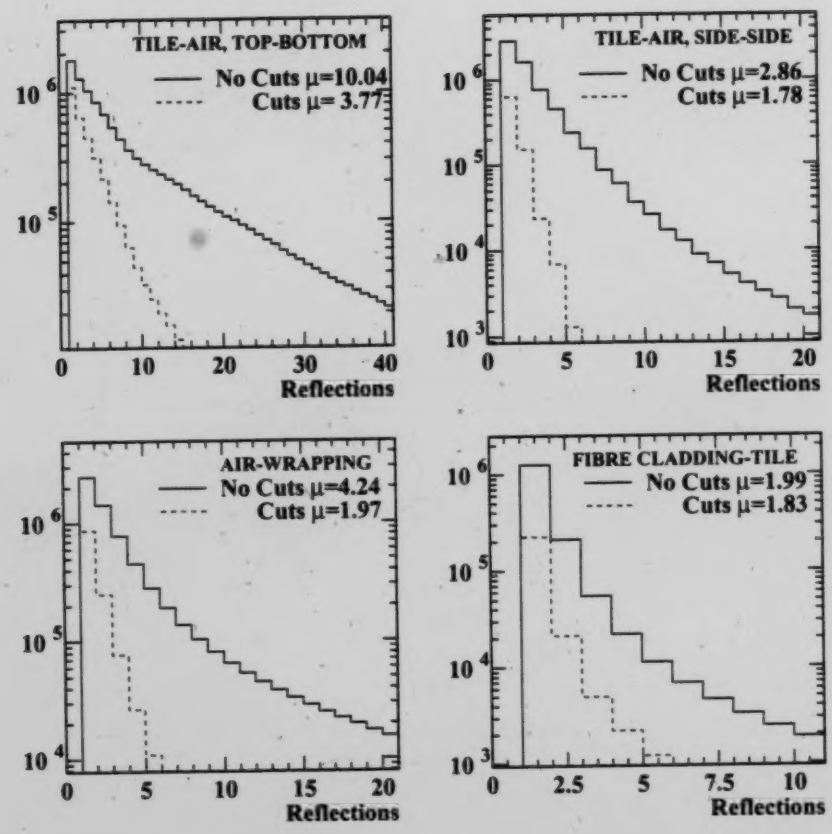

Figure 7.16: Number of reflections experienced by primary scintillation photons at the Tile-Air Top-Bottom, Tile-Air Side-Side, Air-Wrapping, and Fibre-Tile interfaces for both perfectly reflective and realistic non-perfectly reflecting surfaces as specified for combination 424.

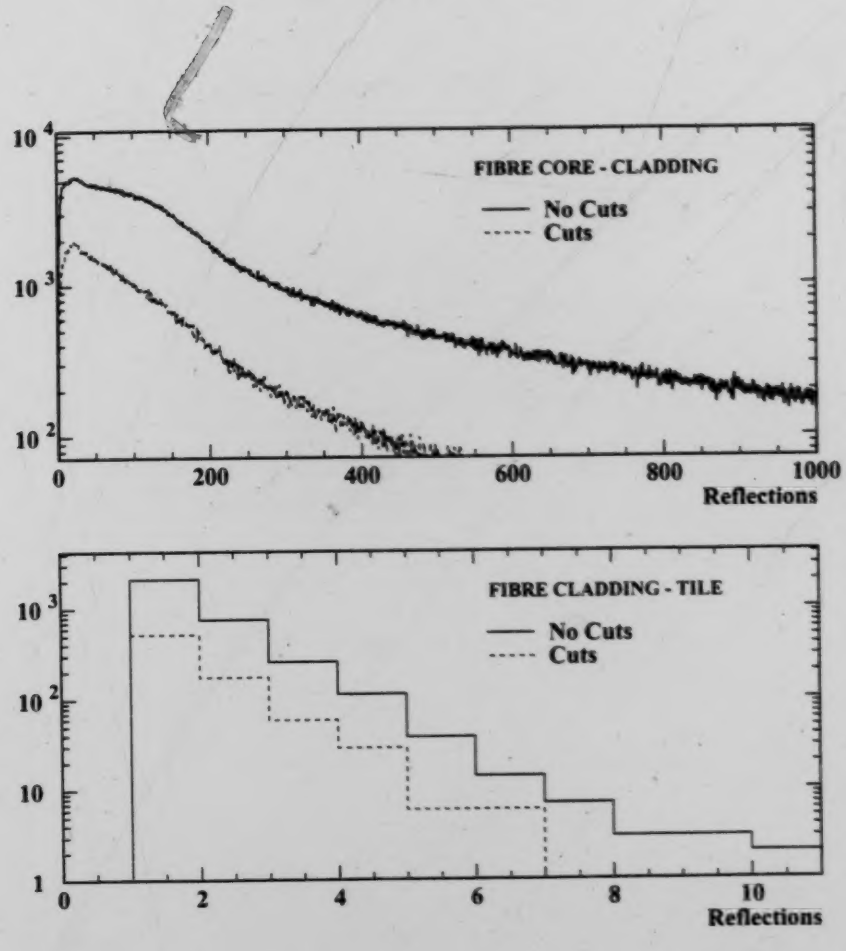

Figure 7.17: Number of reflections experienced by WLS photons at the Fibre Core-Cladding, and Fibre Cladding-Scintillator interfaces for both perfectly reflective and realistic non-perfectly reflecting surfaces as specified for combination 424. The mean number of reflections μ of each type is also given for both cases.

procedure was first carried out to find the mean number of photoelectrons at the end of the WLS fibre it was necessary to fit the results which best agreed with the measured light yield uniformity measurements and yielded the smallest chi-square value. The best match between Monte Carlo and data was from reflectivity combination 424 as listed in Table 7.4.

In the same fashion as that used in the uniformity studies the values of the mean number of photoelectrons and histogram amplitude, $PARAM(1)$ and $PARAM(3)$, were given initial values and allowed to vary during the fitting procedure. All six remaining parameters were fixed with the value of the Gaussian single photoelectron distribution σ_1 adjusted so as to yield a fit with a good χ^2/ν value. A non-zero value of the pedestal $PARAM(7)$ was also given when necessary to provide for any distribution offset from the origin.

Since the quality and specifications of the connector system which bridged the WLS and optical fibres was unknown the fitting procedure was used to first determine the mean number of photoelectrons which would be present at the end of the WLS fibre. Once this value is known, a variety of connectors can be easily convoluted with the result to determine an estimate of the expected number of photoelectrons emitted at the photocathode. A more rigorous analysis is then performed by integrating a specific connector design with the reflectivity analysis cuts.

Average Light Yield

Figure 7.18 shows the distribution of photoelectrons expected at the end of the WLS fibre from the Monte Carlo analysis. The Monte Carlo distribution was fitted with a Poisson distribution convoluted with a Gaussian of $\sigma = 0.13$ photoelectrons

to determine the mean number of photoelectrons as $\overline{NPE}_{WLS} = 39.8 \pm 0.1$. The fit was performed over a range extending to 65 photoelectrons, yielding a reduced chi-square fit of 1.68.

For comparison the measured ADC distribution for the three sigma tile is shown in Figure 7.3. A similar fitting procedure yielded a mean photoelectron count of $\overline{NPE}_{Measured} = 9.41 \pm 0.03$.

Following the determination of the Monte Carlo value for the number of photoelectrons at the end of the WLS fibre the effects of the connector which couples to the optical fibre must now be included. Once included, a measure of the number of photoelectrons emitted at the photocathode can be predicted and compared to the measured value.

Rather than directly compute the resulting photoelectron yield two methods will be used to isolate a range of reflectivity and connector transmission factor values which equate the Monte Carlo and measured values.

The first will use a convolution of the three sigma Monte Carlo results with the output of the separate standalone connector simulations discussed in Appendix B to compute a range of possible connector transmission factor $T_{Connector}$ and fibre surface smoothness values T_{Smooth} which bring the Monte Carlo result into agreement with the data.

The second method will incorporate each possible connector design explicitly into the three sigma fibre analysis procedure but for only the reflectivity parameter combination 424 which best simulated the measured light yield uniformity as discussed in Section 7.5.1. In addition to the previously determined mean number of photoelectrons at the end of the WLS fibre this analysis will also yield a value for the number of photoelectrons emitted at the photocathode for each

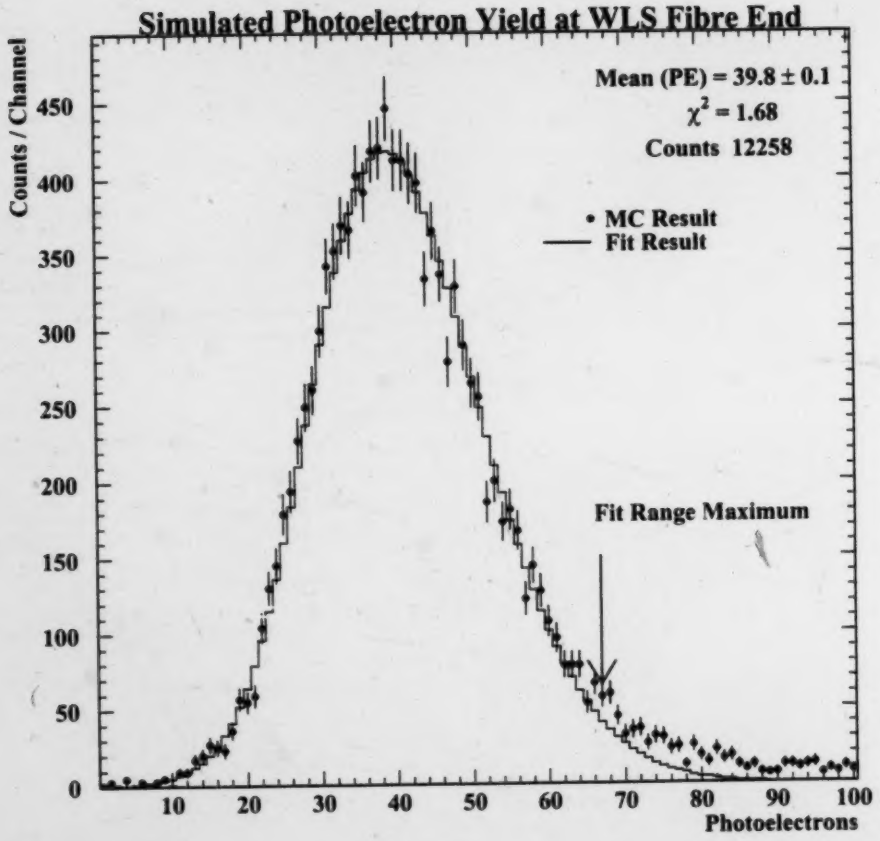

Figure 7.18: Simulated photoelectron yield at the WLS fibre end. The Monte Carlo result was fitted with a Poisson distribution convoluted with a Gaussian to determine the mean number of photoelectrons.

connector type. From this value a second range of fibre surface smoothness values T_{Smooth} which also bring the Monte Carlo and measured results into agreement will be determined.

The two ranges of T_{Smooth} values will be compared to yield a selection of connector geometries which allow the measured average photoelectron output to be fitted to the Monte Carlo.

Simple Three Sigma Fibre-Connector Simulation

The first stage of Monte Carlo analysis determined the mean number of photoelectrons expected at the end of the WLS fibre $\overline{NPE}_{WLS} = 39.8 \pm 0.1$. The extension of this value to equal the measured photoelectron output $\overline{NPE}_{Measured} = 9.41 \pm 0.03$ using the separate connector simulation can be characterized by the relation

$$\overline{NPE}_{Measured} = \overline{NPE}_{WLS} \cdot T_{Connector} \cdot T_{Geom} \cdot T_{Att} \cdot T^3_{Smooth} \qquad (7.13)$$

where $T_{Connector}$ is the connector transmission factor value, T_{Geom} is the fraction of photons surviving through the connector which are geometrically accepted and will propagate down the optical fibre, and T_{Atten} is the fraction of photons which are not lost due to attenuation while propagating down the optical fibre. The value of the wavelength shifting and optical fibre end surface smoothness T_{Smooth} is included to the third power since any WLS photon must pass through the end surface of the WLS fibre and both end surfaces of the optical fibre which couples to the photomultiplier. The quality of the surface polish determines the fraction of photons which will be transmitted. Although differences in polishing technique may cause T_{Smooth} to assume a wide range of values the results of the light yield

uniformity study of Section 7.5.1 can help pinpoint an appropriate range. From the reflectivities recorded as part of the Monte Carlo simulation the value of T_{Smooth} is related to the reflectivity of the fibre core-painted surface interface by the relation

$$T_{Smooth} = \frac{CORSCUT}{R_{Paint}} \tag{7.14}$$

where R_{Paint} is the reflectivity of the scintillator paint applied to the terminated end of the WLS fibre. This relation arises from the fact that in order to undergo reflection from the paint the photon must first pass through the end face of the fibre which has been polished to a smoothness T_{Smooth}. Therefore the overall reflectivity of the fibre core-painted surface interface is the product of the inherent paint reflectivity R_{Paint} and the fibre face surface smoothness T_{Smooth}. From this relation equation 7.13 can be manipulated to solve for the value of the connector transmission factor $T_{Connector}$. Solving for $T_{Connector}$ yields

$$T_{Connector} = \frac{\overline{NPE}_{Measured}}{\overline{NPE}_{WLS}} \cdot \frac{R^3_{Paint}}{T_{Geom} \cdot T_{Att} \cdot (CORSCUT)^3} \tag{7.15}$$

From the reflectivity parameter combinations listed in Table 7.4 which produce the best agreement between the Monte Carlo and data for the light yield uniformity the mean value of the Fibre Core-Painted Surface reflectivity is given by

$$\overline{CORSCUT} = 0.77 \pm 0.02 \tag{7.16}$$

Substituting $\overline{CORSCUT}$ and the reflectivity of $R_{Paint} = 0.95 \pm 0.01$ for a typical scintillator paint such as Bicron BC−620 [29] into equation 7.14 gives an average fibre end smoothness value of $T_{Smooth} = 0.81 \pm 0.02$.

The mean values of T_{Geom} and T_{Att} were calculated from the connector studies carried out in Section B.1 and are given by

$$T_{Geom} = 0.74 \pm 0.03$$
$$T_{Att} = 0.926 \pm 0.001 \tag{7.17}$$

Substituting into equation 7.15 yields

$$T_{Connector} = 0.65 \pm 0.05 \tag{7.18}$$

as the range of possible transmission factors which equate the Monte Carlo and measured results for the number of photoelectrons emitted at the photocathode. This range of transmission values encompasses several of the connector configurations listed in Table B.1 and Table B.2. Specifically for the optical grease connector the transmission factors are in agreement for connector gap sizes ranging from 0.050 cm to 0.100 cm with possible fibre misalignments ranging from 0.000 cm to 0.010 cm.

Therefore for connectors with transmission factors $T_{Connector} = 0.65 \pm 0.05$ and a fibre surface smoothness of $T_{Smooth} = 0.81 \pm 0.02$ the mean number of predicted photoelectrons emitted at the photocathode is equal to the measured value $\overline{NPE}_{Measured}$.

This initial selection of connectors must now be validated by the results obtained for the full Monte Carlo analysis in which the photons are explicitly transmitted through the connector.

Full Three Sigma Fibre-Connector Simulation

The output of the three sigma Monte Carlo simulation was reanalysed using the reflectivity cuts of combination 424 which yielded the best agreement between the

Monte Carlo and data light yield uniformity results. Each of the 24 optical grease connector arrangements in Table B.1 were explicitly simulated in conjunction with the analysis by tracking the WLS photons from the end of the fibre, through the connector, and down the optical fibre to the photomultiplier tube.

By including the connector directly into the simulation the relation between the measured number of photoelectrons $\overline{NPE}_{Measured}$ and the expected number from Monte Carlo at the end of the optical fibre $\overline{NPE}_{Optic}$ simplifies to a dependence upon only a single variable. This quantity is the surface quality or smoothness T_{Smooth} of both the WLS and optical cut fibre ends. The expected and measured light yield are therefore related by the equation

$$\overline{NPE}_{Measured} = \overline{NPE}_{Optical} \cdot T^3_{Smooth} \tag{7.19}$$

As mentioned previously each photon which propagates through the end of the WLS fibre, through the connector and down the optical fibre traverses three fibre end surfaces each of smoothness T_{Smooth}. In the simple three sigma fibre-connector analysis the value of T_{Smooth} was related to the average value of the Fibre Core-Painted Surface reflectivity $\overline{CORSCUT}$ with the final values taken for the best fit reflectivity combinations of Table 7.4. The values of T_{Smooth} and $\overline{CORSCUT}$ in the simple connector model were therefore equal to 0.81 ± 0.02 and 0.77 ± 0.02, respectively.

In the full three sigma fibre-connector simulation the mean number of Monte Carlo photoelectrons at the end of the optical fibre $\overline{NPE}_{Optic}$ is determined by fitting the distribution as discussed in Section 7.5.1. Assuming the relation between the values of $\overline{NPE}_{Measured}$ and $\overline{NPE}_{Optic}$ given in equation 7.19 the value for the fibre end smoothness T_{Smooth} has been computed for each of the 24 optical grease connectors listed in Table B.1. Table 7.5 lists the expected mean number of

photoelectrons at the end of the optical fibre $\overline{NPE}_{Optic}$ for each of the connector types, as well as the corresponding value of T_{Smooth} which would bring this light output into agreement with the measured result of $\overline{NPE}_{Measured} = 9.41 \pm 0.03$.

The tabulated values of T_{Smooth} of the full connector simulation which fall within the range of $T_{Smooth} = 0.81 \pm 0.02$ include to the same configurations selected by the simple connector model as the most likely to match the Monte Carlo light yield at the WLS fibre end $\overline{NPE}_{WLS}$ to the measured mean $\overline{NPE}_{Measured}$. The connectors which satisfy the condition on T_{Smooth} are typically 0.050 cm in connector gap size with misalignments ranging from 0.000 cm to 0.010 cm in length. These connector configurations include those predicted by the simple connector model.

Several other connectors with a large misalignment of 0.010 cm and a wide range of gap sizes ranging from 0.001 to 0.100 cm can also force the Monte Carlo into agreement with the measured average photoelectron output. The validity of such connector configurations is questionable because of the large misalignment of the fibre axes.

Therefore both the simple and full connector simulations find identically configured connectors as those which produce an agreement between the Monte Carlo and measured average light yield values.

Gap Size d (cm)	Misalignment ΔR (cm)	Light Yield $\overline{NPE}_{Optic} \pm 0.1$	Fibre Polish Quality T_{Smooth}
0.001	0.000	25.9	0.71
0.005	0.000	24.9	0.72
0.010	0.000	24.0	0.73
0.025	0.000	21.4	0.76
0.050	0.000	18.0	0.81
0.100	0.000	13.2	0.89
0.001	0.001	25.3	0.72
0.005	0.001	24.5	0.73
0.010	0.001	23.7	0.73
0.025	0.001	21.3	0.76
0.050	0.001	18.0	0.81
0.100	0.001	13.3	0.89
0.001	0.005	22.2	0.75
0.005	0.005	22.2	0.75
0.010	0.005	21.9	0.75
0.025	0.005	20.5	0.77
0.050	0.005	17.7	0.81
0.100	0.005	13.2	0.89
0.001	0.010	18.7	0.80
0.005	0.010	18.7	0.80
0.010	0.010	18.8	0.80
0.025	0.010	18.2	0.80
0.050	0.010	16.6	0.83
0.100	0.010	12.8	0.90

Table 7.5: Mean number of photoelectrons expected at the end of the optical fibre from Monte Carlo and the corresponding value of the fibre surface polish quality T_{Smooth} which is necessary for the Monte Carlo and measured light yield to be in agreement. The simple connector model predicts $T_{Smooth} = 0.79 \pm 0.03$.

CHAPTER 8

TE Scintillating Tile Performance

Studies of the three sigma fibre tile were important in generating the final design of the TE detector at OPAL. The simulation of the three sigma fibre tile, as discussed in Chapter 7, demonstrated the utility and validity of the GEANT-GUIDEIT combination as a descriptor for scintillator-fibre detectors.

In this chapter the simulation is extended to include the Tile 2 element of the TE detector in the OPAL environment at LEP. The sensitivity of the TE detector as a whole to minimum ionizing particles (MIPs) is determined. The performance of the Tile 2 element is also examined in terms of the average light yield from the passage of MIPs for both the entire tile segment and for a central scan region through the center of the tile. A comparison is made with the predicted light yield from simulation for MIPs incident upon a central scan region of the Tile 2 segment. The Monte Carlo is then used to predict the light yield uniformity across the scan region. The limited statistical sample available for MIPs incident upon the Tile 2 scan region at this time prevents an accurate comparison with Monte Carlo in this regards. Finally, the distribution of photon arrival times at the photomultiplier tube (PMT) is also simulated for a given range of reflectivity values and attenuation lengths, and subsequently compared to measurements performed for the TE Tile 2 element.

8.1 TE Scintillating Tiles

A detailed description of the TE detector at OPAL is given in Chapter 3 and elsewhere [7]. The approach taken to simulate the response of the Tile 2 element of TE was similar to that used in Chapter 7, and examined the light output from the passage of cosmic ray muons through a central scan region of the tile.

8.1.1 The TE Tile 2 Segment

The TE detector contains 48 separate Tile 2 elements in each endcap of OPAL. Figure 3.1 demonstrates the grouping of signals from two Tile 2 and two Tile 3 detector elements of the same azimuthal coverage, thereby providing 24 readout sectors in each endcap to match the OPAL trigger segmentation. Each Tile 2 section is 47.83 cm in length with inner and outer widths of 10.87 cm and 16.85 cm respectively, and inclined at an angle of 18° with respect to vertical in each endcap. From purely geometrical considerations and the spatial constraints of the endcap regions the values of the angular and spatial coverage for each element of TE can be determined. Table 8.1 lists the values of the angular acceptance and spatial coverage in both the radial and z coordinates for each of the TE Tile 1, Tile 2, and Tile 3 elements.

Each Tile 2 element was machined with grooves 1.1 mm wide and 2.2 mm deep on both top and bottom faces in the shape of a sinusoidal-like layout as shown in Figure 8.1. Two wavelength shifting (WLS) fibres of 117.0 cm length were embedded within each of the machined grooves and affixed with scintillator cement. The scan region of interest for Tile 2 was a 4.0 cm strip centered at the midway point of the tile at $y = 24.0$ cm and covered the full width of the

Quantity	Tile 1	Tile 2	Tile 3
Angular Acceptance $\theta_{min}(rad)$	0.294	0.378	0.521
Angular Acceptance $\theta_{max}(rad)$	0.393	0.521	0.624
Angular Acceptance $(\cos\theta_{min})$	0.957	0.929	0.867
Angular Acceptance $(\cos\theta_{max})$	0.924	0.868	0.811
Minimum Radius (cm)	65.0	83.7	129.4
Maximum Radius (cm)	89.0	129.2	172.5
Minimum Z-position (cm)	214.4	210.5	225.4
Maximum Z-position (cm)	214.4	225.3	239.4

Table 8.1: Values of the angular and spatial coverage provided by each of the three TE Tile elements in the OPAL environment. The values are derived from the geometrical constraints resulting in complete azimuthal coverage of the endcap region by TE.

scintillator tile in the x-direction. Figure 8.2 shows the scan region relative to the Tile 2 surface.

The WLS and optical fibres were coupled via high precision connectors as described in Chapter 3 with the light subsequently transported to the array of Electron Tubes 9902SKA photomultiplier tubes (PMT). The quantum efficiency as a function of photon wavelength for the 9902SKA PMT is given in Figure 8.3 [54]. The PMT used for TE was chosen to use a Rb Cs photocathode.

8.1.2 TE Tile 2 Description with GEANT-GUIDEIT

Figure 8.2 shows a GEANT drawing of the Tile 2 scintillator geometry and fibre layout. The performance of the Tile 2 was simulated for the passage of incident minimum ionizing cosmic ray muons. A total of 23 200 cosmic ray muon events were simulated using the GEANT-GUIDEIT software previously described

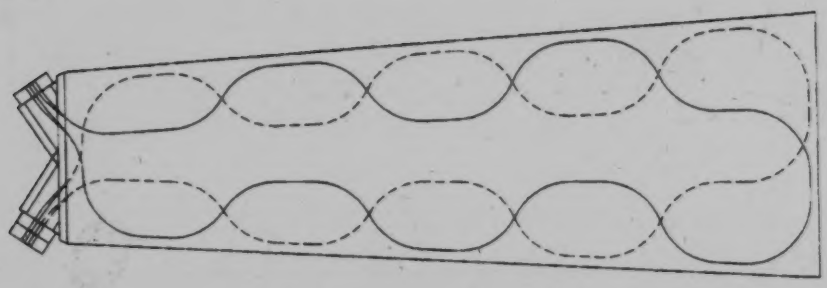

Figure 8.1: Sketch of the WLS fibre layout of the Tile 2 element of the TE detector.

in Chapter 7. The angular distribution of muons was restricted to normal incidence with respect to the tile surface for every point in the scan region. The energy of the incident muon was also required to be in excess of 250 MeV in order to classified as minimum ionizing.

To simulate the Tile 2 response the number of scintillation photons emitted per MeV of ionization energy deposited within the scintillator was approximated as 250 photons/MeV compared to the 500 photons/MeV used for the three sigma fibre tile analysis. The increased size of the scan region also necessitated the reduction in number of scintillation photons tracked. The scale factor to correctly match the $\approx$ 8 000 to 10 000 photons/MeV which in reality are emitted was applied to the predicted light yield at the end of the simulation on an event by event basis. The distribution of WLS photon wavelengths necessitated the application of the quantum efficiency associated with the Electron Tubes 9902SKA PMT Rb Cs photocathode to each of the photons which reach the end of the WLS fibre. Figure 8.3 shows the quantum efficiency as a function of wavelength for the Rb Cs photocathode of the 9902SKA PMT.

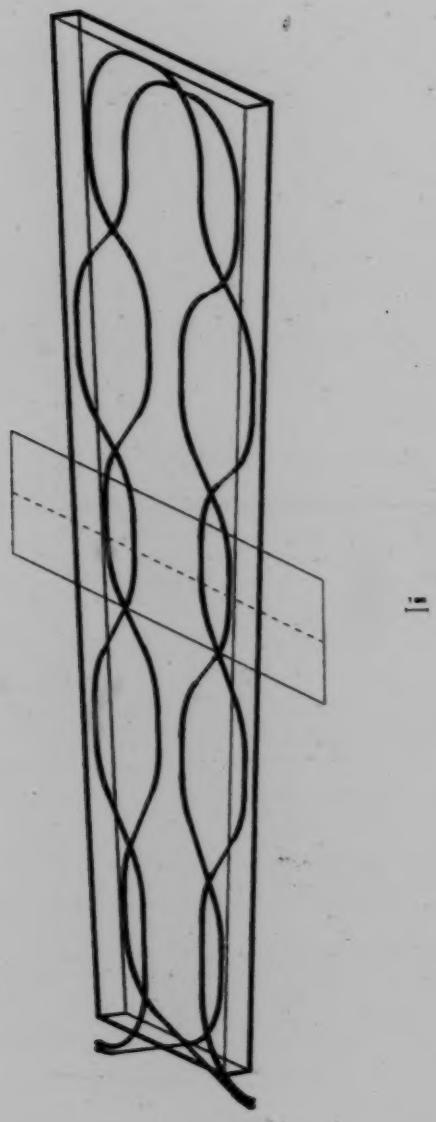

Figure 8.2: GEANT drawing of the TE Tile 2 geometry. The scan region examined with minimum ionizing particles is also shown.

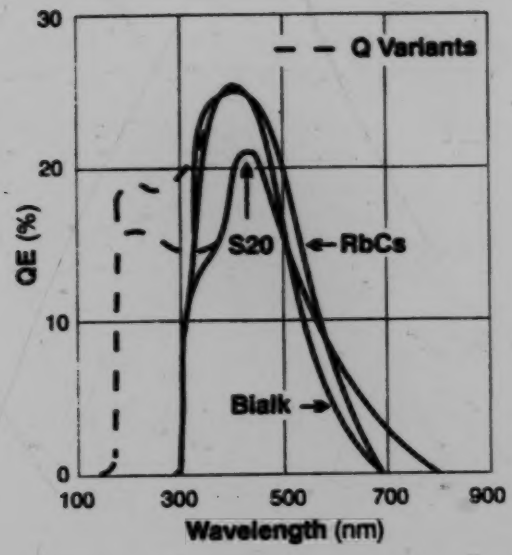

Figure 8.3: Quantum efficiency of the Electron Tubes photomultiplier tube photocathode as a function of wavelength. The PMTs used in TE utilize RbCs photocathode.

The scintillation photon tracking was performed using the GEANT routines until absorption occured within the WLS fibre. The generated secondary WLS photons were subsequently tracked through the fibre layout using the GUIDEIT ray tracing routines until the photons either escaped the fibre boundary or reached the readout end of the fibre which extends beyond the Tile 2 boundary.

All surfaces were again assumed to be perfectly reflecting and all photon attenuation lengths for the various materials were set to infinity. Based upon the experience gained from the three sigma fibre analysis of Chapter 7 a slightly reduced set of reflectivity combinations was used to analyze the Tile 2 Monte Carlo output. Table 8.2 lists the ranges of allowed surface reflectivity values which were

TATBCUT	TASSCUT	AMCUT	COCCUT	CLTCUT
0.800	0.500	0.650	0.999	0.990
0.850	0.550	0.700		
0.900	0.600	0.750		
0.920	0.650	0.800		
0.940		0.850		
0.960				

Table 8.2: Surface reflectivity values used in the Monte Carlo simulations of the Tile 2 geometry of TE. Reflections may occur at the Tile-Air Top-Bottom (TATBCUT), Tile-Air Side-Side (TASSCUT), Air-Wrapping (AMCUT), Fibre Core-Cladding (COCCUT), and Fibre Cladding-Optical Glue (CLTCUT) surfaces.

applied to the Tile 2 Monte Carlo.

8.2 TE Tile 2 Monte Carlo and Measured Results

The most obvious event types which provide isolated MIPs is heavy lepton pair production, including both muon and tau pairs. The direct production of $\mu^+ \mu^-$ from electron-positron collisions unfortunately only provides a small sample from which the sensitivity of the various TE tiles can be studied.

Measurement of the Tile 2 response to MIPs proceeded with the examination of $\mu^+ \mu^-$ events recorded from electron-positron collisions with the OPAL detector with center-of-mass collision energies ranging from from near the Z^0 resonance up to 183 GeV. By examining the Tile 2 response to tracks identified as muons it is possible to obtain a clean signal and distribution of ADC values which are MIPs and do not include any contamination from electromagnetic cascades

which may initiate in the approximately 2 radiation lengths of aluminum which forms the pressure bell directly in front of the TE detector.

Determination of the Tile 2 response required that only a single track be identified as passing through any given particular TE sector per event. This condition is necessary since the sensitivity to the passage of a MIP can only be studied for tile elements which are intersected by a single track. At the current time of operation, the inclusion of low multiplicity events [55] in the TE Tile 2 analysis does not significantly increase the event sample size.

8.2.1 MIP Sensitivity of TE

Over the course of TE operation during 1996 and 1997 a total of 1369 tracks associated with a muon from a $\mu^+ \mu^-$ event intersect an element of the TE detector, before the consideration of any track selection, and produce an observed ADC signal. This number reduces to approximately 657 charged tracks which pass through the Tile 2 sector. Of those tracks only 39 intersect the 4.0 cm wide strip across the full width of the Tile 2 and have a matching TE signal. Therefore, restricting the analysis to muon pair events will not provide adequate statistical sample to accurately determine the Tile 2 light yield uniformity, but will provide an average photoelectron output for comparison with Monte Carlo. An estimate of the Tile 2 sensitivity to MIPs can still therefore be performed.

Figure 8.4 shows the measured ADC distributions associated with the passage of a muon through all of TE (top), the Tile 2 sectors (middle) and the scan region of Tile 2 (bottom). For all three distributions the peak in the ADC distribution associated with the passage of the MIP is visible.

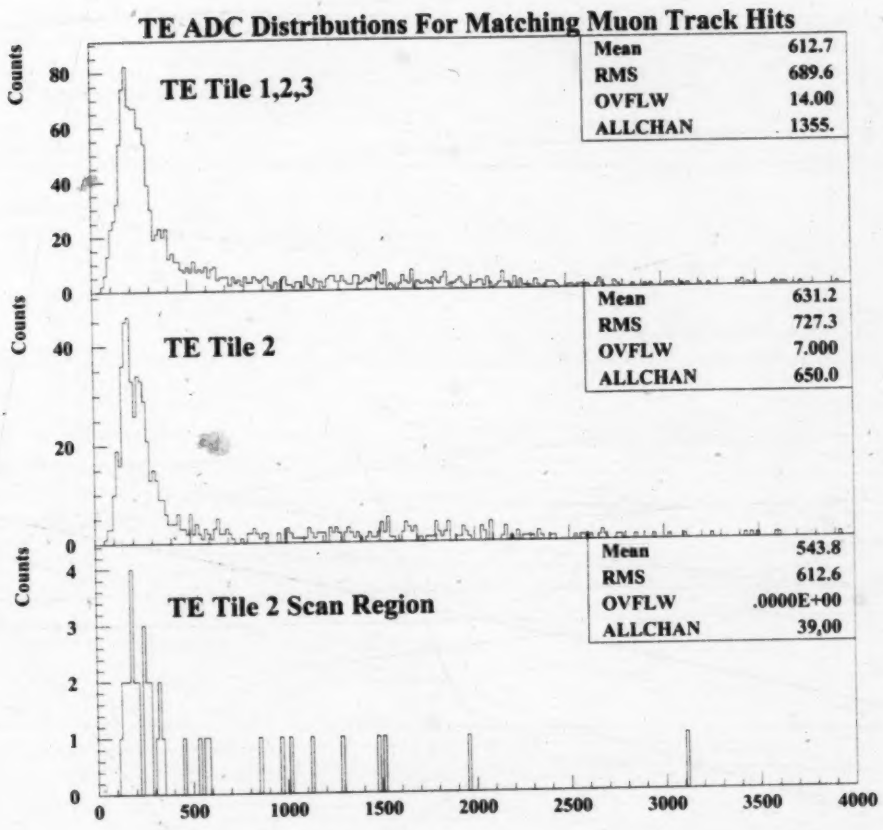

Figure 8.4: Observed TE ADC distribution in any TE Tile (top), TE Tile 2 (middle), and the TE Tile 2 scan region (bottom) from the passage of charged tracks from $\mu^+ \mu^-$ events in OPAL.

The examination of whether or not an ADC measurement in a particular TE Tile is associated with the passage of a charged track determines the MIP detection efficiency of the TE detector. Tracks from the $\mu^+ \mu^-$ events were selected for the efficiency analysis if the following criteria were satisfied:

- Only a single track is pointing to the TE Tile 2 sector under examination for the event.
- The track must possess a momentum $p > 10\ GeV/c$ in order to provide an accurate determination of the spatial hit position on the TE Tile 2 surface through which the muon passes. The momentum must also be less than 100 GeV/c from kinematic constraints.
- The ratio of the energy deposited in the electromagnetic calorimeter to the total track momentum, EE/CP, must be $\ll 1$ in order to veto electrons.
- The intersection point of the charged track with the TE Tile 2 or Tile 3 sector must not occur near the edges of the scintillator. Two cases of track intersection points required to be either 1.0 cm or 3.0 cm interior to the tile are considered. Track hits interior to the tile avoid any possible edge defects in the tiles due to manufacture or installation. Requiring hits interior to the tile also allows for any small errors in the track pointing position on the face of the tile.

Based upon the track selections a total 476 and 308 muon tracks produce associated TE Tile 2 hits for intersection points 1.0 cm and 3.0 cm interior from the tile edge, respectively. Similarly, a total of 309 and 224 muon tracks generate associated TE Tile 3 hits 1.0 cm and 3.0 cm respectively interior to the tile edge. Figures 8.5 and 8.6 show the measured MIP detection efficiencies for both the TE

Tile 2 and Tile 3. The sectors are numbered from 1 to 48 with the first 24 sectors situated in the left endcap region of OPAL ($\cos\theta < 0.$) while the remaining 24 sectors numbered 25 through 48, are situated in right endcap ($\cos\theta > 0$). Each sector contains four scintillating tiles; two each of the Tile 2 and Tile 3. A single PMT is used to readout the photons which reach the end of the WLS fibre embedded within each tile sector.

Figure 8.5 demonstrates the measured efficiencies of the TE Tile 2, Tile 3, and combined Tile $2+3$ sectors for charged tracks 1.0 cm interior to the tile perimeter. The MIP detection efficiencies for similar tracks 3.0 cm interior to the tile perimeter are shown in Figure 8.6.

The MIP detection efficiencies of the individual TE Tiles and the combined TE Tile $2+3$ sector are very high with the exception of several sectors. The detection efficiency also improves for several sectors with the requirement that the muon track be at least 3.0 cm interior to the tile. The poor detection efficiency of several sectors is believed to be associated with problems in the readout electronics. These problematic sectors are as a result omitted from the analysis of the average Tile 2 light yield.

The TE detector has therefore succeeded in achieving the design goal of efficient sensitivity to the passage of MIPS.

8.2.2 TE Tile 2 Average Light Yield

The average light yield of the TE Tile 2 sector is calculated and based upon the sample of muon pairs which satisfy the criteria specified above for the determination of the MIP detection efficiency. The muon tracks selected for the average

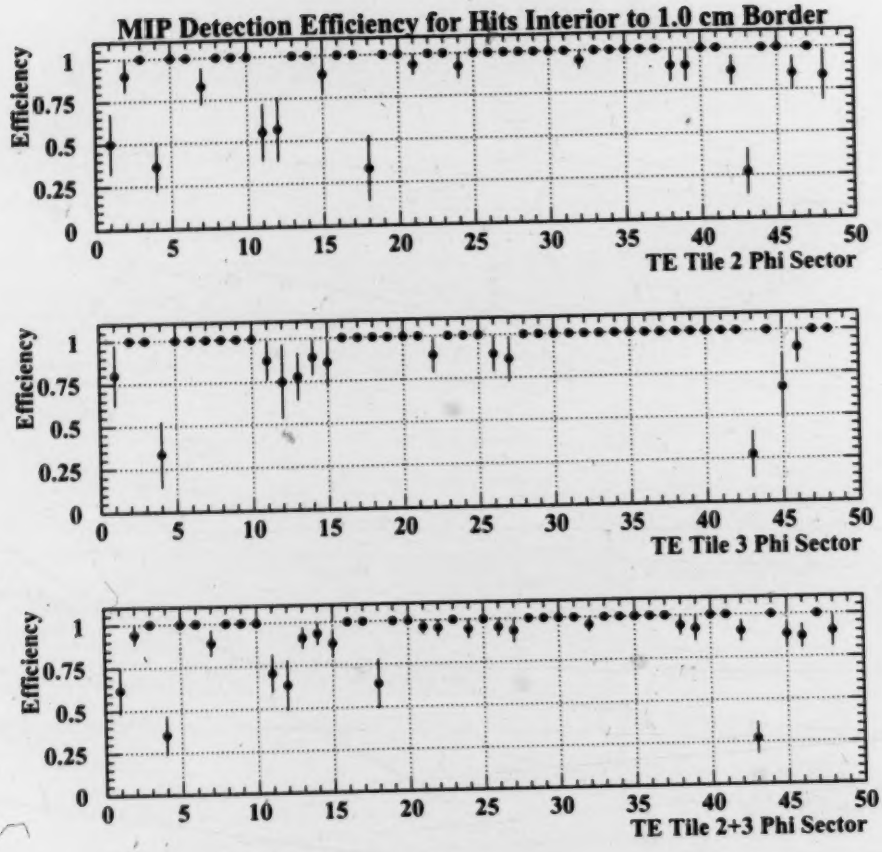

Figure 8.5: MIP detection efficiency of the TE Tile 2, Tile 3, and combined Tile 2+3 sectors for charged tracks 1.0 cm interior to the tile perimeter.

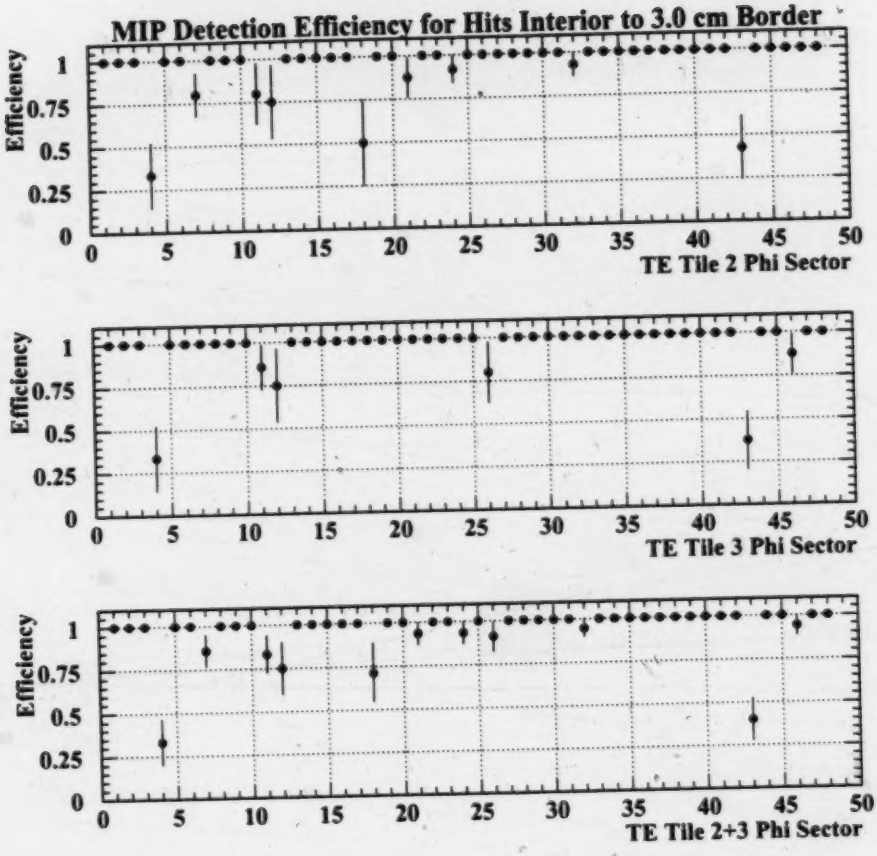

Figure 8.6: MIP detection efficiency of the TE Tile 2, Tile 3, and combined Tile 2+3 sectors for charged tracks 3.0 cm interior to the tile perimeter.

light yield measurement were required to be at least 1.0 cm interior to the tile perimeter.

The fitting procedure to calculate the average light yield follows the method described previously in Section 7.5.1 of Chapter 7 as part of the three sigma fibre tile analysis.

Figure 8.7 shows the measured ADC distribution for muon tracks incident upon the Tile 2 sectors which were determined to be highly efficient for detecting MIPs. The resulting value for the average light output corrected to normal incidence $\overline{NPE}_{Tile2}$ of Tile 2 is calculated to be 13 ± 2 photoelectrons. This result is consistent with a measurement of the average TE photoelectron output of 14 ± 2 [7].

The uncertainty in the value of $\overline{NPE}_{Tile2}$ was estimated through a simple examination of the light output variation as a function of possible fluctuations in the gain of the PMTs about the nominal value of 2×10^7, as well as possible variations in the amount of tube noise experienced by each TE PMTs. Although calibrated using LEDs gain variation and instability may arise from fluctuations in the electron multiplier section of the TE PMTs, possibly due to electron transit time differences or secondary emission factor nonuniformities over the PMT dynodes. Temperature changes may also have an effect on the gain, although expected to be small [30]. The fitting procedure used allows for variations in both the PMT gain and values of tube noise to be applied.

A more detailed and systematic study of the effects of gain instability and tube noise specific to the TE detector readout is therefore necessary to provide a better estimate of the mean photoelectron output and its uncertainty.

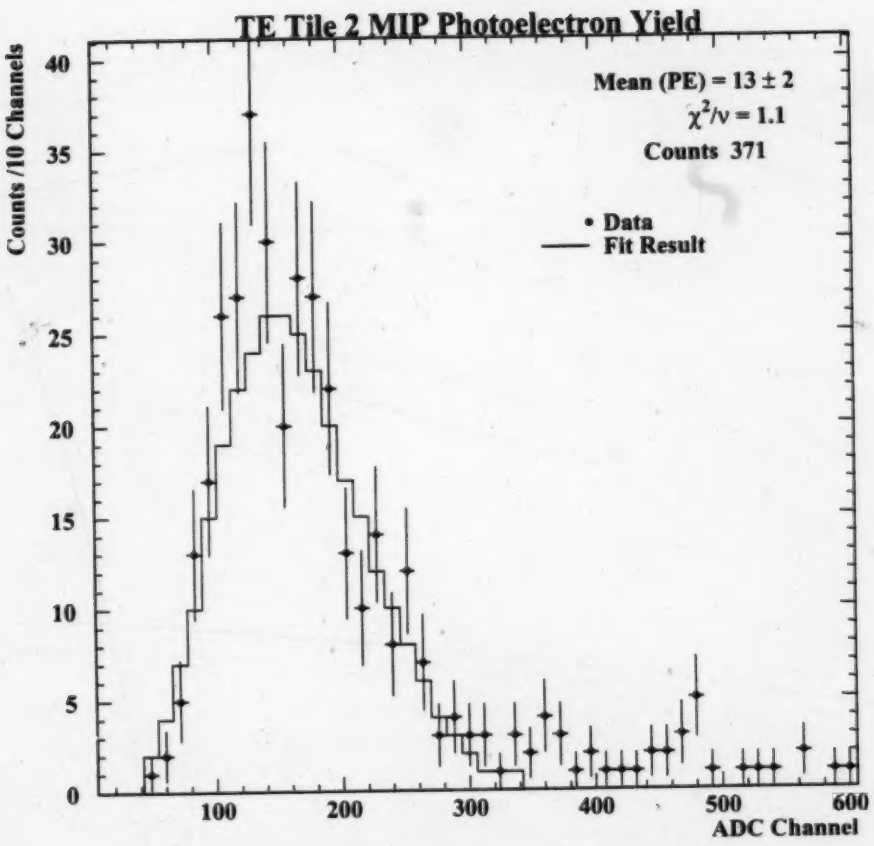

Figure 8.7: Average measured photoelectron output for the passage of MIPs from $\mu^+ \mu^-$ events through the TE Tile 2 sector.

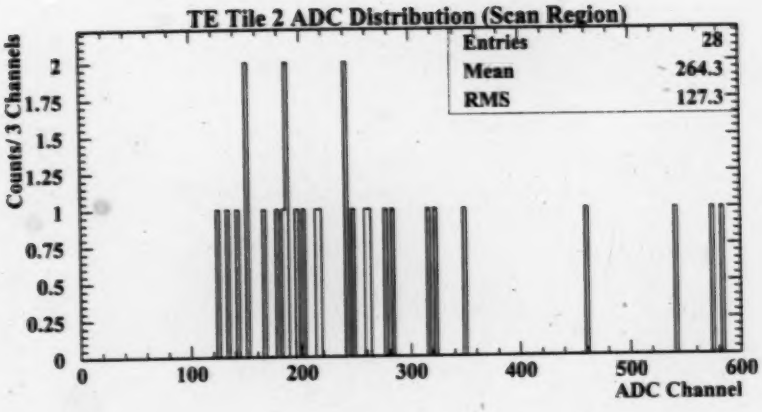

Figure 8.8: Average measured photoelectron output for the passage of MIPs from $\mu^+ \mu^-$ events through the central scan region of the TE Tile 2 sector. The mean light yield is estimated to be 15 ± 3 photoelectrons.

Figure 8.8 shows the measured ADC distribution associated with the passage of muons through the central scan region of Tile 2. The ADC values have also been corrected for normal incidence of the muon trajectory. A total of 28 muon tracks intersect the Tile 2 scan region and satisfy the track quality cuts. Prior to any selection only 39 tracks intersect the Tile 2 scan region. The mean photoelectron output for the central scan region $\overline{NPE}_{Scan}$ is calculated using equation 7.11 of Chapter 7 which relates the mean photoelectron value to the observed ADC mean. A slightly larger photoelectron yield of $\overline{NPE}_{Scan} = 15 \pm 3$ is estimated. The larger uncertainty is representative of the small number of muon tracks which intersect the scan region.

8.2.3 Tile 2 Monte Carlo Light Yield

The average Monte Carlo light yield for the three sigma fibre was predicted in Chapter 7 on the basis of the selection of an optimal set of reflectivity values which provided the best agreement between simulation and data for the light yield uniformity across the width of the scan region. For the TE Tile 2 the sample size of muon events is not large enough to permit the measurement of the light yield variation across the scan region, and therefore the surface reflectivities which best describe the Tile 2 are difficult to determine as accrurately as was done for the three sigma fibre tile. Therefore a direct comparison of the predicted light yield at the end of the optical fibre with that measured for Tile 2 is made.

Based upon the successful match between Monte Carlo and data for the three sigma fibre analysis it was decided to examine the predicted photoelectron yield at the end of the approximately 15.0 m optical fibre of Tile 2 using the optimal reflectivity values of Combination 424 given in Section 7.5.1 of Chapter 7. This was considered a reasonable choice due to the fact that the scintillator material of both TE and the three sigma tile was both BC-408.

Figure 8.9 shows the number of photons reaching the end of the optical fibre $NPE_{Optical}$ for combination 424 with reflectivities: Tile-Air Top-Bottom (TATBCUT) 0.92, Tile-Air Side-Side (TASSCUT) 0.55, and Air-Wrapping (AMCUT) 0.65. The reflectivity of the fibre core-cladding (COCCUT) interface of both the WLS and clear optical fibres was allowed to vary slightly in the Tile 2 Monte Carlo analysis about the base value of 0.999. This variation was performed due to the use of a different manufacturer (Kuraray [24]) of the WLS fibres for TE compared to those used for the three sigma fibre design (Bicron [23]). Although only very small variations in core-cladding reflectivity are believed the senstivity

of the predicted light yield to the value of reflectivity is apparent from the large number of reflections which the WLS photons will undergo at this interface, as shown previously in Figure 7.17.

The distribution shown in Figure 8.9 was determined assuming a value of 0.9985 for the fibre core-cladding reflectivity for both the WLS and optical fibres. The values of the scintillation and WLS photon attenuation lengths were again taken from the manufacturer's specfications, and set equal to 380.0 cm and 360.0 cm, respectively. A high quality connector with an optical grease gap size of 0.010 cm was also assumed.

The relationship between the measured Tile 2 average light yield of 15 ± 3 photoelectrons and the number of predicted photoelectrons at the end of the optical fibre was also used in Chapter 7 and is given by

$$\overline{NPE}_{Measured} = \overline{NPE}_{Optical} \cdot T^3_{Smooth} \tag{8.1}$$

where T_{Smooth} is the surface polish quality of the WLS and optical fibres.

A high fibre surface polish quality T_{Smooth} on the order of 0.80 to 0.85, a reasonable values from the final TE installation, brings the predicted and measured light yields into agreement.

The predictive power though of the Tile 2 Monte Carlo is again limited by the small statistical sample of muon tracks which prevented a comparison on the basis of the light yield uniformity. The abundance of Monte Carlo events will still permit a prediction on the light yield uniformity.

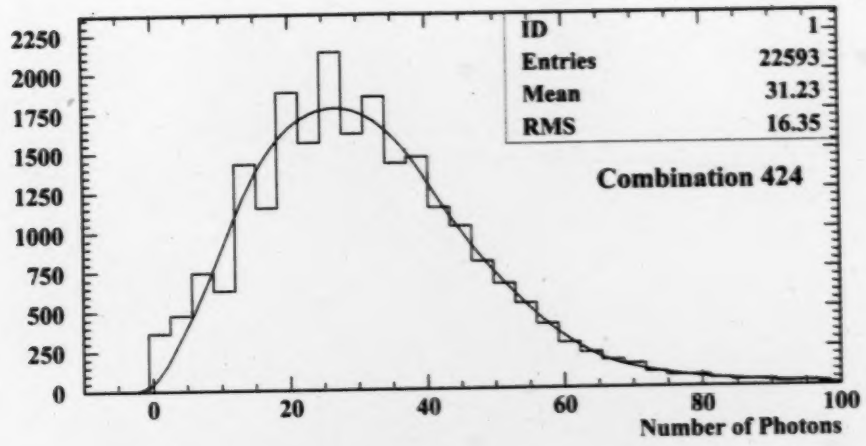

Figure 8.9: Monte Carlo prediction of the number of photoelectrons seen at the end of the optical fibre for reflectivity combination 424. Values of the reflectivities are: Tile-Air Top-Bottom (TATBCUT) 0.92, Tile-Air Side-Side (TASSCUT) 0.55, Air-Wrapping (AMCUT) 0.65, WLS fibre core-cladding (COCCUT) 0.9985, and cladding-optical glue (CLTCUT) 0.990. Attenuation lengths of 380.0 cm and 360.0 cm where applied for scintillation and WLS photons respectively.

8.2.4 TE Tile 2 Predicted Light Yield Uniformity

Shown in Figure 8.10 is the predicted light yield as a function of position across the scan region of TE Tile 2 for reflectivity combination 424. The scan region is shown for reference in Figure 8.2. The light yield uniformity has been normalized to the measured mean light output of approximately 15 ± 3 photoelectrons.

As previously observed with the three sigma fibre uniformity scan there is an enhanced light yield near the locations of the WLS fibres. For the Tile 2 scan region the WLS fibres are located at the approximate positions of $x = \pm 2.4$ cm

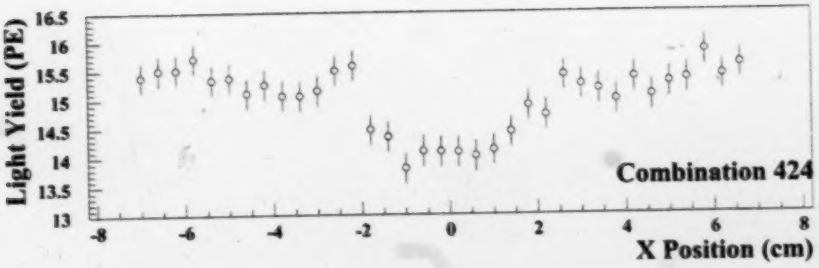

Figure 8.10: Monte Carlo prediction for the light yield uniformity across the scan region of the TE Tile 2 for reflectivity combination 424: Tile-Air Top-Bottom (TATBCUT) 0.92, Tile-Air Side-Side (TASSCUT) 0.55, Air-Wrapping (AMCUT) 0.65, and fibre core-cladding (COCCUT) 0.9985. Attenuation length of 380.0 cm and 360.0 cm for scintillation and WLS photons were assumed.

and $x = \pm 6.0$ cm relative to the center of the scan region. Although a comparison with data is not possible for the Tile 2 uniformity scan the successful agreement between Monte Carlo and data for the three sigma fibre scan of Chapter 7 is a clear indication of the validity of the variations shown in Figure 8.10.

8.2.5 Tile 2 Timing Characteristics

The main design goal of the TE detector was to provide timing information to the OPAL trigger with a good resolution in order to allow online identification of the bunch crossing time. An important aspect of the TE Tile simulations therefore is also to demonstrate the time structure of pulses recorded for the passage of a MIP through a TE scintillating tile.

Figure 8.11 [53] shows a raw signal recorded for the passage of a cosmic

ray muon through single TE Tile 2 sector. The top pulse is of the raw signal while the bottom pulse represents the raw signal after undergoing amplification and integration. The width of the timing gate generated by the Tile 2 signal was measured to be approximately 5 ns, corresponding to a pulse time jitter of $\approx$ 2 ns. Figure 8.12 demonstrates the simulated photon arrival time distribution with a similar resolution of $\approx$ 2 ns. The structure of both the measured and simulated pulses are a series of randomly distributed peaks which represent the emission of a small number of photoelectrons at the PMT photocathode. Variations in the distributions are expected because of the emission time associated with both the scintillator material and the WLS fibre, as well as due to the different pathlength travelled by each photon as it propagates to the PMT.

The good agreement between the Monte Carlo and measured photon arrival time distributions for the Tile 2 sector demonstrates the utility of the GEANT-GUIDEIT software to provide an accurate simulation of a wide variety of scintillator-WLS fibre arrangements.

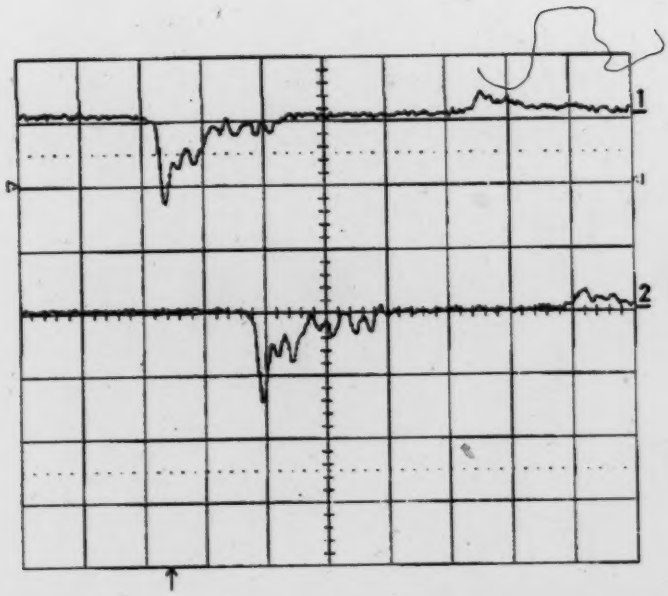

Figure 8.11: Raw pulse signal observed from the passage of cosmic rays for a production TE Tile 2 sector. Each division along the x and y axes represents 20 ns and 50 mV, respectively.

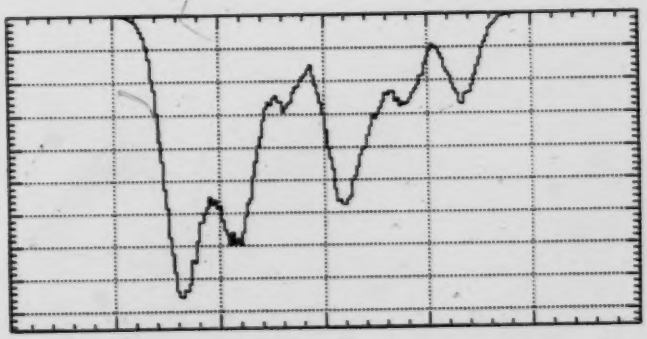

Figure 8.12: Monte Carlo light output as a function of time for the passage of a single cosmic ray through TE Tile 2 assuming a single photoelectron resolution of approximately 2 ns. Each large division on the x axis represents 10 ns. The vertical axis units are arbitrary and therefore indicates only relative amplitudes.

CHAPTER 9

Conclusion

A Monte Carlo simulation of scintillation detectors with wavelength shifting (WLS) fibre readout has been presented. The standard GEANT simulation software has been enhanced with the addition of routines which simulate the processes of scintillation and wavelength shifting. An interface between the GEANT and GUIDEIT simulation programs was constructed whereby scintillation and WLS photons are tracked in the framework of GEANT and GUIDEIT, respectively. The software interface was necessary to ensure the correct propagation of photons in the WLS fibre. Furthermore, the addition of torus segments to the available detector geometries of GUIDEIT permits the simulation of scintillation detectors with complex layouts of embedded WLS fibres.

The GUIDEIT program was first utilized to determine the spatial distribution of photons in the cross-section of a WLS fibre. Measurements performed using a high resolution CCD array were successfully modeled by the Monte Carlo. The observed distribution indicated an increased density of photons propagating as skew rays at radial positions near the outer radius of the WLS fibre core.

The successful simulation of photon propagation in WLS fibres was then applied to describe the response of the three sigma fibre prototype tile to the passage of minimum ionizing particles (MIPs). Measurements were made using a cosmic ray telescope. The Monte Carlo prediction of the photoelectron uniformity and average photoelectron output over a central region of the tile were in good

agreement with data. The surface reflectivity values which best described the three sigma fibre prototype were determined utilizing a chi-square minimization analysis. The optimal surface reflectivity values were subsequently used to predict a range of possible WLS-to-optical fibre connectors which brought Monte Carlo and data into agreement. A separate simulation of various connector configurations was also performed using the GEANT-GUIDEIT software.

The simulation was extended to describe the final design of the Tile Endcap (TE) Tile 2 sector of the OPAL detector. The Monte Carlo was compared with data obtained for MIPs from $\mu^+ \mu^-$ events in terms of the average photoelectron output and uniformity of response across the face of the TE Tile 2. The small event sample size limited the comparison of the Monte Carlo and data to the mean photoelectron output. Both the Monte Carlo and measured values were in agreement for realistic connector configurations and fibre surface polish qualities. A prediction of the photoelectron uniformity expected for the TE Tile 2 was made based upon the optimal surface reflectivity values determined for the three sigma fibre prototype tile. An increase in photoelectron output is predicted for MIPs intersecting the TE Tile 2 at locations near the embedded WLS fibres.

A comparison of the predicted and observed pulse shapes for the passage of a single MIP through the TE Tile 2 was also made. Both the Monte Carlo and data demonstrate a series of peaks corresponding to the varying arrival times of photons at the photocathode. In the future it is hoped an increased number of MIPs observed at OPAL will enable a measurement of the photoelectron uniformity of the TE Tile 2 which can be compared to Monte Carlo.

The good agreement between Monte Carlo and data obtained for the three

sigma prototype and TE Tile 2 sector demonstrate the success of the GEANT-GUIDEIT simulation software. The simulation can therefore be employed to predict the response of scintillator-WLS fibre detectors. WLS fibre readout of scintillating tiles is indeed a clearly novel technique for the efficient detection of MIPs.

Bibliography

[1] M.G. Albrow et. al., NIM A256(1987) 23.

[2] K. Ahmet et. al., NIM A305 (1991) 275-319.

[3] P.P. Allport et. al., NIM A324 (1993) 34.

[4] J.R. Carter et al., NIM A286 (1990) 99.

[5] O. Biebel et al., NIM A323 (1992) 169.

[6] H. Mes et al., NIM A265 (1988) 445.

[7] *Thin Scintillating Tiles with High Light Yield for the OPAL Endcap*, , B. Caron et. al., OPAL TN524, November 1997.

[8] J.D. Hobbs et al., NIM A325 (1993) 494.

[9] C. Beard et al., NIM A286 (1990) 117.

[10] S. Dado et al., NIM A252 (1986) 511.

[11] J. Allison et al., NIM A236 (1985) 284.

[12] G. Alexander et al., Z. Phys. C52 (1991) 175.

[13] B.E. Anderson et al., IEEE Trans. On Nuclear Science, 41 (1994) 845.

[14] *The Trigger System of the OPAL Experiment at LEP*, CERN-PPE91-32.

[15] *The Pretrigger System of the OPAL Experiment at LEP*, CERN-PPE93-48.

[16] *GOPAL Simulation Software*, J. Allison et al., NIM A317 (1992) 47.

[17] *GEANT Detector Description and Simulation Tool*, CERN Program Library Long Writeup W5013 (1994).

[18] *Proposal to Install Scintillating Tiles in the OPAL Endcap*, OPAL Collaboration, CERN-LEPC/94-09, 1994.

[19] *Aspects of the Presampler Endcap Detector in the Context of a Possible Upgrade to the OPAL Endcap Region*, D. Hochman, et al., OPAL TN233, 1994.

[20] *Report from the Bunch Train Working Group*, T. Camporesi et al., CERN/LEPC 94-13.

[21] *Bunch Trains for LEP2*, E. Keil, Proceedings, Fifth Workshop on LEP Performance, Chamonix, 1995.

[22] *Correction to EE Calibration Coefficients for Bunch Trains*, C.P. Ward, OPAL TN302, 1995.

[23] *Bicron Corp.*, 12345 Kinsman Rd. Newbury OH 44065 USA

[24] *Kuraray Corp.*, 3-10, Nihonbashi, 2 Chome, Chuo-ku, Tokyo 103 Japan

[25] *Hoechst Aktiengesellschaft* 65926 Frankfurt am Main, Germany

[26] *E.I. duPont di Nemours*, Wilminton DE 19898 USA

[27] *Electron Tubes Ltd.*, Bury St., Ruislip, Middx HA4 7TA UK

[28] *Tests of the Hamamatsu R4760 and Thorn-EMI 9902KA Photomultiplier Tubes*, W. Springer, Internal Note, 1995.

[29] *Bicron Specifications for Scintillators and Fibres*, Bicron Catalogue, 1994.

[30] *Techniques for Nuclear and Particle Physics Experiments*, W.R. Leo, Springer-Verlag, 1992.

[31] *Review of Particle Physics*, Physical Review D54 (1996).

[32] *Theory and Practice of Scintillation Counting*, J.B. Birks, Pergamon Press, 1964.

[33] T. Foerster, Ann. Phys. 2, (1948) 55.

[34] *Energy-Transfer and Light-Collection Characteristics for Different Types of Plastic Scintillators*, B. Bengston and M. Moszynski, NIM 117 (1974) 227.

[35] *Introduction to Experimental Particle Physics*, R.C. Fernow, Cambridge University Press (1986), p.155.

[36] *Leaky-Ray Theory of Optical Waveguides of Circular Cross Section*, A.W. Snyder, Appl. Phys. 4, 273-298 (1974).

[37] *Principles of Optics*, M. Born and E. Wolf, Pergamon Press, Oxford, 1975.

[38] *Optical Waveguide Theory*, A. Snyder and J. Love Chapman and Hall, 1983.

[39] *Scintillating Fibres*, T.O. White, NIM A273 (1988) 820-825.

[40] *Monte Carlo Simulations of Scintillating Fiber Optic Waveguides*, R.J. Mountain, p.278, Proceedings, Symposium on Detector Research and Development for The SSC, 1990.

[41] *GUIDEIT V1.1 Users Manual*, Daniel A. Simon, October 1993.

[42] *PVM 3 User's Guide and Reference Manual*, A. Geist et al., ORNL/TM-12187, September 1994.

[43] *Trapping Efficiency of Plastic Luminescent Fibers*, P. Rebourgeard, H. Blumenfeld, and M. Bourdinaud, DAPNIA/SED 96-02, October 1996.

[44] *Lite-On Inc.*, 720 South Hillview Drive, Milpitas, CA 95035.

[45] *Connectix Corporation*, 2955 Campus Drive, San Mateo, CA 94403.

[46] *Private Communication*,D. Johnson and N. Rodning.

[47] *Scintillator-Fiber Charged-Particle Track-Imaging Detector*, W. Binns, M. Israel, and J. Klarmann, NIM 216 (1983) 475-480.

[48] M.P. De Pascale et al., J. Geophys. Res. 98 3501 (1993).

[49] *Cosmic Rays on Earth*, K. Allkofer and P.K.F. Grieder, Fachinformationszentrum, Karlsruhe (1984).

[50] PHILIPS Data Handbook, Electron Tubes, September 1992.

[51] E.I. duPont di Nemours, Wilminton DE 19898 USA

[52] *Numerical Recipes in Fortran*, W.H. Press, S.A. Teukolsky, W.T. Vetterling, B.P. Flannery, Cambridge University Press, 1992.

[53] *Private Communication*, N. Rodning.

[54] *Photomultipliers and Accessories*, Electron Tubes Ltd., Bury St., Ruislip, Middx HA4 7TA UK

[55] *The OPAL Primer*, 1997.

[56] *CERNLIB - CERN Program Library Short Writeups*, (1993).

Appendix A

Simulation of Photon Propagation Through Bent Optical Fibres

Version 1.1 of the GUIDEIT [41] ray-tracing routines permitted the description of straight cylinders or fibres only. Therefore in order to implement GUIDEIT as a replacement of the GEANT Version 3.21 [17] photon tracking through wavelength shifting (WLS) fibres it was necessary to extend the GUIDEIT program to create routines which would handle photon propagation through bent fibres. By enabling tracking through bent fibres it would then be possible to accurately simulate photon tracking through a wide variety of fibre layouts, including those of the three sigma fibre tile and the TE Tile 2, discussed in Chapters 7 and 8, respectively.

An overview of the additions to GUIDEIT are described below, followed by a brief examination of the application of GUIDEIT to simulations of the losses of photons through bent fibres.

A.1 Photon Tracking Through Toroidal Geometries

The GUIDEIT software was adapted in order to overcome the geometric limitations of GEANT and provide an accurate description of bent fibres. Routines to

define the toroidal geometry as specified by the user and to perform the necessary photon tracking were added to the GUIDEIT library.

In the detector description provided to GUIDEIT the user can specify a toroid shape by the coordinates of the torus center, the swept radius of the torus, and the tube radius. The user also specifies the angular range through which the toroid sweeps.

The method of tracking used in GUIDEIT determines the intersection of a ray with a given surface. The ray describing a photon trajectory is defined by the parametric ray equations given by

$$\begin{aligned} X &= X_0 + T \cdot X_1 \\ Y &= Y_0 + T \cdot Y_1 \\ Z &= Z_0 + T \cdot Z_1 \end{aligned} \tag{A.1}$$

where (X_0, Y_0, Z_0) is the origin of the ray, (X_1, Y_1, Z_1) the components of the ray direction vector. If the ray intersects the toroidal geometry at the position (X, Y, Z) then the distance from the the ray origin to the intersection point is given by the value of T. It is the value of T which defines the step size taken in the propagation of the photon ray through the geometry.

To determine the intersection of a given ray with a toroidal surface consider the original equations for a toroid centered at the position $(X, Y, Z) = (0, 0, 0)$ and defined by an axis $(0, 0, 1)$. The equation for two circles of radius B centered at positions $(-A, 0, 0)$ and $(A, 0, 0)$ is given by

$$((R - A)^2 + Z^2 - B^2) \cdot ((R + A)^2 + Z^2 - B^2) = 0 \tag{A.2}$$

where A is the swept radius and B is the tube radius of the toroid. In order to

rotate the two circles about the Z-axis the substitution $R^2 = X^2 + Y^2$ is made. Substitution of the parametric ray equations yields a quartic polynomial in the variable T and is written as

$$C_4 \cdot T^4 + C_3 \cdot T^3 + C_2 \cdot T^2 + C_1 \cdot T + C_0 = 0 \tag{A.3}$$

The coefficients of the polynomial are

$$C_4 = (X_1^2 + Y_1^2 + Z_1^2)^2 \tag{A.4}$$

$$C_3 = 4.0 \cdot (TX + TY + TZ) \cdot (X_1^2 + Y_1^2 + Z_1^2) \tag{A.5}$$

$$\begin{aligned} C_2 = 2.0 \cdot (X_1^2 + Y_1^2 + Z_1^2) \cdot (X_0^2 + Y_0^2 + Z_0^2 - A^2 - B^2) \\ +4.0 \cdot (TX + TY + TZ)^2 \\ +4.0 \cdot A^2 \cdot Z_1^2 \end{aligned} \tag{A.6}$$

$$C_1 = 4.0 \cdot (TX + TY + TZ) \cdot (X_0^2 + Y_0^2 + Z_0^2 - A^2 - B^2) + 8.0 \cdot A^2 \cdot TZ \tag{A.7}$$

$$C_0 = (X_0^2 + Y_0^2 + Z_0^2 - A^2 - B^2)^2 + 4.0 \cdot A^2 \cdot (Z_0^2 - B^2) \tag{A.8}$$

where TX, TY, TZ are equal to $X_0 \cdot X_1, Y_0 \cdot Y_1, Z_0 \cdot Z_1$, respectively.

In order to compute the roots of this quartic polynomial the CERNLIB [56] routine DRTEQ4 is called. The value of the step size T is then equal to the value of the smallest positive real root returned.

If the ray is considered to have intersected the toroid the value of the hit position is checked to ensure it is within the angular region of the toroid specified as a component of the detector geometry. If the photon-toroid intersection point is indeed within the detector description then the normal to the toroid surface at the intersection point (X, Y, Z) is computed. The photon at this point either

undergoes total internal reflection or refraction, depending upon the relative values of the refractive indices of the optical fibre core and cladding layers.

Further changes were necessary to the GUIDEIT tracking procedure in order to simulate multiclad fibres such as those used for the TE Tiles as discussed in Chapter 3.

A.2 Losses of Photons in Bent Fibres

A simple simulation using the new toroid tracking GUIDEIT program was constructed to determine the transmission and losses of photons in bent optical fibres. The optical fibre to be simulated was bend at a radius of 2.5 cm and extended over an angular range of 90°. Two straight fibre sections each 5.0 cm in length are placed before and after the bend to ensure that the incoming photons were already trapped by total internal reflection.

Two possible fibre types were studied. The single clad fibre consisted of a central core material surrounded by a single layer of material. The refractive indices of the core and cladding layers were $N_{core} = 1.60$ and $N_{clad} = 1.49$ extending to radii of 0.0485 cm and 0.050 cm, respectively. The double clad fibre was identical to the single clad but also included a second cladding layer of refractive index $N_{clad2} = 1.42$. For this fibre the first cladding layer only extended to 0.049 cm.

To simulate the transmission of photons through the fibre bends 1000000 photons were generated and tracked using GUIDEIT from one end of a straight fibre and then through the 90° bend with approximately 90 % and 93 % transmission achieved for the single and double clad fibres, respectively. As expected from geometrical optics the second cladding layer acts to trap a greater portion

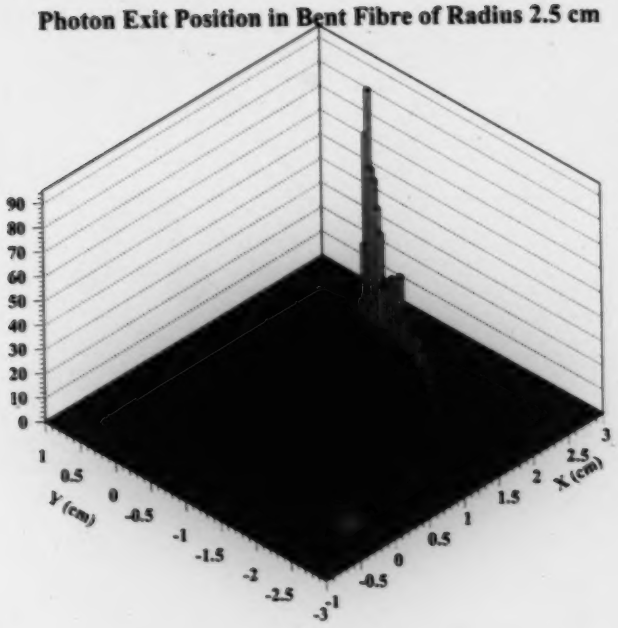

Figure A.1: Exit position of a photon which escapes from a bent optical fibre of radius 2.5 cm. The photons enters the fibre bend at $(X, Y) = (2.5, 0.0)$ and are propagating along the negative y direction.

of the propagating photons.

Figure A.1 shows for the double clad fibre the the (x, y) position along the fibre bend where the photons fail to undergo total internal reflection at either of the cladding layers. The vast majority of the photons which escape the fibre do so at or very near the beginning of the arc.

Appendix B

Optical Fibre Connector Simulation Results

The examination of the light yield uniformity for the three sigma Monte Carlo analysis determined the mean number of photoelectrons which would be observed if the photomultiplier were coupled directly to the end of the wavelength shifting fibre. Since the experimental setup for the three sigma tile coupled the wavelength shifting fibre to a 2.5 m long clear optical fibre, a connector must then be included in the simulation when considering the average light yield.

B.1 Optical Fibre Connector Simulations

During development with the prototype three sigma fibre tile the wavelength shifting fibre was coupled to a clear optical fibre using a fused joint connector. With the fused joint connector there is a small layer of optical grease between the two fibre sections. Several uncertainties exist concerning the connector, including the thickness of the optical grease layer, the degree to which the fibre axes are aligned, and the surface polish quality of the two fibre faces. To determine the transmission characteristics of various connector designs a stand-alone simulation using the GUIDEIT ray-tracing software was constructed. Figure B.1 schematically shows the layout of the simulated connector geometry.

In the simulation a WLS fibre of radius R_{WLS} and core refractive index of

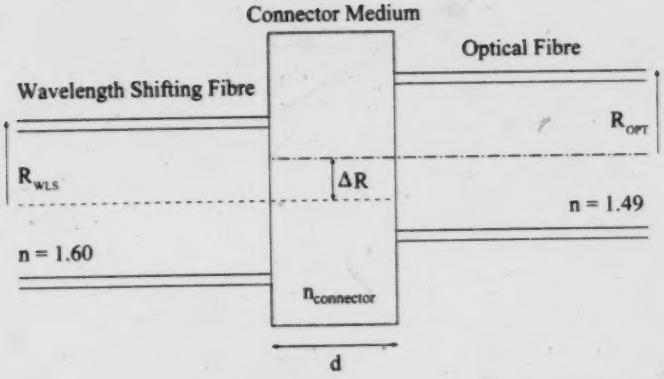

Figure B.1: Layout of the WLS fibre to optical fibre connector simulated using GUIDEIT. The WLS fibre of radius R_{WLS} and refractive index $n = 1.60$ is coupled through a connector medium of thickness d and refractive index $n_{connector}$ to an optical fibre of radius R_{OPT} and refractive index $n = 1.49$. The fibre axes may be misaligned by an amount ΔR.

$n_{WLS} = 1.60$ is coupled through a connector medium of thickness d and refractive index $n_{Connector}$ to an optical fibre of radius R_{OPT} and refractive index $n_{Optical} = 1.49$. The fibre axes may be misaligned by an amount ΔR. The connector medium was simulated for the two possible cases of being either a typical optical grease ($n_{Connector} = 1.60$) or an air gap ($n_{Connector} = 1.00$). Both fibres were assumed to have perfectly smooth polished fibre ends. A photon incident upon the end of the wavelength shifting fibre will enter the connector medium only if the angle of incidence is less than the critical angle $\theta_{C1} = \sin^{-1} n_{Connector}/n_{WLS}$ defined by the relative refractive indices of the WLS fibre core and connector medium. If transmitted into the connector the photon will only pass into the optical fibre if it is incident upon the fibre face and if the angle of incidence is again less than the critical angle $\theta_{C2} = \sin^{-1} n_{Optical}/n_{Connector}$ at the interface. The performance of the connector can be characterized by the transmission factor $T_{Connector}$ defined as

the fraction of photons exiting the WLS fibre which survive the transition through the connecting medium and successfully enter the optical fibre.

Table B.1 lists the values of the transmission factor $T_{Connector}$ for an optical grease connection with values of gap size d and misalignment ΔR with ranges of 0.001 to 0.100 cm and 0.000 to 0.010 cm respectively. Table B.2 lists the transmission factor $T_{Connector}$ for the same geometric ranges but for an air gap connector. For both cases the radius of the WLS fibre R_{WLS} and the clear optical fibre R_{OPT} were assumed to be 0.0485 cm, equivalent to the radius of the BCF-91A and clear optical fibre of the TE detector.

For the optical grease connector the transmission factor $T_{Connector}$ remains in excess of 90% for connector gap sizes up to 0.010 cm and misalignments up to 0.005 cm.

B.1.1 Radial Distribution of Photons

The observed increased degradation as a function of connector gap size is a result of of the high density of photons at the WLS fibre outer radius. Such photons have values of polar angle approaching 90° and as such upon entering a new medium, even of the same refractive index, will have trajectories directed away from the fibre axis. If the size of the connector gap is large enough then the photon after propagating through the gap distance d in the direction of the fibre axis will be at a radial extent beyond that of the adjoining optical fibre. The photons therefore do not reach the connector medium-optical fibre boundary and are lost.

Figure B.2 demonstrates the distribution of the photons in the fibre cross-section as a function of radius upon exiting the wavelength shifting fibre for an

Connector Gap Size d (cm)	Misalignment ΔR (cm)	Transmission Factor $T_{Connector}$
0.001	0.000	0.999
0.005	0.000	0.992
0.010	0.000	0.962
0.025	0.000	0.861
0.050	0.000	0.721
0.100	0.000	0.517
0.001	0.001	0.998
0.005	0.001	0.990
0.010	0.001	0.962
0.025	0.001	0.861
0.050	0.001	0.721
0.100	0.001	0.517
0.001	0.005	0.942
0.005	0.005	0.930
0.010	0.005	0.910
0.025	0.005	0.830
0.050	0.005	0.701
0.100	0.005	0.502
0.001	0.010	0.850
0.005	0.010	0.840
0.010	0.010	0.825
0.025	0.010	0.770
0.050	0.010	0.661
0.100	0.010	0.475

Table B.1: Transmission coefficient results for varying connector size and fibre misalignment from Monte Carlo simulation of an optical grease connector with refractive index $n_{Connector} = 1.60$.

Connector Gap Size d (cm)	Misalignment ΔR(cm)	Transmission Factor $T_{Connector}$
0.001	0.000	0.866
0.005	0.000	0.844
0.010	0.000	0.800
0.025	0.000	0.677
0.050	0.000	0.515
0.100	0.000	0.296
0.001	0.001	0.865
0.005	0.001	0.841
0.010	0.001	0.799
0.025	0.001	0.676
0.050	0.001	0.516
0.100	0.001	0.296
0.001	0.005	0.824
0.005	0.005	0.804
0.010	0.005	0.769
0.025	0.005	0.658
0.050	0.005	0.502
0.100	0.005	0.289
0.001	0.010	0.754
0.005	0.010	0.736
0.010	0.010	0.710
0.025	0.010	0.618
0.050	0.010	0.476
0.100	0.010	0.271

Table B.2: Transmission coefficient results for varying connector size and fibre misalignment from Monte Carlo simulation for an air gap connector of refractive index $n_{Connector} = 1.00$.

optical grease connector of 0.050 cm thickness and zero misalignment. The radial distributions are shown for the cases of both the stand-alone GUIDEIT connector simulation (dashed line) and the three sigma fibre tile simulation which used both GEANT and GUIDEIT (solid line). The stand-alone GUIDEIT simulation generates the WLS photons directly so as to be uniformly distributed in the fibre cross-section, and subsequently tracks the photons down the fibre. Both distributions are generally in good agreement and clearly indicate that greater than 50 percent of the photons are propagating in the outer 20 % of the fibre radius. The radial distribution of photons at then end of the WLS fibre , also shown in Figure B.2, which survive the propagation through the connector and enter the optical fibre are also in good agreement. The good agreement between the stand-alone and full three sigma fibre simulations shows the validity of being able to look at the issues surrounding the connector performance independently of the three sigma performance.

The effect of the connection medium of thickness d on the amount of light propagated through the connector is shown in Figure B.3 for both the full three sigma fibre simulation as well as the stand-alone GUIDEIT simulation. Again the connector medium is optical grease 0.050 cm in thickness will no misalignment between the fibre axes. The solid line represents the radial distribution of photons at the exit of the WLS fibre while the dashed line is the exit radius of the photon in the WLS fibre for those which survive through the connector and enter the optical fibre. The presence of the connector degrades the number of photons by a factor of $T_{Connector} = 0.721$, the majority of which are in the outer 30% of the fibre radius. The amount of loss decreases with smaller separations of the two fibres since fewer photons will have propagated to a radius larger than the optical fibre.

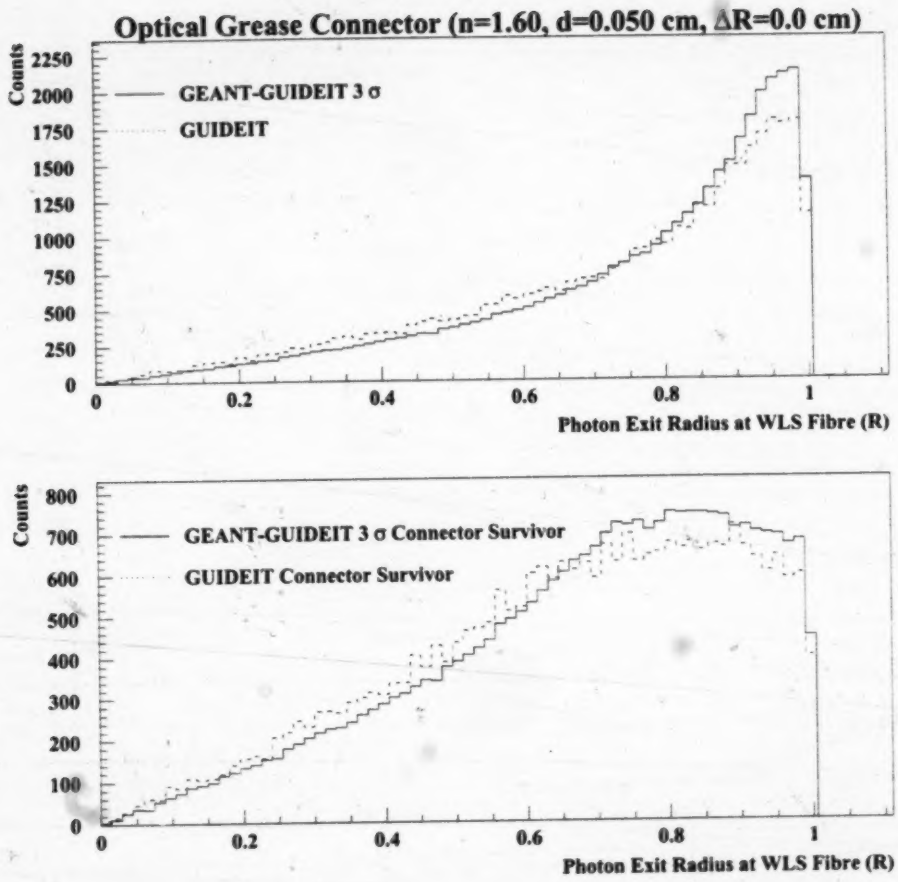
Optical Grease Connector (n=1.60, d=0.050 cm, ΔR=0.0 cm)
Counts
GEANT-GUIDEIT 3 σ
GUIDEIT
Photon Exit Radius at WLS Fibre (R)
GEANT-GUIDEIT 3 σ Connector Survivor
GUIDEIT Connector Survivor
Photon Exit Radius at WLS Fibre (R)

Figure B.2: Comparison of the GEANT-GUIDEIT 3σ and GUIDEIT stand-alone predictions for the radial distribution of photons in the fibre cross-section which reach the end of the WLS fibre (solid line) and survive the adjoining connector (dashed line) for an optical grease connector of 0.050 cm thickness and zero misalignment.

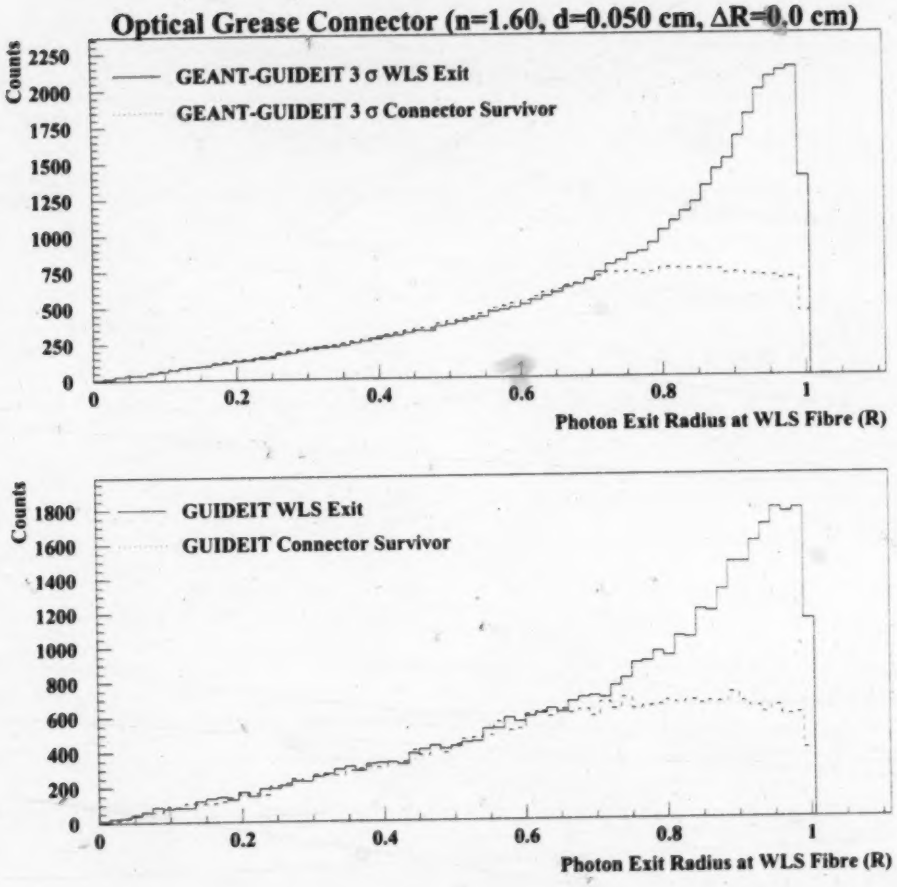
Optical Grease Connector (n=1.60, d=0.050 cm, ΔR=0.0 cm)
Counts
GEANT-GUIDEIT 3 σ WLS Exit
GEANT-GUIDEIT 3 σ Connector Survivor
Photon Exit Radius at WLS Fibre (R)
GUIDEIT WLS Exit
GUIDEIT Connector Survivor
Photon Exit Radius at WLS Fibre (R)

Figure B.3: Comparison of the radial distribution of photons in the fibre cross-section which reach the end of the WLS fibre (solid line) and survive the adjoining connector (dashed line) for both GEANT-GUIDEIT 3 σ and GUIDEIT stand-alone simulations of an optical grease connector of 0.050 cm thickness and zero misalignment.

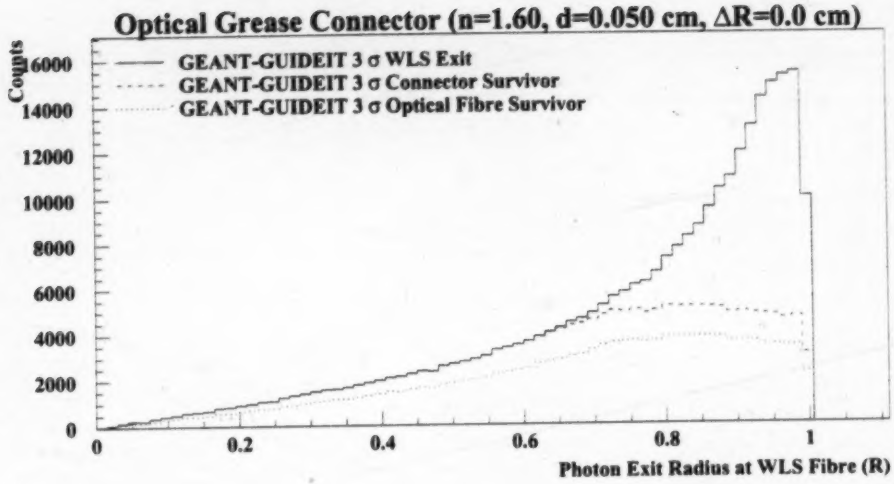

Figure B.4: Radial distribution of photon exit positions at the WLS fibre for photons which exit the WLS fibre (solid line), propagate through the connector (dashed line) and survive to the end of the optical fibre (dotted line) for an optical grease connector medium of 0.050 cm thickness and zero misalignment.

In addition to experiencing transmission losses due to the connector, photon attenuation within the optical fibre acts to degrade the number of photons which reach the end of the optical fibre. Figure B.4 shows the radial distribution of photons at the WLS fibre exit for photons which enter the connector medium, photons which survive the connector medium and pass into the optical fibre, and which survive to the end of a 2.5 m optical fibre length. The attenuation of the optical fibre was approximately 35.0 m. From the distribution it is evident that the largest amount of loss occurs at the connector interface. The losses due to attenuation also act greatest upon the photons which are at the outer perimeter of the fibre since photons which propagate towards the outer radius of the fibre

must travel longer distances in order to traverse the same length of optical fibre compared to photons with trajectories of polar angle $\ll 90°$.

Therefore it has been demonstrated that an optical fibre connector can be simulated independently and yield results equal to those corresponding to the full three sigma fibre simulation.

As discussed previously in Chapter 6 the light distribution within a single WLS fibre has been successfully simulated and compared with measurements performed using a CCD array. This successful simulation has been applied to demonstrate that a WLS to optical fibre connector can be simulated independently and yield results equal to those achieved via the full three sigma fibre Monte Carlo. Therefore many different connector designs can be simulated accurately and applied efficiently without having to specify the connector geometry explicitly in the analysis of the Monte Carlo output. Since the connector simulation performed in the three sigma analysis is carried out simultaneously with the parameterization of the reflectivity values for any of the reflectivity combinations listed in Table 7.4, a great deal of time is saved by performing the separate connector simulation. A fast estimate of the number of photoelectrons at the end of the wavelength shifting fibre is therefore possible, and those connectors which indicate a good agreement with the measured result can then be fully simulated with the three sigma fibre tile analysis.